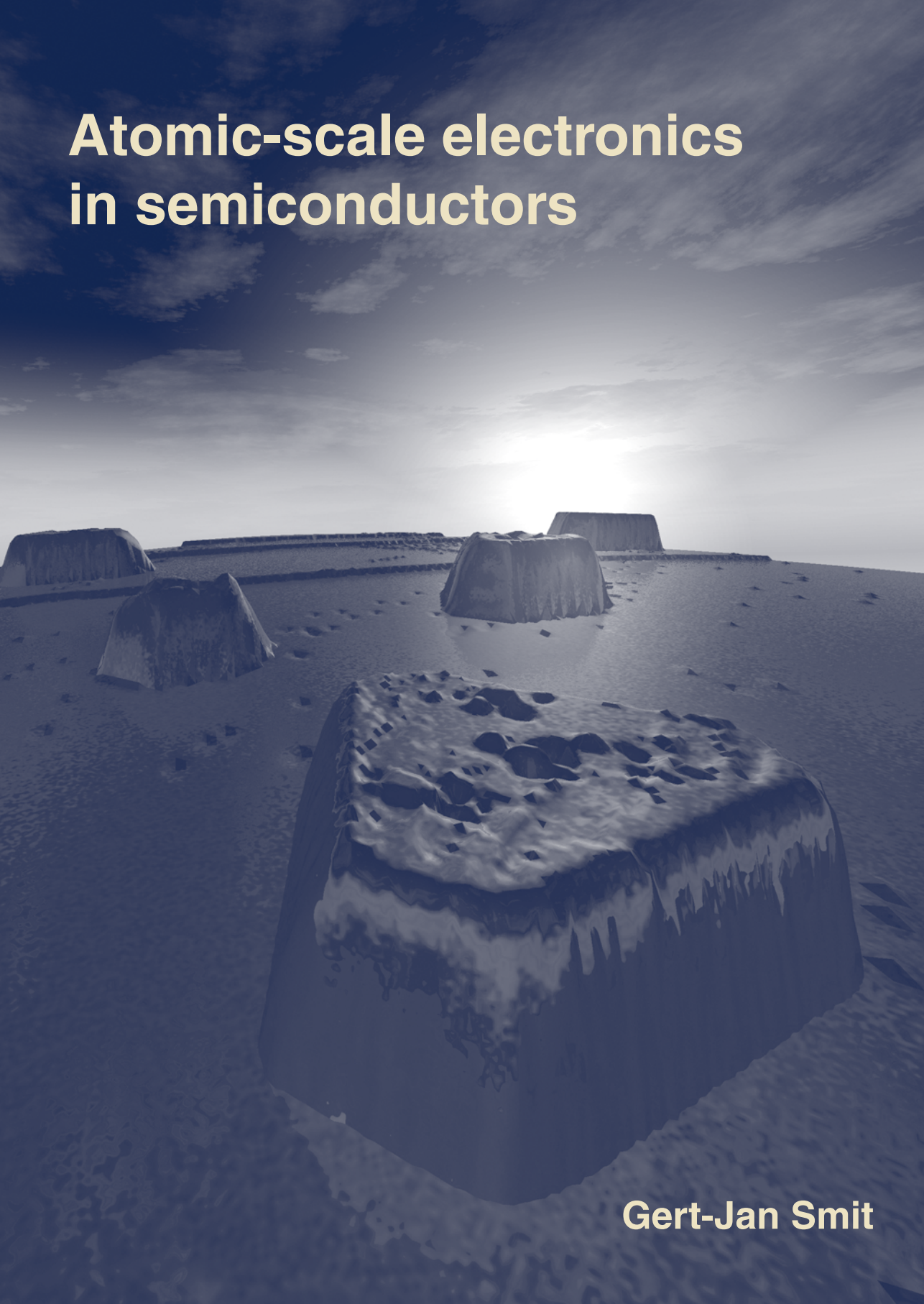


Atomic-scale electronics in semiconductors



Gert-Jan Smit

Atomic-scale electronics in semiconductors

Atomic-scale electronics in semiconductors

Proefschrift

ter verkrijging van de graad van doctor
aan de Technische Universiteit Delft,
op gezag van de Rector Magnificus prof. dr. ir. J. T. Fokkema,
voorzitter van het College voor Promoties,
in het openbaar te verdedigen op maandag 16 februari 2004 om 15.30 uur

door

Geert Derk Jan SMIT

doctorandus in de natuurkunde en wiskunde,
geboren te Meppel.

Dit proefschrift is goedgekeurd door de promotor:

Prof. dr. ir. T. M. Klapwijk

Samenstelling promotiecommissie:

Rector Magnificus, voorzitter

Prof. dr. ir. T. M. Klapwijk, Technische Universiteit Delft, promotor

Prof. dr. ir. G.E.W. Bauer, Technische Universiteit Delft

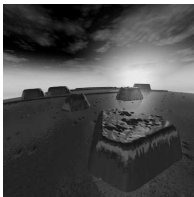
Prof. dr. J.T.M. de Boeck, IMEC en Technische Universiteit Delft

Prof. dr. H.W.M. Salemink, Technische Universiteit Eindhoven

Prof. dr. J.R. Tucker, University of Illinois at Urbana-Champaign

Dr. S. Rogge, Technische Universiteit Delft

Dr. R. Woltjer, Philips Research



Cover image: Three-dimensional representation of a scanning tunneling micrograph, showing several CoSi_2 -islands on a $\text{Si}(111)$ surface. The scale in the z -direction is greatly exaggerated.

The research described in this thesis was done as part of the DIOC (Delft interfacultair onderzoekscentrum) program ‘Novel computation structures based on quantum devices’.

The ‘Stichting voor Fundamenteel Onderzoek der Materie (FOM)’ which is financially supported by the ‘Nederlandse Organisatie voor Wetenschappelijk Onderzoek (NWO)’ is acknowledged for providing the experimental infrastructure.

Printed by OPTIMA Grafische Communicatie, Rotterdam, The Netherlands

ISBN 90-77595-06-6

Keywords: Nano-electronic devices / semiconductors at the atomic scale / discreteness of doping / single dopant spectroscopy / crystal fields / Stark effect / Zeeman effect

Copyright © 2004 by G. D. J. Smit

All rights reserved. No part of the material protected by this copyright notice may be reproduced or utilized in any form or by any means, electronic or mechanical, including photocopying, recording or by any information storage and retrieval system, without permission from the author.

Contents

.....

1	Atomic scale electronics	1
	1.1 Introduction	1
	1.2 Overview of current research	2
	1.2.1 Ultimate silicon technology	
	1.2.2 Wave function manipulation and detection	
	1.3 Outline of this thesis	5
2	Scaling of Schottky diodes	9
	2.1 Introduction	9
	2.2 Theory	11
	2.2.1 Barrier shape	
	2.2.2 Transport	
	2.3 Experiments	17
	2.3.1 Sample preparation and characterization	
	2.3.2 Measurements	
	2.4 Results and discussion	21
	2.5 Conclusion	24
3	Scaling of micro-fabricated nanometer-sized Schottky diodes	27
	3.1 Introduction	27
	3.2 Simulations and results	28
	3.3 Discussion	29
	3.4 Conclusion	31
4	Conductance distribution in nanometer-sized semiconductor devices due to doping statistics	33
	4.1 Introduction	33
	4.2 Measurements	34
	4.2.1 Room temperature measurements	
	4.2.2 Low temperature measurements	

4.3	Analysis	39
4.4	Application to the data	41
4.5	Conclusions	42
5	Spectroscopy of individual dopant atoms	45
5.1	Introduction	45
5.2	Experiments in large devices	46
5.3	Experiments in nano-devices	49
5.4	Discussion	52
5.5	Conclusion	53
6	Group theoretical analysis of double acceptors in a magnetic field: identification of the Si:B⁺ ground state	55
6.1	Introduction	55
6.2	Background	56
6.3	Double acceptors in a magnetic field	57
6.4	Linear Zeeman effect	59
6.4.1	The Γ_7 -levels	
6.4.2	The $\Gamma_3 + \Gamma_5$ level	
6.5	Quadratic Zeeman effect	60
6.5.1	The Γ_1 and Γ_2 levels	
6.5.2	The Γ_3 level	
6.5.3	The Γ_4 and Γ_5 levels	
6.6	Central field approximation	62
6.7	Application to B ⁺	63
6.8	Conclusions	65
7	Stark effect of shallow impurities in Si	67
7.1	Introduction	67
7.2	Donors	69
7.2.1	The donor ground state	
7.2.2	Symmetry of the donor ground state in an electric field	
7.2.3	Shift and splitting in an electric field	
7.3	Acceptors	76
7.3.1	Linear Stark effect	
7.3.2	Quadratic Stark effect	
7.4	Large electric fields in the SHM	79
7.5	Discussion and conclusion	82

8	Gate-induced ionization of single dopant atoms	85
8.1	Introduction	85
8.2	Model system	86
8.3	Solving the Schrödinger equation	87
8.4	Results	89
8.5	Discussion	91
8.6	Application	92
8.7	Conclusion	92
A	Representations of groups	95
A.1	Introduction	95
A.2	Groups	95
	A.2.1 Crystallographic point groups	
	A.2.2 Double groups	
A.3	Representations	97
	A.3.1 Reducibility	
	A.3.2 Product representation	
A.4	Characters	98
A.5	Relevant character tables	99
A.6	Representations and wave functions	99
A.7	Matrix elements	102
	Summary	105
	Atomic-scale electronics in semiconductors	105
	Elektronica op atomaire schaal in halfgeleiders	106
	List of publications	109
	Dankwoord	111
	Curriculum Vitae	113



Atomic scale electronics

.....

1.1 Introduction

The size of a hydrogen atom is defined by its Bohr radius, which is only half an Angstrom. A dopant atom in a semiconductor—considered as the solid state analogue of a hydrogen atom—has a Bohr radius of several nanometers. Nowadays semiconductor technology has arrived at the edge of the regime where this length scale is accessible, thus enabling experimental study and control of a single atom’s wave functions. This capability opens up new lines of research in several areas of physics. The emerging field, concerned with electronic processes and devices in which individual dopant atoms play a role, is called *Atomic Scale Electronics* (ASE).

It is well-known that the introduction of dopant impurities in a semiconductor has an enormous effect on its electrical properties. The conductivity of a semiconductor can be tuned over many orders of magnitude by varying the concentration of dopant atoms, while the *type* of charge carriers (electrons or holes) can be chosen by selecting the right type of impurity. Next to chemical doping, the carrier density in a semiconductor can be changed dynamically by using electrostatic gates. The versatility of semiconductor material, combined with the application of oxides and metals (‘permanent’ insulators and conductors), has led to the tremendous success of CMOS-technology (complementary metal oxide semiconductor) in computer industry.

Traditionally, the effect of doping is considered as a homogeneous effect, changing the intensive properties of the material. Indeed, in most practical applications the concentration of mobile charge carriers, the Fermi-level position, and the conductivity can be considered as constant throughout the semiconductor bulk. In reality, however, the dopant atoms are discrete entities, the positions of which are randomly distributed in the host material. The total number of dopant atoms in a device determines whether the discreteness can be ignored or must be taken into account (see Fig. 1.1).

The exponentially increasing demand for cheaper, faster, more compact, more functional, and more power-saving electronics is mainly being met by the industry through

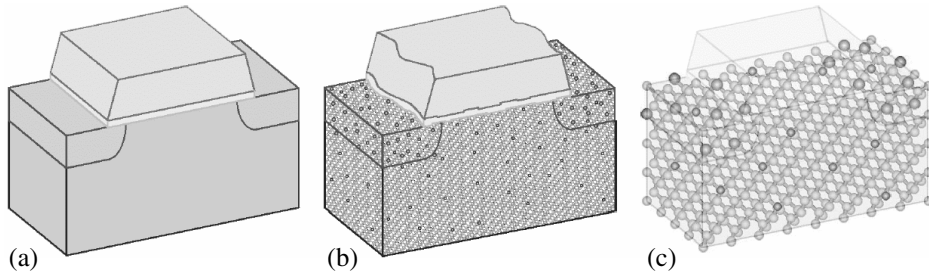


Figure 1.1 Schematic drawing of a MOSFET, illustrating the transition from a continuous to an atomistic regime. **(a)** In the conventional picture the material properties are homogeneous and the boundaries smooth and abrupt. **(b,c)** In smaller devices [channel length 20 nm (b) and 4 nm (c)] the discrete and random nature of doping causes large intrinsic parameter fluctuations. (Image courtesy of A. Asenov)

a higher level of integration. Manufacturing more components per chip requires smaller devices. Ever since the steady trend in the size reduction of the components has been recognized (Moore's law), people have realized that this trend cannot continue infinitely. The discreteness of doping has, in fact, been recognized as one of the fundamental limits in scaling down the existing technology: if the number of dopants in a device gets small, relative statistical variations get large and the device behavior becomes a sensitive function of the the actual number of dopants and their positions, leading to unreliable device behavior. In the top-down approach employed by the semiconductor industry, the discreteness of doping is therefore considered as a big problem, eventually resulting in hitting a 'brick wall'.

However, the fact that the 'atomic' length scale is already within reach in a laboratory environment offers great opportunities. New research can be anticipated, comprising control and detection of charge and spin in semiconductors at the level of *individual* dopant atoms. Starting from there gives rise to a bottom-up approach that may lead to novel types of devices, circuits and computer architectures.

The important length scale at which the physics of single dopants takes place is referred to as the *atomic* scale. At sufficiently low temperatures, a dopant atom binds one or more valence electrons or holes. In a first order approximation, such an entity is very similar to a hydrogen (helium, lithium, ...) atom in vacuum. The Bohr radius of a dopant atom (defined in analogy with hydrogen) is a natural candidate for defining the dopant's 'size'. It is a measure for the extent of the wave function of the carrier(s) bound to the dopant and also for the extent of the potential well caused by the ionized dopant.

1.2 Overview of current research

Semiconductor physics at the atomic scale can be looked at and worked on from various perspectives. To demonstrate that it is indeed a vivid and emerging field, several

examples of ongoing research that can be captured under the umbrella of ASE are outlined below.

Ultimate silicon technology deals with the development techniques for growth, lithography and control of material properties, which are required for the fabrication of devices down to the atomic scale. Many physical effects cannot straightforwardly be extended below a certain length scale. An especially important issue is coping with the discreteness of doping, as sketched above. Moreover, control of materials down to the level of individual dopant atoms will become more and more essential.

Understanding macroscopic properties of (complex) materials from an atomistic point of view is supported by experiments accessing the level of single dopant atoms. An interesting example in this respect is the use of a scanning tunneling microscope to spatially map the wave function of a hole bound to a Be-acceptor [1] or a Mn-acceptor [2] in GaAs. The latter may help to better understand the magnetic properties of this material. Another example is the direct observation (by scanning transmission electron microscopy) of Sb-clusters in heavily doped Si, explaining the saturation of the mobile charge carrier concentration with increasing doping level [3].

The miniaturization in Si technology has led to new device concepts. Among the most important is the idea to use individual dopant atoms as quantum bits (qubits) for a quantum computer (QC). The first elaborated QC-design in this category is due to Kane [4, 5] and was later followed by several variants [6, 7, 8, 9]. Experimental achievements in solid state quantum computing are hardly at the proof-of-principle stage in terms of their abilities to perform quantum computational tasks. Nevertheless, many groups are performing calculations and experiments which are motivated by a certain aspect of one of these QC-designs, thus extending their research to the field of individual dopant atoms.

The physical phenomena playing a role in ASE are related to many areas in physics. In many respects, ASE is a sophisticated extension of semiconductor physics. The similarity of a dopant atom with a hydrogen (helium, lithium, ...) atom leads to a natural link with atomic physics. The well-developed field of (coupled) quantum dots is closely related to physics of the quantum coherent interactions of the nuclear and electron spins in a dopant atom.

Because ASE covers several different areas of (semiconductor) physics, recognition of a common element can stimulate fruitful cross-fertilization between them. Therefore, ASE is a useful umbrella that emphasizes a valuable relationship between various research fields.

This thesis will obviously be concerned with only a subset of the topics outlined above. In the following subsections, a more detailed overview will be given of recent progress and results in those subfields of ASE, that are related to this thesis.

1.2.1 Ultimate silicon technology

From a top-down approach, random spatial fluctuations in the potential landscape of a device due to randomly positioned dopants have since long been recognized as a serious problem in scaling down MOSFETs [10, 11, 12]. They cause large and unpredictable device-to-device threshold voltage [13] and resistance [14] variations, which can

inherently not be prevented by optimizing the fabrication process. In this context, various groups are trying to model these effects and understand them theoretically [15, 16]. Moreover, new device concepts are being developed in order to extend this limit of device scaling, such as the Schottky barrier MOSFET [17], thin-channel MOSFET [18], and the FinFET [19].

Even when the discreteness of doping does not need to be taken into account, devices start to behave differently when their feature size drops below the semiconductor screening length (Debye length, L_D , which is a measure for the spatial extent of space charge regions). This effect has been observed in many different material systems (see for instance Ref. 20, 21, 22).

Of more fundamental interest is the development of silicon nanowires. These structures make it possible to realize not only nanometer-sized metal-semiconductor contacts, but also small *pn*-junctions and transistors [23]. Due to their unconventional geometry, the electrostatic picture is quite different from conventional devices. Moreover, nanowires provide the opportunity for experimental studies of one-dimensional transport in semiconductors. A very intriguing related issue is the effect of doping on the conductivity and mobility in such one-dimensional structures, even more as the nanowire diameter can be as small as 1 nm [24], which is smaller than the Bohr-radius of a dopant.

1.2.2 Wave function manipulation and detection

The effect of external perturbations on the wave function of a dopant atom (in large ensembles of dopants) has been investigated for several decades and is a fairly mature field [25]. The prospect of realizing quantum computing using individual dopant atoms as qubits has renewed the interest in this field.

Motivated by the QC design of Kane [4], several groups have performed calculations on the action of a small local gate on a nearby dopant atom [26, 27, 28]. Moreover, it has been shown that the exchange interaction between two dopant atoms can also be tuned by a gate [29]. This is especially interesting because the exchange coupling shows non-monotonous behavior as a function of the inter-dopant distance in Si [30].

Despite the large theoretical effort, experimental results on the electronic state of individual dopant atoms under external perturbations are very limited in number. In most of the measurements published until now, the dopant atom was located in a device that was originally designed for other purposes [31, 32, 33]. For that reason, there was only limited control and knowledge about the nature and exact position of the impurity under investigation. More dedicated experiments to verify the theoretical predictions would be facilitated by precise positioning of one or more dopant atoms in a device. Various groups are developing techniques to realize this. Single ion implantation [34, 35] enables exact control of the number of impurities. However, the spatial resolution is still limited to several tens of nanometers. Alternatively, scanning tunneling microscope lithography in ultra high vacuum [36, 37] allows for positioning dopants with almost atom precision on a surface, though the required overgrowth with silicon still has to be demonstrated.

1.3 Outline of this thesis

This thesis aims at providing identification, analysis and understanding of several basic issues that are important for atomic scale electronics. We will focus on scaling of metal-semiconductor diodes, effects of the discreteness of doping on the electrical properties of small diodes, resonant tunneling spectroscopy of single dopant atoms and the effect of magnetic and electric fields on the electronic state of dopant atoms.

In Chapter 2, experiments on nanometer sized epitaxial Schottky diodes are presented, demonstrating the scaling behavior of Schottky diodes when entering the regime where their size gets small compared to the Debye length L_D in the semiconductor. A model is presented that predicts an increase in conduction (per unit area) for smaller diodes, qualitatively explaining the observed behavior.

Chapter 3 presents simulation to estimate the influence of this scaling effect in micro-fabricated devices with interconnects.

The visibility of the discreteness of doping in the IV -characteristics of small Schottky diodes is addressed in Chapter 4. A statistical analysis of the experimental results is presented, connecting the observed scatter in the measurements to fluctuations in the Schottky barrier height due to dopant atoms.

Resonant tunneling through a single dopant atom between two metallic contacts is a promising method to study the properties of individual dopants. In Chapter 5, we provide some context for the calculations in the remainder of this thesis, by presenting measurements of a tunneling device containing many single dopant channels in parallel. We use this device to study the magnetic field behavior of the B^+ -ground state, demonstrating the effectiveness of this technique in ASE. We also present the successful implementation of a fabrication and measurement scheme, that should lead to the observation of resonant tunneling through a single dopant atom in the near future.

Starting in Chapter 6, we turn to the theoretical study of (individual) dopant atoms in external fields. In this chapter, we qualitatively study the behavior of a double acceptor in a magnetic field. The results can be directly applied to the experimental data of the previous chapter and we draw conclusions about the nature of the ground state of the B^+ state.

An electric field is the most straightforward means to address an individual impurity. In Chapter 7, calculations are presented on the splitting and shift of the dopant energy levels and lifetimes in an electric field. Moreover, the applicability of the ‘scaled hydrogen model’ is discussed.

Finally, in Chapter 8 we present calculations of the influence of a local electric field on a single dopant atom. The results are of special importance in the context of quantum computing.

In summary, this thesis addresses several basic but essential issues in the field of *atomic scale electronics*. Taking our results as well as the progress of others in this field into account, it is reasonable to expect that within a few years time both the controlled manipulation of a single dopant atom’s wave function and tuning of the interaction between two dopant atoms will have been realized experimentally.

- [1] M. B. Johnson, O. Albrektsen, R. M. Feenstra, and H. W. M. Salemink, *Appl. Phys. Lett.* **63**, 2923 (1993).
- [2] A. M. Yakunin, A. Y. Silow, P. M. Koenraad, W. van Roy, J. de Boeck, and J. H. Wolter, *cond-mat/0308234* (2003).
- [3] P. M. Voyles, D. A. Muller, J. L. Grazul, P. H. Citrin, and H.-J. L. Grossmann, *Nature* **416**, 826 (2002).
- [4] B. E. Kane, *Nature* **393**, 133 (1998).
- [5] B. E. Kane, *Fortschr. Phys.* **48**, 1023 (2000).
- [6] A. M. Stoneham, A. J. Fisher, and P. T. Greenland, *J. Phys.: Condens. Matter* **15**, L447 (2003).
- [7] A. J. Skinner, M. E. Davenport, and B. E. Kane, *Phys. Rev. Lett.* **90**, 087901 (2003).
- [8] R. Vrijen, E. Yablonovitch, K. Wang, H. W. Jiang, A. Baladin, V. Roychowdhury, T. Mor, and D. DiVincenzo, *Phys. Rev. A* **62**, 012306 (2000).
- [9] D. Mozyrsky, V. Privman, and M. L. Glasser, *Phys. Rev. Lett.* **86**, 5112 (2001).
- [10] B. Hoeneisen and C. A. Mead, *Solid-State Electron.* **15**, 819 (1972).
- [11] J. D. Meindl, Q. Chen, and J. A. Davis, *Science* **293**, 2044 (2001).
- [12] Semiconductor Industry Association, *Tech. Rep.* (2001), <http://public.itrs.net>.
- [13] T. Tanaka, T. Usuki, T. Futatsugi, Y. Momiyama, and T. Sugii, *IEDM Tech. Dig.* pp. 271–274 (2000).
- [14] T. Shinada, A. Ishikawa, C. Hinoshita, M. Koh, and I. Ohdomari, *Jpn. J. Appl. Phys.* **39**, L265 (2000).
- [15] N. Sano and M. Tomizawa, *Appl. Phys. Lett.* **79**, 2267 (2001).
- [16] G. Slavcheva, J. H. Davies, A. R. Brown, and A. Asenov, *J. Appl. Phys.* **91**, 4326 (2002).
- [17] L. E. Calvet, H. Luebben, M. A. Reed, C. Wang, J. P. Snyder, and J. R. Tucker, *J. Appl. Phys.* **91**, 757 (2002).
- [18] J. Knoch and J. Appenzeller, *Appl. Phys. Lett.* **81**, 3082 (2002).
- [19] L. Chang, Y. K. Choi, J. Kedzierski, N. Lindert, P. Xuan, J. Bokor, C. Hu, and T. J. King, *IEEE Circuits & Devices Magazine* **19**, 35 (2003).
- [20] P. Avouris, I.-W. Lyo, and Y. Hasegawa, *J. Vac. Sci. Technol. A* **11**, 1725 (1993).
- [21] G. D. J. Smit, S. Rogge, and T. M. Klapwijk, *Appl. Phys. Lett.* **80**, 2568 (2002).
- [22] W. I. Park, G. C. Yi, J. W. Kim, and S. M. Park, *Appl. Phys. Lett.* **82**, 4358 (2003).
- [23] Y. Cui and C. M. Lieber, *Science* **291**, 851 (2001).
- [24] D. D. D. Ma, C. S. Lee, F. C. K. Au, S. Y. Tong, and S. T. Lee, *Science* **299**, 1874 (2003).
- [25] A. Ramdas and S. Rodriguez, *Rep. Prog. Phys.* **44**, 1297 (1981).
- [26] G. D. J. Smit, S. Rogge, J. Caro, and T. M. Klapwijk, *Phys. Rev. B* **68**, 193302 (2003).
- [27] L. M. Kettle, H.-S. Goan, S. C. Smith, C. J. Wellard, L. C. L. Hollenberg, and C. I. Pakes, *Phys. Rev. B* **68**, 075317 (2003).
- [28] A. S. Martins, R. B. Capaz, and B. Koiller (2003), *cond-mat/0308575*.
- [29] A. Fang, Y. C. Chang, and J. R. Tucker, *Phys. Rev. B* **66**, 155331 (2002).
- [30] B. Koiller, X. Hu, and S. D. Sarma, *Phys. Rev. Lett.* **88**, 027903 (2002).
- [31] M. W. Dellow, P. H. Beton, C. J. G. M. Langerak, T. J. Foster, P. C. Main, L. Eaves, M. Henini, S. P. Beaumont, and C. D. W. Wilkinson, *Phys. Rev.*

- Lett. **68**, 1754 (1992).
- [32] M. R. Desphande, J. W. Sleight, M. A. Reed, R. G. Wheeler, and R. J. Matyi, Phys. Rev. Lett. **76**, 1328 (1996).
 - [33] L. E. Calvet, R. G. Wheeler, and M. A. Reed, Appl. Phys. Lett. **80**, 1761 (2002).
 - [34] T. Schenkel, A. Persaud, S. J. Park, J. Meijer, J. R. Kingsley, J. W. McDonald, J. P. Holder, J. Bokor, and D. H. Schneider, J. Vac. Sci. Technol. B **20**, 2819 (2002).
 - [35] R. P. McKinnon, F. E. Stanley, N. E. Lumpkin, E. Gauja, L. D. Macks, M. Mitic, V. Chan, K. Peceros, T. M. Buehler, A. S. Dzurak, et al., Smart Mater. Struct. **11**, 735 (2002).
 - [36] J. R. Tucker and T.-C. Shen, Solid-State Electron. **42**, 1061 (1998).
 - [37] S. R. Schofield, N. J. Curson, M. Y. Simmons, F. J. Rueß, T. Hallam, L. Oberbeck, and R. G. Clark, Phys. Rev. Lett. **91**, 136104 (2003).



Scaling of Schottky diodes

Abstract — We have measured electrical transport across epitaxial nanometer-sized metal-semiconductor interfaces by contacting CoSi_2 -islands grown on $\text{Si}(111)$ with an STM-tip. The conductance per unit area was found to increase with decreasing diode area. These observations are explained by a generally applicable model, describing the potential barrier shape in ultra small Schottky diodes. It is shown that for diodes smaller than a characteristic length l_c (associated with the semiconductor doping level) the conventional description no longer holds. For such small diodes the Schottky barrier thickness decreases with decreasing diode size. As a consequence, the resistance of the diode is strongly reduced, due to enhanced tunneling. Without the necessity of assuming a reduced (non-bulk) Schottky barrier height, this effect provides an explanation for the experimental observation of enhanced conductance in small Schottky diodes.*

2.1 Introduction

Electrical transport through metal-semiconductor interfaces has received tremendous interest in the past decades, both experimentally and theoretically. This interest is of course greatly stimulated by the huge importance of such a heterojunction in the computer industry. In addition, the effect of downsizing the dimensions of a device on its electrical transport properties is an important topic today. Extremely small diodes have

*This chapter is based on the following papers: G. D. J. Smit, S. Rogge, and T. M. Klapwijk, *Appl. Phys. Lett.* **80**(14), 2568 (2002) and G. D. J. Smit, S. Rogge, and T. M. Klapwijk, *Appl. Phys. Lett.* **81**(20), 3852 (2002).

been experimentally realized and characterized in various systems, e.g. carbon nanotube heterojunctions [1] and junctions between *p*-type and *n*-type Si nanowires [2]. These experiments showed several deviations from conventional diode behavior.

Only a few experiments have been reported, which purpose was to address the physics of downscaling metal-semiconductor contacts. In none of them epitaxial interfaces were used, although it is well-known that the Schottky barrier height (SBH) is an extremely sensitive function of the atomic structure of the interface (see e.g. Ref. 3). Scanning tunneling spectroscopy (STS) of metallic clusters on a semiconductor surface has been used to study small metal-semiconductor contacts [4]. In addition, experiments have been carried out in which the tip of a scanning tunneling microscope (STM) was used to contact a semiconductor surface [5, 6] or a metallic cluster on a semiconductor surface [7] to form a small Schottky contact. Various deviations from the large-diode models were revealed. One of them is enhanced conductance, which was interpreted as a lower effective barrier [5]. Besides the work that addresses a single small diode directly, measurements have been carried out on many small diodes in parallel [8, 9].

Next to the experimental work, a large amount of models and theories exist, addressing several aspects of metal-semiconductor interfaces. Most existing models are restricted to infinitely extending interfaces, expressed in the assumption that all parameters vary only in the direction perpendicular to the surface. However, when the interface-size is decreased, at some point the actual junction geometry becomes important and many of such models cease to apply. A few specific geometries have been analyzed. For instance, some modelling has been done in truly one-dimensional systems [10, 11] and extremely small diodes (less than ~ 100 atoms) have been studied in local density calculations [12, 13]. However, little work has been done on modelling the effects of downscaling a conventional diode, in the regime where quantum confinement does not play a role.

In this chapter, we will present measurements of electrical transport through an epitaxial, nanometer sized metal-semiconductor interface. The $\text{CoSi}_2/\text{Si}(111)$ -interface used in our experiments is among the few metal-semiconductor interfaces of which reliable SBH values exist, mainly because it can be grown as a virtually perfect, abrupt, epitaxial interface [14], in which the atomic arrangement is well-determined. The SBH in this system is 0.67 eV (for *n*-type Si) and has been measured with various techniques [14, 15, 16]. It is therefore a nearly ideal system to study electrical properties of metal-semiconductor interfaces and has been intensely used for that purpose.

We will also present a simple model (based on the Poisson equation) describing the barrier shape in a diode, that is readily applicable to arbitrarily shaped small junctions. In particular, this model will be applied to explain several aspects of our measurements. Our model is related to existing models describing inhomogeneities in the Schottky barrier height (SBH) in large diodes [17], barrier shapes in small semiconducting grains [18] and charge transfer to supported metal particles [19]. Although we restrict ourselves to metal-semiconductor junctions, a similar model can be developed for, e.g., *pn*-junctions. The main result is that if the size of the metal-semiconductor interface is smaller than a certain characteristic length l_c , the thickness of the barrier is no longer determined by the doping level or the free carrier concentration, but instead by the size and shape of the diode. The resulting thin barrier in small diodes will give rise to enhanced tunneling, qualitatively explaining measurements of enhanced conductance [5, 6, 20] and making the

(often unjustified) assumption of a reduced SBH unnecessary. Moreover, experimentally observed scaling behavior and deviating IV -curve shapes [20] can be explained.

2.2 Theory

The transport properties of a Schottky diode are governed by the potential landscape which has to be traversed by the charge carriers. In order to derive the relevant length scale and study the general physical phenomenon, we start by analyzing an easily scalable and highly symmetrical model system, namely a metallic sphere embedded in semiconductor (see Figure 2.1, upper left inset). This model system allows for studying the scaling properties of a diode by calculating various properties of the system as a function of the radius a of the metallic sphere. The radius a is used as a measure for the interface size: for large a , we should find the well known results for a conventional diode, while decreasing a gives the opportunity to study finite size effects. An advantage of the high symmetry is that many physical properties can be expressed in explicit formulae.

2.2.1 Barrier shape

We start by calculating the barrier shape in the semiconductor in this model-structure. The (initial) SBH φ_B is accounted for in boundary conditions and is considered as a given quantity. For simplicity, the depletion approximation [21] is adopted, which assumes that the space charge region is depleted from charge carriers. It is a valid assumption as long as the position of the Fermi-energy in the barrier region is such that the free carrier concentrations are small compared to the doping concentration. This is true for the direction and amount of band bending in most common Schottky contacts, in particular for CoSi_2 on moderately to highly doped silicon. Moreover, the space charge region is assumed to be homogeneously charged. Deviations due to the limited validity of this assumption (discrete dopants) will be discussed in more detail in Chapter 4.

The barrier shape can be calculated by solving the Poisson equation in the semiconductor region with the appropriate boundary conditions. However, it is more illustrative to calculate the different contributions to the potential landscape by calculating electric fields with help of Gauss's law.

When the metallic sphere is embedded in a semiconductor with dielectric constant ϵ_s and has a total charge Q distributed over its surface, the electric field \mathcal{E}_1 due to this sphere as a function of radial coordinate r is

$$\mathcal{E}_1 = \frac{Q}{4\pi\epsilon_s r^2} \quad \text{for } r \geq a.$$

In the depletion approximation this charged sphere is surrounded by a uniform charge density (caused by ionized dopants) $\rho = \pm eN_d$, where N_d is the doping concentration and the sign depends on the doping type. For the remainder of this derivation the doping is assumed to be n -type. The electric field \mathcal{E}_2 due to the homogeneously charged thick spherical shell extending from $r = a$ to $r = a + w$ (where w has to be determined yet) is

12 | Scaling of Schottky diodes

given by

$$\mathcal{E}_2 = \frac{eN_d}{3\epsilon_s} \left(r - \frac{a^3}{r^2} \right).$$

As the total electric field must vanish outside the depletion region, the total enclosed charge must be zero, so $Q = -eN_d \frac{4}{3} \pi ((a+w)^3 - a^3)$. Therefore, the total electric field in the region $a < r < a+w$ is

$$\mathcal{E} = \mathcal{E}_1 + \mathcal{E}_2 = \frac{eN_d}{3\epsilon_s} \left(\frac{(a+w)^3}{r^2} - r \right)$$

while $\mathcal{E} = 0$ for $r > a+w$. Because $\mathcal{E} = -dV/dr$, this can be integrated to obtain the potential

$$V(x) = - \int_{a+x}^{a+w} \mathcal{E} dr = \frac{eN_d}{3\epsilon} \left(\frac{3(a+w)^2}{2} - \frac{(a+w)^3}{a+x} - \frac{(a+x)^2}{2} \right),$$

where $x = r - a$, the distance from the charged sphere. This equation can be rewritten as

$$\frac{e}{kT} \cdot V(x) = \frac{1}{2L_D^2} \left[(a+w)^2 - \frac{2(a+w)^3}{3(a+x)} - \frac{(a+x)^2}{3} \right] \quad \text{for } 0 \leq x \leq w, \quad (2.1)$$

where $L_D = \sqrt{\epsilon_s kT / (e^2 N_d)}$ is the Debye length. The Debye length is an important length scale in semiconductors, that indicates the distance over which distortions in the potential are screened by free carriers. The zero-point of the potential is chosen in the semiconductor bulk. The value of the depletion width w is fixed by the second boundary condition $V(0) = V_s$, where V_s is the total potential drop over the space charge region and satisfies $V_s = (\varphi_B - \varphi_s)/e - V$ (here $\varphi_s = E_C - E_F$ is the distance from Fermi-level to conduction band in the bulk and V is the applied bias). For p -type semiconductors a similar equation applies. Eq. (2.1) is valid for small bias voltage V . The limited validity of the depletion approximation at finite temperatures only affects the tail of the barrier (where $|V(x)| \lesssim kT$), which is unimportant for the transport properties.

From the Eq. (2.1), it can be seen that the characteristic length scale of this system is

$$l_c \stackrel{\text{def}}{=} L_D \sqrt{2eV_s/kT} = \sqrt{\frac{2\epsilon_s V_s}{eN_d}}. \quad (2.2)$$

This characteristic length is obviously strongly related to L_D . By comparing the diode size a to l_c we can decide whether the diode is ‘small’ or ‘large’. The value of l_c mainly depends on the doping level. In the lower right inset of Figure 2.1 the value of l_c is plotted versus doping concentration N_d for a fixed value of V_s .

Now we will use the expression for the barrier shape (Eq. (2.1)) to analyze the behavior of some physical quantities of interest. Next to the SBH, an important quantity for electrical transport is the Schottky barrier thickness. In Figure 2.1, the barrier full width at half maximum (FWHM, $x_{1/2}$) calculated from Eq. (2.1) is plotted as a function of diode size a . From the figure it is clear that for $a \gg l_c$ the value of $x_{1/2}$ approaches a constant, which was expected for a large diode. Indeed, for $a \gg l_c$, Eq. (2.1) reduces to

$$V(x) = -\frac{eN_d}{2\epsilon_s} (x-w)^2,$$

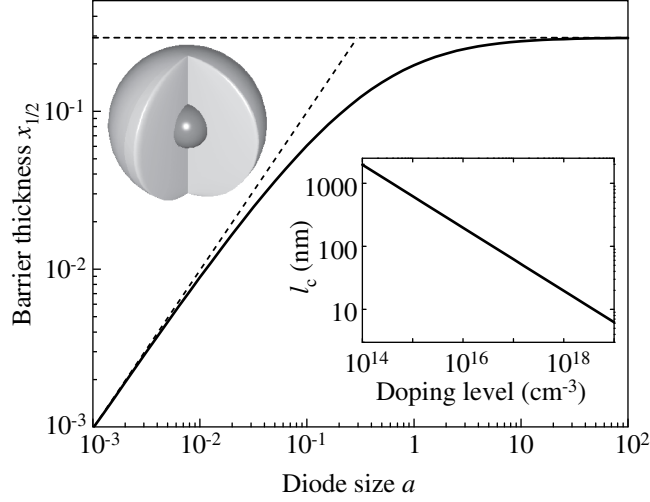


Figure 2.1 Plot of the calculated barrier FWHM $x_{1/2}$ as a function of diode size a [based on Eq. (2.1)], both in units of l_c . The dashed lines represent the asymptotic values for $a \gg l_c$ (conventional or ‘large’ diode) and $a \ll l_c$ (new regime, ‘small’ diode) respectively. The lower right inset is a plot of l_c as a function of doping level N_d in silicon ($\epsilon_s = 11.7$) for $\varphi_B = 0.67$ eV and $T = 300$ K. The upper left inset shows the model system, a metallic sphere embedded in semiconductor.

which is the well-known textbook [21] result for band bending in the depletion approximation for an infinitely large diode. Both the depletion width $w = \sqrt{(2\epsilon_s/eN_d)V_s} = l_c$ and $x_{1/2} = (\sqrt{2} - 1)w$ are in that regime independent of a .

Figure 2.1 shows that for $a \lesssim l_c$ the value of $x_{1/2}$ is no longer constant, but decreases with decreasing a . For $a \ll l_c$ it approaches $x_{1/2} = a$, i.e. the barrier thickness equals the diode size. This also follows from Eq. (2.1), which reduces for $a \ll l_c$ to

$$V(x) = V_s \cdot a/(a + x),$$

at least in the region $x \ll w$ (that is, close to the interface). Note that this is exactly the potential due to the charged sphere only. In this regime, the effect of the semiconductor space charge on the barrier shape and thickness can apparently be neglected*. This can be understood from the fact that the screening due to the space charge region takes place on a length scale l_c , as in conventional (large) diodes. However, from Gauss’s law it follows that any charged object of typical size $d < \infty$ in a dielectric medium gives rise to a potential that behaves roughly as $V(r) \propto d/r$. This Coulomb potential can be further screened by the formation of a space charge layer of opposite sign, but that additional screening can be neglected if $d \ll l_c$. This observation does not only hold for a sphere, but for *any* interface with typical dimensions much smaller than l_c .

*Note that the barrier shape is still *implicitly* dependent on N_d via V_s as it influences the Fermi-level position in the semiconductor bulk

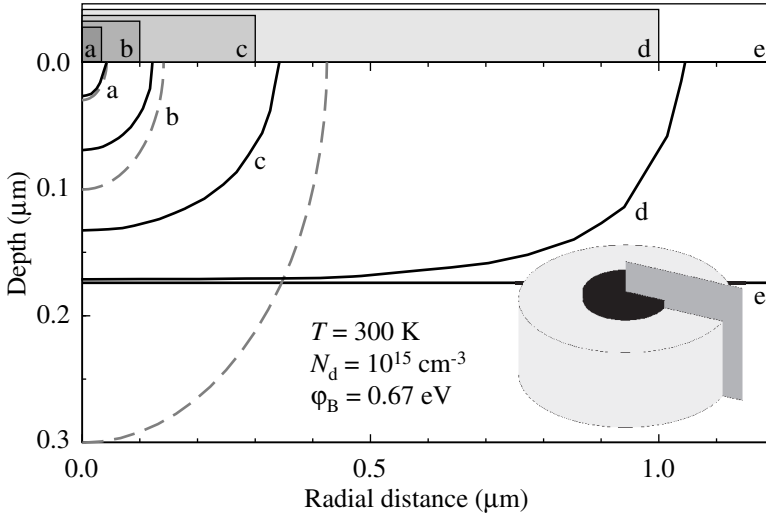


Figure 2.2 The solid lines are contours of the barrier FWHM for various disc-shaped contacts (see inset; radii ranging from 30 nm (a) to infinite (e)), taken from a numerical solution of the Poisson equation in silicon. It clearly shows the contact size dependence for contact radii smaller than $l_c \sim 750 \text{ nm}$. The dashed lines are the FWHM-contours of the barrier for the three smallest diodes, which would result from neglecting the screening effect of the semiconductor space charge region. This illustrates the point that for the smallest diodes, the space charge region has a negligible effect on the barrier shape. Note that the scales of both axes are not equal. The inset indicates the plane of cross-section shown in the figure.

To further illustrate this point, we must step away from this idealized model system. In a geometry that can actually be realized in an experiment, the Poisson equation must be solved numerically. We have done this, as an example, for n -doped silicon ($N_d = 10^{15} \text{ cm}^{-3}$) in contact with metallic circular disks of various radii. In this and all further calculations $\phi_B = 0.67 \text{ eV}$ was used, which is the barrier height of the $\text{CoSi}_2/\text{Si}(111)$ -interface [14]. Figure 2.2 shows the FWHM-contours of the barriers as resulting from these calculations. Also shown are the FWHM-contours of the barrier due to the metallic contacts only, illustrating the negligible effect of the space charge region on the barrier thickness in very small diodes*.

Note again that our description of small diodes has some similarity to that of SBH-inhomogeneities in large diodes as analyzed by Tung [17]. There, the effect of small patches with lower SBH on the space charge region is found to extend for only a few times the size of these patches.

The image charge effect [21], which results in barrier lowering, was neglected so far. However, inclusion of this effect would only enhance the phenomenon mentioned above,

*This effect is closely related to the action of small gates (see Chapter 8).

as it reduces the effective barrier height and width even further, especially in barriers which are narrow already.

One more issue that needs attention is the discrete nature of doping. In our analysis, the dopant atoms play a role in determining the Fermi-level position in the semiconductor bulk and were considered to provide a homogeneous space charge region. However, for the typical parameters of our experiments $N_d = 10^{15} \text{ cm}^{-3}$ and $a = 30 \text{ nm}$ (so $a \ll l_c$) the volume in which the potential drops to half its initial value contains approximately one doping atom. Discrete energy levels of such a doping atom cannot be resolved at room temperature. More importantly, the potential well due to an ionized single dopant will locally distort the barrier shape. This complicates the potential landscape, but it can only significantly increase the conductance of the diode, when the dopant resides close to the interface. In Chapter 4, this effect will be discussed in much more detail.

2.2.2 Transport

The shape of the barrier has consequences for electrical transport. The advantage of a Schottky-contact over a pn -junction is that transport properties are easier to model, because only one type of charge-carriers needs to be considered. These carriers are (driven by a bias voltage) transported to the other side of the barrier by either thermionic emission over the barrier or tunneling through the barrier. In general, thermionic emission is the dominant transport process for low to moderately doped semiconductors at room temperature. Only for highly doped semiconductors (thin barrier) or at low temperatures (thermionic emission cut off) tunneling becomes important.

From the discussion in the preceding section it is clear, that for very small Schottky-contacts the barrier can be very thin, even when the semiconductor is lowly doped. The main consequence for electrical transport is, that the narrow barrier in small diodes can make tunneling the dominant transport mechanism (instead of thermionic emission) even at very low doping levels.

To study the effect of the reduced barrier width on the transport properties of a small Schottky diode, a transmission coefficient $T(E, V)$ was obtained for the barrier shape from Eq. (2.1). This was done in a one-dimensional fully quantum mechanical calculation [22]. Note that $T(E, V)$ is implicitly dependent on temperature and doping level, because these quantities influence the position of the Fermi-level in the bulk semiconductor. The current density is then given by

$$J(V) \propto \int_0^{\infty} T(E, V) [f(\varphi_s + E) - f(\varphi_s + E + V)] dE,$$

from which it follows that the zero bias differential conductance satisfies

$$\left. \frac{dJ}{dV} \right|_{V=0} \propto - \int_0^{\infty} T(E, V) f'(\varphi_s + E) dE.$$

Here, f is the Fermi-Dirac distribution function and E the energy at which the electron transfer takes place, measured with respect to the semiconductor conduction band edge.

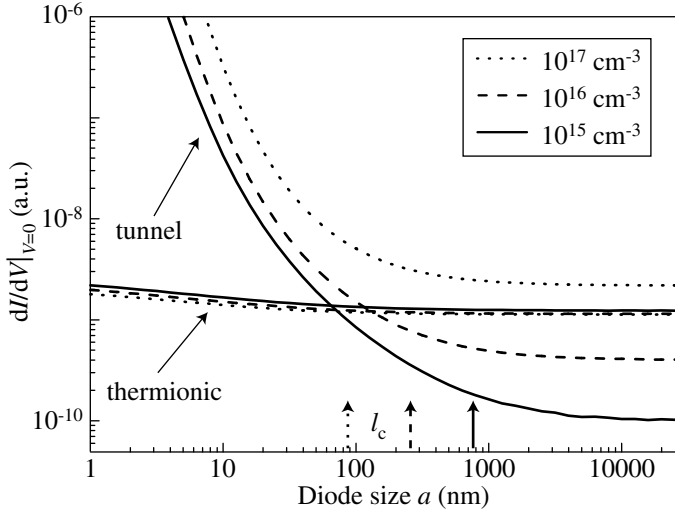


Figure 2.3 The (room temperature) contributions of tunneling and thermionic emission to the zero bias differential conductance, plotted as a function of diode size a for various doping concentrations. The vertical arrows indicate the values of l_c . The parameters are the same as in Figure 2.2.

Transport due to electrons at energies below the barrier maximum ($E < V_s$) is regarded as tunneling, while for $E > V_s$ we speak of thermionic emission. Obviously, the contribution of thermionic emission is almost independent of the barrier thickness, while tunneling is strongly dependent on the barrier thickness.

In Figure 2.3, the calculated zero bias differential conductance is plotted as a function of diode size a for several values of N_d . For $a \gtrsim l_c$ this quantity is independent of a . For smaller values, the tunnel current starts to increase rapidly, eventually leading to a strong increase of the total conductance.

Moreover, the shape of the current-voltage (IV) curves changes with decreasing diode size. Our calculations (Fig. 2.4) show that for large diodes the IV -curve has exactly its expected exponential shape $I = I_0[\exp(eV/kT) - 1]$. Apart from the total current increase, in small diodes the relative contribution of the reverse current starts to increase and eventually—in extremely small diodes—the reverse current exceeds the forward current, thus reversing the rectifying behavior of the diode. Notice that this effect generally already occurs at large diode sizes, due to the presence of edges and vertices.

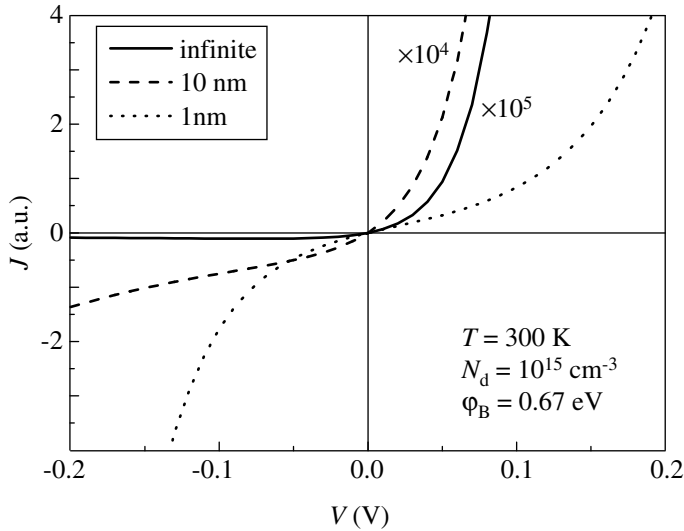


Figure 2.4 Calculated JV -curves for various diode sizes. The large diode curve has the expected exponential shape. The qualitative appearance of the curves changes drastically with decreasing diode size. The curves of the larger diodes have been scaled vertically.

2.3 Experiments

2.3.1 Sample preparation and characterization

All experiments were performed in an ultra high vacuum (UHV) system with a base pressure of $5 \cdot 10^{-11}$ mbar. Si samples, diced from standard 4''-wafers and with n -type doping (resistivity either $10 \Omega\text{cm}$ or $0.01 \Omega\text{cm}$) have been used as substrate. They were loaded into the system without chemical cleaning and thoroughly outgassed at $550 \text{ }^\circ\text{C}$. After flashing the sample to $1200 \text{ }^\circ\text{C}$ several times, it was slowly ($1 \text{ }^\circ\text{C/s}$) cooled down to room temperature to yield a clean 7×7 -reconstructed Si(111) surface (checked by STM). Heating of the silicon was achieved by passing a current through the sample.

It has been reported that a significant amount of acceptor-like impurities can be incorporated in the top layer of the substrate during sample flashing at $1200 \text{ }^\circ\text{C}$ in UHV [23], effectively reversing the doping to p -type in (initially) n -type low-doped samples. Nevertheless, the concentration of these possible p -type dopants is expected to be so low that it does not affect our main arguments.

About 0.3 monolayers of Co atoms were evaporated onto the surface which was held at room temperature. Then the sample was subsequently annealed at $800 \text{ }^\circ\text{C}$ for about 5 min, so that hexagon-shaped epitaxial CoSi_2 -islands were formed (Fig. 2.5(a)). The height of the islands ranged from 2–4 nm with respect to the silicon surface, while the diameters were in the range 15–40 nm. The inter-island distances were much larger than the island

diameters (see Fig. 2.5(c)). The average dimensions of the islands and the spread therein depends on the terrace width and slightly on the amount of Co on the surface and the annealing procedure. The values given here apply to the measurements presented in this chapter.

The atomically flat surface and straight edges of the islands confirm that they are perfectly crystalline. The alignment of the edges with the main crystallographic directions confirms the epitaxial growth. From TEM-studies, it has been shown that CoSi_2 -islands grow on top of the Si-substrate [24], although they were grown by a method slightly different from ours. If in our case the CoSi_2 -islands would grow *into* the substrate, the three occurring $\text{CoSi}_2/\text{Si}(100)$ -interfaces [25] do have the same SBH as the $\text{CoSi}_2/\text{Si}(111)$ interfaces [26, 27].

From the STM-image, it can be seen that two different surface reconstructions coexist on the surface, well separated from each other (Fig. 2.5(d)). One is easily recognized as the well-known 7×7 -reconstruction of the clean $\text{Si}(111)$ -surface. The other is an irregular Co-induced reconstruction which will be referred to as the Co-induced 1×1 -reconstruction [25].

As the final preparation step, the Si-surface reconstruction was destroyed by exposing the surface to atomic hydrogen for 10 min at a pressure of 10^{-6} mbar, while the surface was held at 400°C , followed by a fast cool-down. This procedure was necessary to decrease the effect of surface related conduction channels as will be discussed later.

2.3.2 Measurements

The *IV*-measurements were done (at room temperature) by positioning the STM-tip over an island. After switching off the feedback loop, the tip was lowered by a distance Δz , sufficient to make contact to the island. Then the current was measured while ramping the voltage. The appropriate value of Δz was determined by lowering the tip at a fixed bias and measuring the current. After the expected initial exponential increase, the current saturated at a constant value when the tip was lowered by $\sim 9 \text{ \AA}$. To ensure good contact, in all *IV*-measurements $\Delta z = 15 \text{ \AA}$ was used. The voltage ramping speed was typically $10 - 100 \text{ V/s}$, which is slow compared to the *RC*-time of the system ($\sim 1 \text{ ms}$). This is confirmed by the absence of hysteresis in the measurements. The current measurements were limited to 50 nA by the *in situ IV*-converter.

A schematic representation of the procedure in a single measurement is depicted in Fig. 2.6. The voltage ramp was generated by a digital function generator. Both the applied voltage and the output of the *IV*-converter were simultaneously measured by 16-bit analogue-to-digital converters in a data-acquisition card (see Fig. 2.7).

Carefully ‘crashing’ the STM-tip for *IV*-measurements in this way did hardly deteriorate the imaging quality of the STM-tip (Fig. 2.5(b)). When repeating the measurement on different positions on the same island, the *IV*-curves reproduced perfectly. From this, it can be concluded that the resistance of the (ill-defined and expected-to-be-irreproducible) tip-island contact is negligible compared to the total resistance. This is supported by the fact that the electrochemically etched tungsten STM-tips were prepared to be contaminant and oxide-free by *in situ* annealing and self-sputtering with Ne. Since both CoSi_2

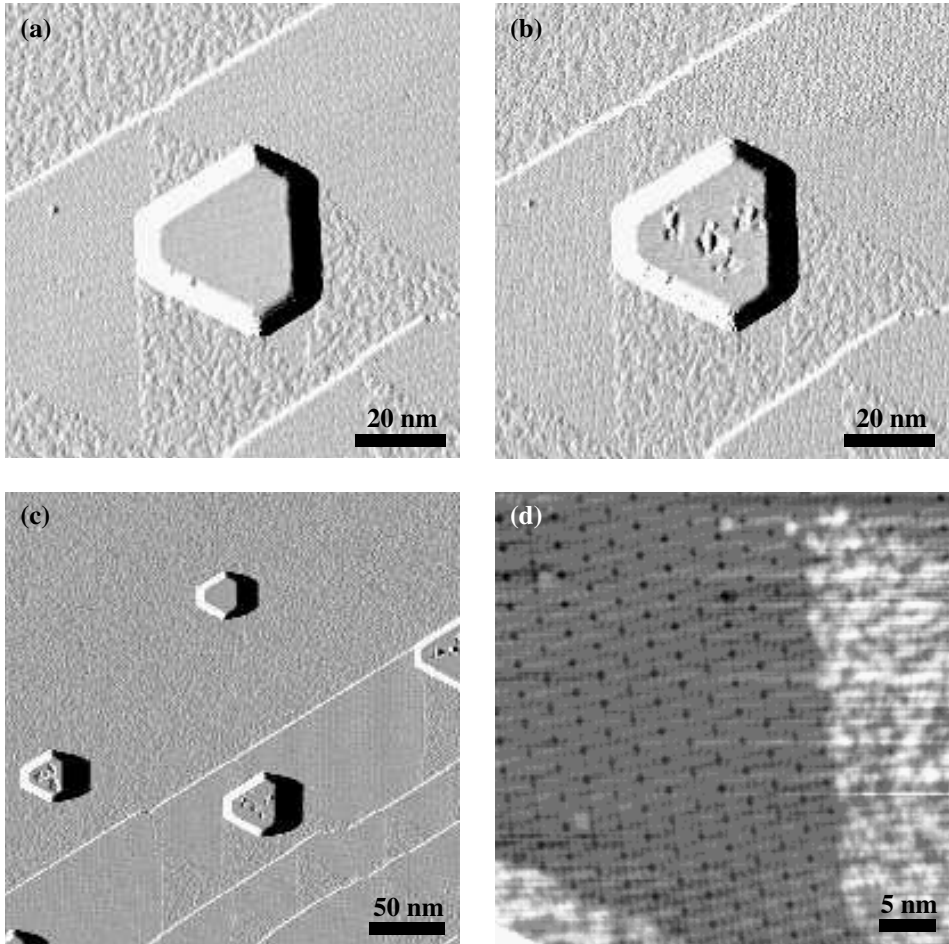


Figure 2.5 (a) STM (current-)image of a typical CoSi_2 -island. The height of this island is 2.3 nm. (b) The same island after a few IV -measurements, clearly showing the imprints of the STM-tip. This image also demonstrates that the measurements do not destroy the imaging quality of the tip. (c) Zoom-out of the same area, showing the well-separated islands, some of which have been contacted for measurements. (d) Height-image of a detail of the sample surface, showing the 7×7 -reconstruction of the clean Si(111)-surface, as well as adjacent areas with the Co-induced reconstruction. All images were taken with sample bias $V = +2 \text{ V}$ and set-point current $I = 0.1 \text{ nA}$.

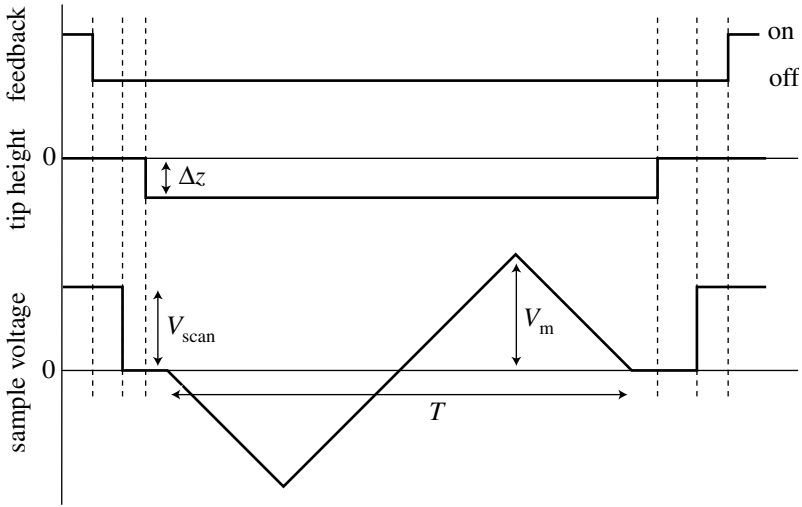


Figure 2.6 Schematic overview of a single measurement procedure, indicating the order of events. The sweep-time T was usually around 150 ms. The maximum bias voltage V_m was chosen in such a way that the largest current was close to the allowed 50 nA.

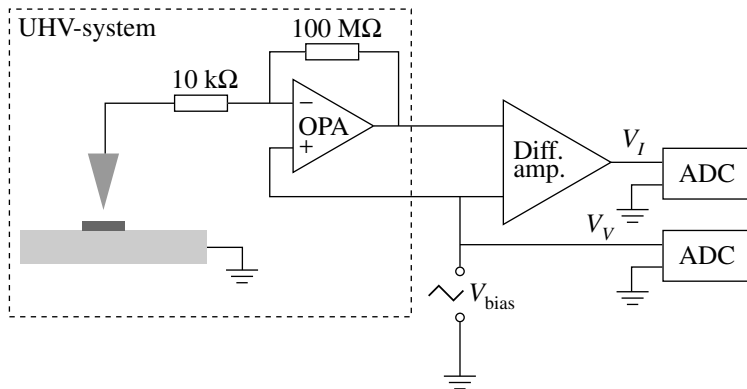


Figure 2.7 Schematic diagram of electronic measurement circuit. The bias voltage V_{bias} is generated by a function generator. The voltages V_I (proportional to the current) and V_V (measured bias voltage) are digitized by two analogue-to-digital converters in a data acquisition card.

and the tip are metallic, no barrier at the tip-island interface is expected. Furthermore, the resistance of the back-contact on the sample was measured to be at most a few $k\Omega$. The spreading resistance from the island to the substrate is also estimated to be negligible. Therefore, we can be sure that we are really probing the properties of the island-substrate interface. The advantage of this type of measurement (as compared to the usual STS) is that the measurements are not dominated by the properties of the surfaces at either side of the vacuum-gap, but instead it is possible to directly probe the properties of the buried metal-semiconductor interface.

As mentioned before, two different surface reconstructions coexist on our samples after preparation. Some islands are completely surrounded by the Co-induced 1×1 -reconstruction, while others partly border 7×7 -reconstructed surface areas (see Fig. 2.5). IV -curves on the former type of islands yielded on average a significantly higher resistance than measurements on the latter type. This is presumably due to either surface conduction [28] or environmental Fermi-level pinning resulting in additional band bending. For this reason, in all presented measurements the surface reconstruction was first destroyed by exposing it to atomic hydrogen, as described before. This treatment always led to a decreased conductance, apparently reducing the contribution of a surface-related transport channel. Measurements on the same sample always gave consistent results after this procedure*.

The range of island sizes that can be fabricated in the self-assembling growth process is limited. In the measurements presented in this chapter, this range is approximately 15–40 nm for the island diameters. Still, both the small and the large diode regime can be addressed by varying the doping level. Indeed, on the $10 \Omega\text{cm}$ substrate, where the doping level predicts a screening length of about $1 \mu\text{m}$, we are far into the small-diode regime. On the $0.01 \Omega\text{cm}$ substrate (screening length $\sim 10 \text{ nm}$) we are just at the other side of the crossover.

2.4 Results and discussion

Fig. 2.8 shows a few typical measurements on the low-doped sample. As expected, it was impossible to fit our IV -data of the small diodes to the standard diode equation $I \propto [\exp(eV/kT) - 1]$, even at small bias. This indicates that indeed the dominant transport process is not thermionic emission, here. A further clear manifestation of the special behavior of small diodes is the much higher conductance than expected from downscaling a conventional diode. From a typical IV -curve acquired on a small diode ($10 \Omega\text{cm}$ substrate), a specific contact resistance R_c (the zero-bias differential resistance multiplied by the island area) of $1 \cdot 10^{-2} \Omega\text{cm}^2$ was derived. This is four orders of magnitude smaller than for conventional diodes with a barrier height of 0.67 eV [21, 27]. Considering the facts that in a conventional diode on a $10 \Omega\text{cm}$ substrate $J_{\text{th}}/J_{\text{T}}$ (ratio of thermionic and tunnel current) is expected to be roughly 10^{10} [29] and that J_{th} is independent of the barrier thickness, the total current increase requires an increase of the tunnel current by a

*Comparison of measurements on samples from different fabrication runs was not straightforward, because the procedure of hydrogen exposure was not perfectly reproducible.

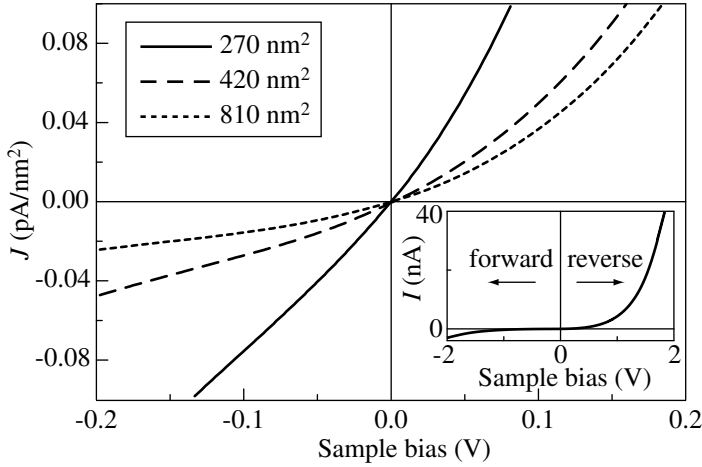


Figure 2.8 Measured average current *density* for various island sizes on the $10\ \Omega\text{cm}$ substrate. Smaller islands have larger current densities due to the narrower barrier. The inset shows the full *IV*-curve for the $810\ \text{nm}^2$ island, demonstrating that the current increases faster with reverse bias than with forward bias.

striking factor of $\sim 10^{14}$. Due to the sensitivity of the tunnel current on the barrier thickness, such a large increase can reasonably well be explained by a considerably reduced barrier thickness.

Besides, pure thermionic emission would lead to a saturation current at positive sample bias of approximately $1 \cdot 10^{-7}$ nA for this SBH [21]. The observed current is, however, much larger. This also indicates the presence of an important, additional conduction path. Note that it is not necessary to assume a *lower* SBH to explain our data.

To further test our hypothesis, the dependence of the (small-bias) conductance on the island area was studied. The large diodes ($0.01\ \Omega\text{cm}$ substrate) behaved as expected: the barrier thickness is determined by L_D and therefore independent of the diode size. A larger diode area leads straightforwardly to a larger conductance (see Fig. 2.9). The observed current-area dependence is not perfectly linear, which is presumably due to the contribution of the edges, which are not included in our simple model. (Deviation that are due to randomly positioned dopants are treated in Chapter 4.) Due to the high doping level there will be a significant amount of tunneling in these diodes. For that reason, the *IV*-curves do not behave according to the standard diode equation $I = I_0[\exp(eV/kT) - 1]$.

The small diodes show a different dependence on island area. The measurements in Fig. 2.8 show that in small diodes the conductance *per unit area* decreases with increasing diode area. To demonstrate this trend even clearer, in Fig. 2.10 the measured zero-bias conductance per unit area is plotted versus island size. This figure is fully consistent with our model, which predicts a thicker barrier for larger interfaces, leading to a decreasing contribution of the tunnel current.

Finally, we want to mention the behavior of small diodes at large bias. In conventional diodes, the current saturates at reverse bias. At forward bias, after the initial exponential

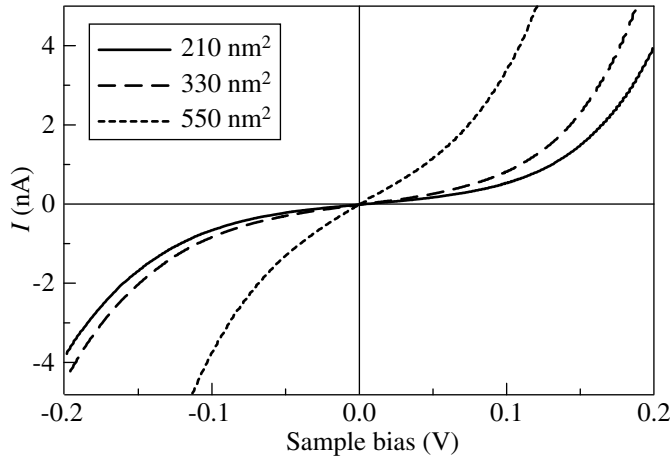


Figure 2.9 Measured IV -curves for various island sizes on the $0.01 \Omega\text{cm}$ substrate. The zero-bias conductance is increases with increasing island size, as can be expected from a conventional diode.

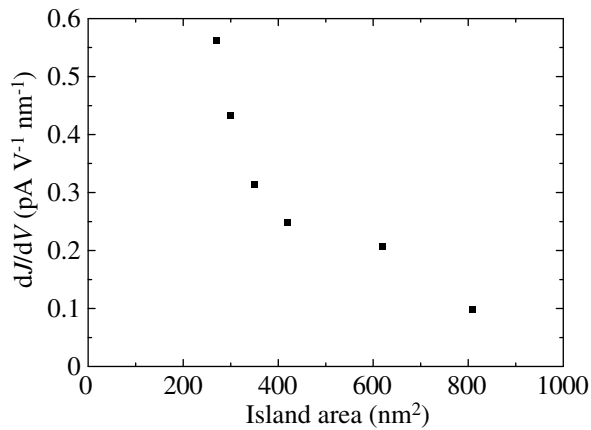


Figure 2.10 Zero-bias differential conductance per unit area as a function of island area on a low doped ($10 \Omega\text{cm}$) sample. The trend of higher current density for smaller islands is clearly observed. The error in each point is much smaller than the distance between the points.

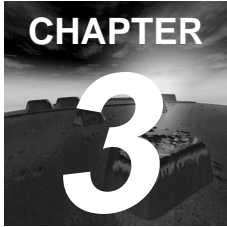
increase, the current is limited by the serial resistance of the bulk semiconductor. In our small diodes, the situation is completely different. From the inset in Fig. 2.8 it can be seen that the expected diode operation is even reversed: the measured current at forward (negative) bias is smaller than at reverse bias. As explained in Section 2.2.2, this behavior can be understood from the fact that the barrier thickness decreases fast in reverse bias for initially thin barriers. The effect is even enhanced by taking into account the related process of Fowler-Nordheim tunneling from the diode's edges at positive sample bias.

2.5 Conclusion

In conclusion, we have measured electrical transport through epitaxial nanometer scale metal-semiconductor interfaces. Both the observed high zero-bias conductance and the dependence of the zero-bias conductance on the diode area support our model for the extent of the space charge region for interface sizes smaller than the free carrier screening length. By a simple electrostatic argument, it demonstrates that the Schottky barrier thickness becomes a function of the diode size for small diodes (e.g. smaller than $l_c \approx 80$ nm for $N_d = 10^{17}$ cm⁻³). Consequently, the contribution of tunneling to the total conductance is greatly enhanced in small diodes. This effect can explain several experimental results [5, 6, 20], without the assumption of a reduced SBH. Finally, we found that small diodes show *IV*-curve shapes that qualitatively differ from those of conventional diodes.

- [1] Z. Yao, H. W. C. Postma, L. Balents, and C. Dekker, *Nature* **402**, 273 (1999).
- [2] Y. Cui and C. M. Lieber, *Science* **291**, 851 (2001).
- [3] D. R. Heslinga, H. H. Weitering, D. P. van der Werf, T. M. Klapwijk, and T. Hibma, *Phys. Rev. Lett.* **64**, 1589 (1990).
- [4] D. L. Carroll, M. Wagner, M. Rühle, and D. A. Bonnelli, *Phys. Rev. B* **55**, 9792 (1997).
- [5] P. Avouris, I.-W. Lyo, and Y. Hasegawa, *J. Vac. Sci. Technol. A* **11**, 1725 (1993).
- [6] R. Hasunuma, T. Komeda, and H. Tokumoto, *Appl. Surf. Sci.* **130–132**, 84 (1998).
- [7] H. Hasegawa, T. Sato, and C. Kaneshiro, *J. Vac. Sci. Technol. B* **17**, 1856 (1999).
- [8] S. Doniach, K. K. Chin, I. Lindau, and W. E. Spicer, *Phys. Rev. Lett.* **58**, 591 (1987).
- [9] W. Yang, F. J. Jedema, H. Ade, and R. J. Nemanich, *Thin Solid Films* **308–309**, 627 (1997).
- [10] F. Léonard and J. Tersoff, *Phys. Rev. Lett.* **83**, 5174 (1999).
- [11] A. A. Odintsov, *Phys. Rev. Lett.* **85**, 150 (2000).
- [12] V. G. Zavodinsky and I. A. Kuyanov, *J. Appl. Phys.* **81**, 2715 (1997).
- [13] U. Landman, R. N. Barnett, A. G. Scherbakov, and P. Avouris, *Phys. Rev. Lett.* **85**, 1958 (2000).
- [14] R. T. Tung, *Mater. Chem. Phys.* **32**, 107 (1992).
- [15] W. J. Kaiser, M. H. Hecht, R. W. Fathauer, L. D. Bell, E. Y. Lee, and L. C. Davis, *Phys. Rev. B* **44**, 6546 (1991).

- [16] H. von Känel, T. Meyer, and M. Klemenc, *J. Electron Spectrosc.* **109**, 197 (2000).
- [17] R. T. Tung, *Phys. Rev. B* **45**, 13509 (1992).
- [18] C. Malagu, V. Guidi, M. Stefancich, M. Carotta, and G. Martinelli, *J. Appl. Phys.* **91**, 808 (2002).
- [19] T. Ioannides and X. Verykios, *J. Catal.* **161**, 560 (1996).
- [20] G. D. J. Smit, S. Rogge, and T. M. Klapwijk, *Appl. Phys. Lett.* **80**, 2568 (2002).
- [21] S. M. Sze, *Physics of Semiconductor Devices* (Wiley, New York, 1981), 2nd ed.
- [22] J. S. Walker and J. Gathright, *Am. J. Phys.* **62**, 408 (1994).
- [23] M. Liehr, M. Renier, R. A. Wachnik, and G. S. Scilla, *J. Appl. Phys.* **61**, 4619 (1987).
- [24] P. A. Bennett, D. J. Smith, and I. K. Robinson, *Appl. Surf. Sci.* **180**, 65 (2001).
- [25] B. Ilge, Ph.D. thesis, Delft University of Technology (2000).
- [26] R. T. Tung, *J. Vac. Sci. Technol. B* **2**, 465 (1984).
- [27] S. Zhu, R. L. van Meirhaege, C. Detavernier, F. Cardon, G.-P. Ru, X.-P. Qu, and B.-Z. Li, *Solid-State Electron.* **44**, 663 (2000).
- [28] Y. Hasegawa, I.-W. Lyo, and P. Avouris, *Surf. Sci.* **357–358**, 32 (1996).
- [29] C. Y. Chang and S. M. Sze, *Solid-State Electron.* **13**, 727 (1970).



Scaling of micro-fabricated nanometer-sized Schottky diodes

Abstract — Diodes on the nanometer scale generally show non-ideal transport characteristics. In this chapter, the transition of a conventional Schottky diode to a nano-diode is investigated. It is shown that electrostatic effects in small lithographically fabricated diodes can lead to a considerably thinner Schottky barrier, with the consequence of a greatly enhanced tunneling current. We present numerical simulations as well as analytical calculations of the potential barrier shape in small devices, demonstrating this scaling effect. Special focus is placed on the role of the interconnects.*

3.1 Introduction

As shown in the previous chapter, nanometer-size diodes generally show transport characteristics deviating from those of conventional diodes. For diodes which are much smaller than the characteristic length scale l_c (see Eq. 2.2), the barrier thickness is proportional to the diode size. For low doping concentrations (10^{15} cm^{-3}) the scaling effect needs already to be considered for diodes with a contact diameter of less than about

*This chapter is based on the following paper: G. D. J. Smit, M. G. Flokstra, S. Rogge, and T. M. Klapwijk, *Microelectronic Engineering* **64**(1–4), 429 (2002).

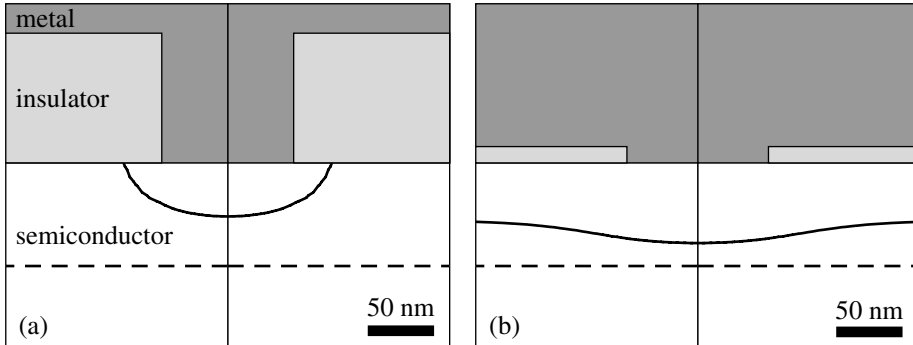


Figure 3.1 Results of our numerical calculations, plotted in a cross-section of a realistic layout for a nano-Schottky diode including interconnect. The devices are cylindrical symmetric around the middle vertical axis. The solids lines in the semiconductor region are contours of the FWHM of the barrier resulting from a numerical solution of the Poisson equation (see text). The dashed lines are contours of the FWHM of the barrier in a large diode, for otherwise equal parameters. In both structures $T = 300\text{ K}$, $\varphi_B = 0.67\text{ eV}$ and $N_D = 10^{16}\text{ cm}^{-3}$ were used. **(a)** The small-size effect on the barrier shape resulting in a reduced barrier thickness is clearly visible. Here the interconnect is separated from the semiconductor by a thick insulating layer with a small dielectric constant $\varepsilon_i = 2.5$ (e.g. PMMA). **(b)** When the insulating layer is thin and has a higher dielectric constant $\varepsilon_i = 3.9$ (e.g. SiO_2), the small-size effect on the barrier thickness is largely masked by the electrostatic effect of the interconnect.

800 nm, while for a more common concentration like 10^{17} cm^{-3} the cross-over length is about 80 nm.

In this chapter, our goal is to investigate the consequences of this effect for transport in lithographically fabricated diodes in the micrometer down to the nanometer length-scale. Simulations of the potential barrier shape in small realistic metal-semiconductor devices are reported, where special care is taken to understand the role of the interconnects which can mask the scaling behavior substantially.

3.2 Simulations and results

To study the occurrence of this scaling effect in a device layout that can be micro-fabricated, we have performed numerical calculations. For simplicity, a cylindrical symmetric contact was chosen. The Poisson equation was solved with a finite element method to yield the potential and the electron and hole concentrations at room temperature. The Schottky barrier height φ_B was considered as a given quantity and imposed as a boundary condition. The dopant concentration was assumed to be uniform and interface states at insulator-semiconductor interface were neglected.

The results of our calculations are presented in Fig. 3.1. Part (a) of this figure illustrates the scaling behavior of a nano-diode in a layout that can be realized by standard

micro-fabrication techniques. The diode shown has a radius of 50 nm, which is about equal to the Debye length L_D for the doping concentration used ($N_D = 10^{16} \text{ cm}^{-3}$). Due to the small size of this diode, the barrier is considerably thinner than for a corresponding large diode. This is consistent with the results in Chapter 2. However, Fig. 3.1(b) shows the same diode, the only difference being that the insulator between the large metal interconnect and the semiconductor is replaced by a 20 nm thick oxide layer. The electrostatic effect of the interconnect now causes an additional space charge region to appear below the insulator-semiconductor interface. This space charge strongly affects the barrier thickness of the diode. Here, the electrostatic influence of the large interconnect almost completely masks the scaling effect in the nanometer-sized Schottky diode. In contrast, the thicker insulation layer with a lower dielectric constant in Fig. 3.1(a) leaves the finite size effect clearly visible.

3.3 Discussion

To make an experimental study of the small-size effect in micro-fabricated Schottky diodes possible, the influence of the interconnect must be reduced as much as possible. Because interconnects are in general large and the insulating layer must be thicker than a few atomic layers, a standard approach [1] can be used to investigate the additional band bending caused by the interconnect. Apart from the additional insulating layer, the charge distribution in a conventional metal-insulator-semiconductor (MIS) structure is very similar to that in a Schottky diode. Solving the one-dimensional Poisson equation in this situation (assuming translational symmetry) straightforwardly gives the potential as a function of position. From this standard result an expression for the extent W of the depletion zone in the semiconductor can be deduced and is given by

$$W = d \cdot \frac{\varepsilon_s}{\varepsilon_i} \left(\sqrt{1 + \frac{2V_{\text{sm}}\varepsilon_i^2}{eN_D d^2 \varepsilon_s}} - 1 \right). \quad (3.1)$$

Here, ε_s and ε_i are the dielectric constants of the semiconductor and insulator respectively. V_{sm} is the potential difference between the metal-insulator interface and the semiconductor bulk, N_D is the dopant concentration, e is the electron charge and d is the thickness of the insulating layer.

Reducing the influence of the interconnects is equivalent to minimizing the value of W . To achieve this, a large fraction of the total potential difference between the metal and the semiconductor bulk should drop over the insulator. If we define $(1 - \alpha)$ as the fraction of the total potential difference that drops over the insulator, the minimal required thickness of the insulating layer d_{min} as a function of α is given by

$$d_{\text{min}} = \sqrt{\frac{V_{\text{sm}}\varepsilon_i^2}{2eN_D\varepsilon_s} \frac{(1 - \alpha)^2}{\alpha}}. \quad (3.2)$$

This function is plotted in Fig. 3.2. The results are in good agreement with the numerical calculations in Fig. 3.1, which were obtained for the same parameters.

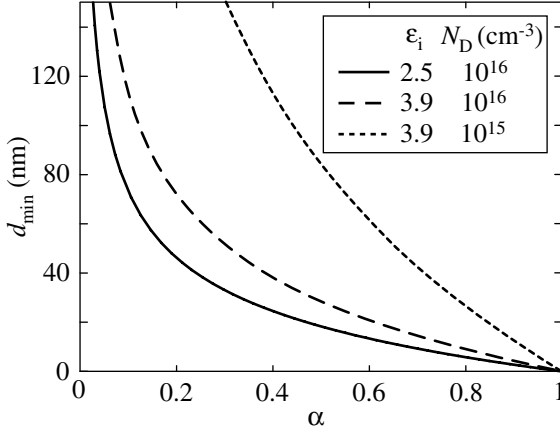


Figure 3.2 The minimal required insulator thickness d_{\min} as a function of α . The parameters of the first two curves are the same as for the nano-diodes in Fig. 3.1.

From Eq. (3.2) it is easily deduced that a small value of α requires N_D and d_{\min} to be large while ϵ_i must be small. These conclusions are intuitive, although the effect of the dopant concentration N_D needs some more discussion. Despite the fact that a large N_D decreases the distorting effect of the interconnect, a higher dopant concentration also requires a smaller diode to enter the anomalous scaling regime, since the Debye length is proportional to $1/\sqrt{N_D}$. As lithographically fabricated structures cannot be much smaller than about 50 nm in diameter, N_D must not be much higher than 10^{16} cm^{-3} . On the other hand, a lower value of N_D would require a much thicker insulating layer to reach the same value for α (see the last curve in Fig. 3.2), making fabrication much more difficult. Eq. (3.2) can be helpful to optimize the device parameters within such boundary conditions. Our calculations show that it is possible to tune the device parameters within realistic limits in such a way that the effect of the interconnect is reduced to $\alpha < 0.1$.

Throughout this paper, we assumed that φ_B is independent of the diode size. Only when a high quality epitaxial interface is used, one can be sure of a well-defined constant barrier height over the total contact area. A good example of an interface that meets these requirements is the $\text{CoSi}_2/\text{Si}(111)$ -interface [2]. On n -type silicon, it has a well-defined barrier height $\varphi_B = 0.67 \text{ eV}$ that has been measured with various techniques [2, 3, 4]. This value of φ_B was used in our calculations.

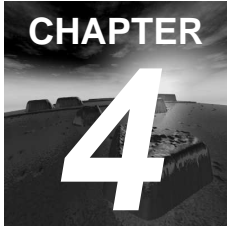
As mentioned before, interface states at the insulator-semiconductor interface and fixed charges in the insulator were neglected in our general analysis. However, depending on the choice of materials, these phenomena can readily occur. The presence of electronic states at the insulator-semiconductor interface would cause α to become independent of d and ϵ_i . Instead, α would be determined by Fermi-level pinning. Trapped charges in the insulator can cause additional band-bending, also changing the value of α . This shows that the determination of α can be more involved than sketched in Sec. 3. Nevertheless, the observability of the scaling effect still depends in the same way on α , i.e. on the rela-

tive position of the Fermi-level at the metal–semiconductor and insulator–semiconductor interfaces.

3.4 Conclusion

The different behavior of nanometer-sized metal-semiconductor interfaces compared to standard sized interfaces has been investigated by numerical simulation. Devices with a realistic layout in terms of interconnects and insulating layers on the 100 nm length scale clearly show a thinner Schottky barrier—leading to a more dominant tunneling current—than a conventional large diode. Interconnects play an important role as they can mask the scaling effect substantially. In very small diodes, this scaling effect allows for lithographic manipulation of the barrier thickness independent of the carrier concentration. The presented simulations demonstrate that the discussed scaling behavior can be measured in lithographically fabricated devices.

- [1] S. M. Sze, *Physics of Semiconductor Devices* (Wiley, New York, 1981), 2nd ed.
- [2] R. T. Tung, *Mater. Chem. Phys.* **32**, 107 (1992).
- [3] H. von Känel, T. Meyer, and M. Klemenc, *J. Electron Spectrosc.* **109**, 197 (2000).
- [4] W. J. Kaiser, M. H. Hecht, R. W. Fathauer, L. D. Bell, E. Y. Lee, and L. C. Davis, *Phys. Rev. B* **44**, 6546 (1991).



Conductance distribution in nanometer-sized semiconductor devices due to doping statistics

.....

Abstract — We show that individual dopant atoms dominate the transport characteristics of nanometer sized devices, by investigating metal semiconductor diodes down to 15 nm diameter. Room temperature measurements reveal a strongly increasing scatter in the device-to-device conductance towards smaller device sizes. The low-temperature measurements exhibit pronounced features, caused by resonant tunneling through electronic states of individual dopant atoms. We demonstrate by a statistical analysis that this behavior can be explained by the presence of randomly distributed individual dopant atoms in the space charge region.*

4.1 Introduction

In semiconductor physics, the influence of doping is generally accounted for by a homogeneous shift of the Fermi-level, caused by the introduction of free carriers in the

*This chapter is based on the following paper: G. D. J. Smit, S. Rogge, J. Caro, and T. M. Klapwijk, cond-mat/0309137 (2003), to be published in Phys. Rev. B.

semiconductor. However, when the dimensions of a device are small compared to the average distance between individual dopants, the discrete nature of doping must be taken into account. Each individual ionized dopant introduces a Coulomb potential well in the semiconductor, locally distorting the potential landscape. When the number of dopants in the volume of semiconductor that determines the transport characteristics of a device gets small, these random potential fluctuations cause atypical behavior of semiconductor devices [1]. As mentioned in Chapter 1, this is commonly viewed as one of the fundamental limits in the ongoing size-reduction of CMOS-technology [2, 3]. Mapping the positions of individual dopants [4] and the potential fluctuations they induce [5, 6] has been performed experimentally with various techniques. Furthermore, the influence of statistical fluctuations due to random dopants on device behavior has been subject of simulations [7].

In this chapter, we experimentally investigate the effects of the discreteness of doping on the transport properties of small diodes by comparing many identically prepared devices. We find that statistical fluctuations caused by randomly positioned individual dopant atoms do not average out for very small devices. In contrast, fluctuations dominate the electrical transport properties of the smallest devices and cause large differences in the conductance of nominally equal devices. Furthermore, we demonstrate that at low temperature the Coulomb well of a single dopant gives rise to a resonant tunneling channel.

4.2 Measurements

In order to allow for measuring the transport characteristics of many identically prepared diodes, we use self-assembly methods to fabricate epitaxial CoSi₂-diodes. The tip of a scanning tunneling microscope (STM) is used to characterize and access the devices individually.

All experiments are performed in an ultra-high vacuum (UHV) system with a base pressure of $5 \cdot 10^{-11}$ mbar. Self assembled CoSi₂-islands are grown on Si-substrates (resistivity 0.015 Ωcm, doping concentration around $2 \cdot 10^{18}$ cm⁻³) by evaporating a submonolayer of cobalt onto a clean 7×7 -reconstructed Si(111) surface, followed by an anneal at 800 °C for about 5 min. The resulting hexagon-shaped epitaxial CoSi₂-islands have heights in the range of 2–10 nm and diameters in the range of 15–80 nm. The inset of Fig. 4.2 displays an STM-image of a typical island. Each island is regarded as a nanometer sized epitaxial metal-semiconductor diode. The inter-island distances are roughly ten times larger than the island diameters. To minimize the effect of surface related transport channels, the 7×7 surface reconstruction surrounding the islands is destroyed by exposing it to atomic hydrogen for 10 min at a substrate temperature of 400 °C.

Current-voltage (*IV*) measurements are performed by positioning the STM-tip over an island. After switching off the feedback loop, the tip is lowered by 15 Å, which is found to be sufficient to make contact to the island. Then the current is measured while ramping the voltage, yielding well-reproducible *IV*-curves that reflect the properties of the metal-semiconductor contact. The sample preparation and measurements techniques are described in more detail in Chapter 2.

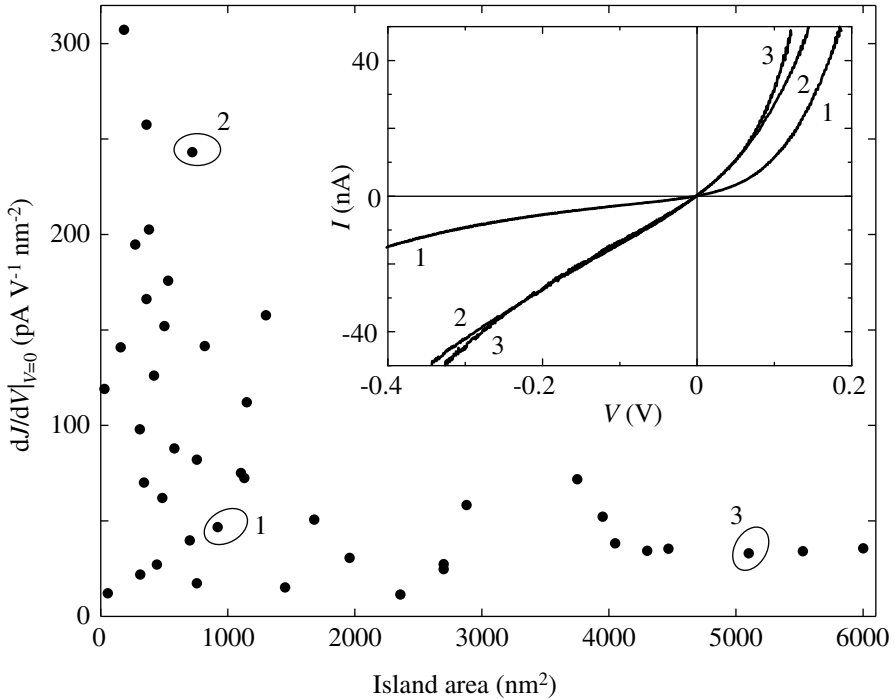


Figure 4.1 The zero bias conductance per unit area as a function of island area at room temperature. For large islands, the measured values fall within a narrow range. For smaller islands, the scatter is rapidly increasing and is much larger than the measurement-inaccuracy. The inset shows some typical IV -curves. The numbers in the inset correspond to the numbered data points in the main figure.

4.2.1 Room temperature measurements

Some typical room-temperature measurements are displayed in the inset of Fig. 4.1, showing weakly rectifying IV -curves. The overall shape of the curves is very similar. To investigate the dependence of the diode's conductances on their size, in Fig. 4.1 the zero-bias conductance per unit area is plotted as a function of island area for more than 40 different islands, grown on two similar n -type samples. One would expect that devices of equal size yield the same value for this quantity. Indeed, for larger devices the conductance per unit area falls within a narrow range. However, towards smaller areas there is no definite behavior. Instead, the scatter in the measured values increases rapidly and nominally equal devices yield very different results.

To study the increasing scatter in more detail, the standard deviation of the conductance per unit area is plotted in Fig. 4.2 as a function of diode area, calculated from the data of Fig. 4.1. We clearly observe that the standard deviation increases with decreasing island size.

Measurement inaccuracies are not the source of this random scatter, as proved by

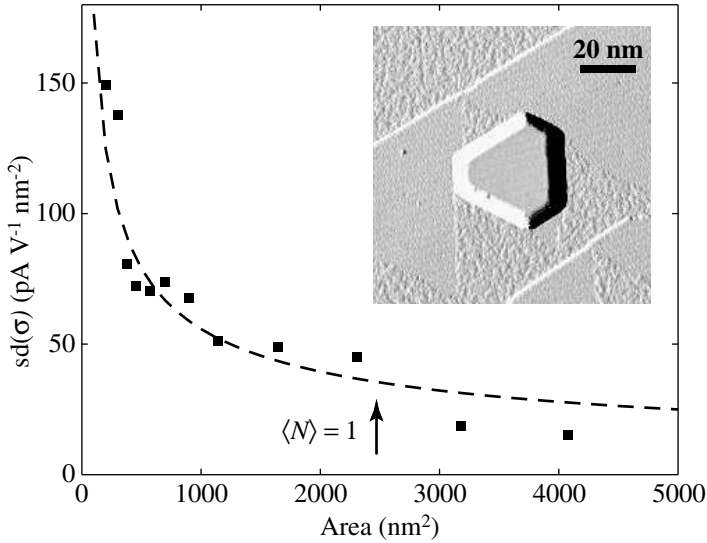


Figure 4.2 Standard deviations of the measured conductance per unit area for various values of the device area A . Each point is calculated from eight neighboring data points in Fig. 4.1. The dashed line is a least square fit of the function C/\sqrt{A} to these points, yielding $C = 1.8 \text{ nA V}^{-1} \text{ nm}^{-1}$. The arrow indicates which island size corresponds to an average of one dopant atom per island ($\langle N \rangle = 1$) according to our analysis. The inset shows an STM-image of a typical island, acquired at room-temperature directly after preparation.

the low noise level (typically less than 10 pA around zero bias) and good reproducibility of measurements on the same device. Moreover, this scatter is absent in similar measurements on low-doped samples (see Fig. 2.10). Schottky barrier inhomogeneities [8], which have been observed at non-epitaxial interfaces [9, 10, 11], do not play a role here, as they are due to variations in the atomic arrangement at the metal-semiconductor interface itself. The metal-semiconductor interfaces in our devices are perfectly epitaxial and mono-crystalline, which is supported by cross-sectional transmission electron micrographs of similar structures [12]. This also rules out interface defects or grain boundaries as the origin of the fluctuations. In addition, BEEM measurements of CoSi₂-films on undoped Si(111) reveal a perfectly homogeneous Schottky barrier height [10]. Only islands showing an atomically flat and defect-free surface in the STM-images were included in the analysis.

We will show that the increased scatter in the measured data is caused by the presence of randomly distributed dopant atoms in the Schottky barrier. An ionized dopant atom locally distorts the barrier, giving rise to a local barrier reduction and thus a high conductance spot (see the inset of Fig. 4.3). Then, the observed spread in Fig. 4.2 is directly related to the spread in the number of dopant atoms N in the barrier of a device. From

Poisson statistics, the relative spread is given by

$$\frac{\text{sd}(N)}{\langle N \rangle} = \frac{1}{\sqrt{\langle N \rangle}},$$

where $\text{sd}(N)$ is the standard deviation of N . Because $\langle N \rangle$ is proportional to the island area A , this gives that the standard deviation of the number of dopants per unit area increases when the device area decreases. Indeed, Fig. 4.2 shows that a function of the form C/\sqrt{A} describes our observations appropriately.

4.2.2 Low temperature measurements

To further investigate the influence of individual dopant atoms on the transport properties of small diodes, we performed similar experiments in a low-temperature UHV-STM operating at 4.5 K. In the upper part of Fig. 4.3, several IV -curves of two different islands are plotted. Each represents a full and independent measurement cycle (stop scanning, make contact, ramp V , release contact, resume scanning), demonstrating their reproducibility. The current is plotted on a logarithmic scale, to make the features of the curves visible over several orders of magnitude in current. Note that the noise-level is below 1 pA.

From the measured IV -curves, the quantity $(V/I) \cdot (dI/dV)$ (the so-called normalized differential conductance) has been calculated. It was calculated from the average of several IV -curves per island and plotted for the same two islands in the lower part of Fig. 4.3. This is a well-known approach in the field of scanning tunneling spectroscopy [13] and is very useful as it reduces the overall exponential behavior and enhances bias-dependent features. Indeed, the weak features in the IV -curves turn into clear peaks and the peaks show a one-to-one correspondence to the features in the IV -curves. The data presented in Fig. 4.3 was acquired from a p -type sample and it can be seen that the features appear at one bias polarity, only. This is true for all acquired curves on the same sample. For substrates with the opposite doping type (n -type), the peaks occur at the opposite bias polarity (not shown).

The peaks can be explained by resonant tunneling through a discrete energy level of a dopant atom, occurring when the Fermi-level at either side of the barrier lines up with an energy level of the dopant's potential well. The resulting resonant channel produces a feature in the measurement curve. Resonances are expected at bias voltages from zero up to the barrier height (roughly 0.5–0.7 V, depending on the dopant type; see also the inset in the lower part of Fig. 4.3). This is consistent with the observations. The actual bias voltage at which a resonance occurs is predominantly determined by the distance of the dopant atom to the interface. The number of peaks in a typical spectrum (one to four) corresponds to the expected number of dopants in the devices, as we will show later. This confirms our hypothesis that individual dopants influence the conduction path.

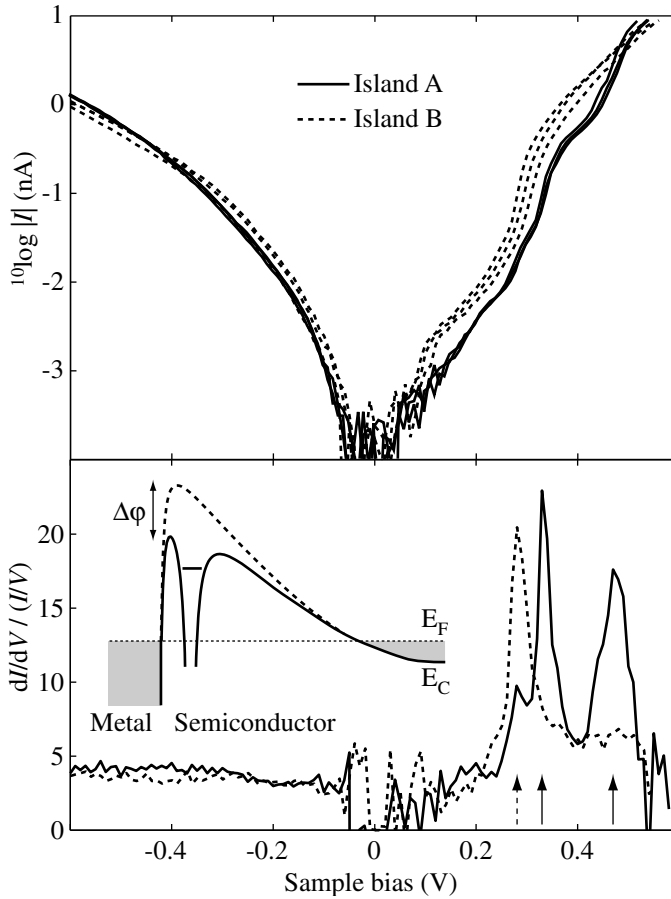


Figure 4.3 Measured IV -curves of two different CoSi_2 -islands on the same p -type sample. The upper graph shows three measurements of one island (island A, $A = 1300 \text{ nm}^2$) and also three measurements of another island (island B, $A = 1500 \text{ nm}^2$), demonstrating the reproducibility of the measurements. Features occurring at $|V| \lesssim 0.1 \text{ V}$ ($|I| \lesssim 1 \text{ pA}$) are due to noise. The lower panel shows the normalized differential conductance of the same two islands, calculated from an averaged IV -curve. Arrows indicate the main features in the IV -curves, showing up as peaks in the lower panel. The inset schematically shows the band diagram of an unbiased device. For clarity, the situation for an n -type sample is drawn. The dashed line is the initial conduction band (E_C) profile. The solid line is E_C perturbed by the dopant's Coulomb well, causing a local barrier lowering $\Delta\phi$.

4.3 Analysis

Motivated by the foregoing observations, we present a model that links the conductance fluctuations observed at room temperature to (random) dopant positions. Moreover, the parameters in the model are directly related to device parameters.

Because the dopants in the substrate are randomly distributed, the number of dopants N in the barrier of a given island is Poisson-distributed with parameter λ . This means that the probability $P_\lambda(k)$ that N equals k for a certain device is given by

$$P_\lambda(k) = \frac{\lambda^k}{k!} e^{-\lambda}, \quad (4.1)$$

where $\lambda = \langle N \rangle$ is the mean value of the number of dopants in the barrier of this particular device. The parameter can be expressed as $\lambda = AtN_d$, where A is the area of the island, t the effective thickness of the barrier and N_d the average doping concentration in the barrier. As shown in Fig. 4.2, the scatter in the number of dopants in the barrier per unit area satisfies $\text{sd}(N)/A \propto 1/\sqrt{A}$ and therefore is large for small islands.

We will now show that this effect also creates scatter in conductance measurements. We assume that dopants located in a certain region close to the metal-semiconductor interface induce a local barrier lowering that gives rise to a low-resistance transport channel*. The conductance of a transport channel induced by a dopant atom depends on the dopant's distance to the interface. Since the distance is a random variable, the conductance G_1 of a single channel is not the same for all channels, but has a certain probability distribution. The distribution is given by a probability density function $f_1(g)$, meaning that $f_1(g)dg$ is the probability for a certain channel to have a conductance G_1 between g and $g + dg$. Both the distribution of the position of a dopant in the barrier and the dependence of the conductance of a channel on that position are contained in $f_1(g)$.

Assuming that the values of the conductance of the individual channels are independent and characterized by the same distribution given by $f_1(g)$, the total conductance of a device is given by the sum of the contributions of the individual channels. Here, we neglect the background conduction and assume that the conductance is dominated by these channels. If there are k channels, the total conductance is $G_k = \sum_{i=1}^k G_1^{(i)}$, where the conductance of the individual channels is denoted by $G_1^{(i)}$. The density function $f_k(g)$ of G_k can be calculated explicitly[†] by taking the k -fold convolution of $f_1(g)$ [14]

$$f_k(g) = \underbrace{f_1(g) * \dots * f_1(g)}_{k \text{ times}}.$$

Finally, taking into account the Poisson distribution of the number of channels (Eq. 4.1), the density function $f(g, \lambda)$ of the total conductance G of a device can be computed as

$$f(g, \lambda) = \sum_{k=0}^{\infty} P_\lambda(k) f_k(g). \quad (4.2)$$

*Note that here the term 'channel' refers to a weak spot in a barrier and is unrelated to the conduction channels occurring in the field of quantum transport.

[†]In a numerical calculation, the $f_k(g)$ can be easily computed by using (fast) Fourier-transforms: $f_k = \mathcal{F}^{\text{inv}}([\mathcal{F}(f_1)]^k)$, where \mathcal{F} is the Fourier transform and \mathcal{F}^{inv} its inverse.

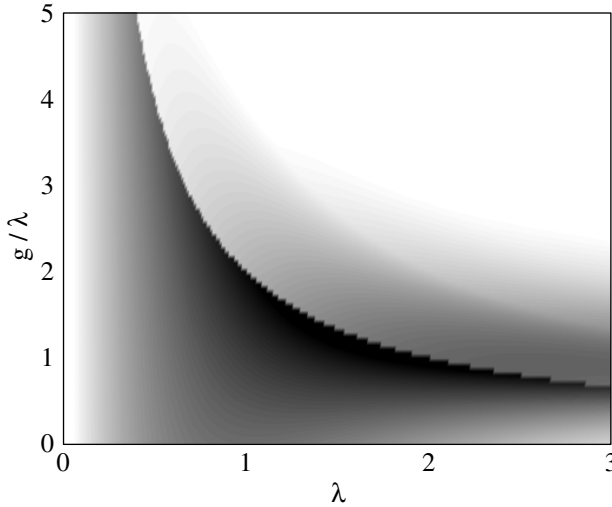


Figure 4.4 Map of $f(g, \lambda)$ as defined in Eq. (4.2) plotted as a function of g/λ (vertical axis) and λ (horizontal axis). The function values are represented in a linear gray-scale, where white corresponds to 0 and black to 0.65. For $f_1(g)$ a uniform distribution was chosen.

In other words, for given device parameters N_d , A and t , $f(g, \lambda)dg$ is the probability that the total conductance G due to dopant atoms in the diode is between g and $g + dg$.

To illustrate its behavior, Fig. 4.4 shows a map of $f(g, \lambda)$ (from Eq. 4.2) as a function of g/λ (proportional to the conductance per unit area) and λ (which is proportional to A). For a fixed value of the device area (that is a fixed value of λ and a vertical line in the plot) the color scale gives the probability density to find a device with a particular conductance per unit area g/λ . For large values of λ , all density is concentrated around $g/\lambda = \frac{1}{2}$, while for smaller λ it is spread over an increasingly wide range of values. In this figure $f_1(g)$ was chosen as a uniform distribution. However, as we will show next, the general properties of $f(g, \lambda)$ are not strongly dependent on the particular choice of $f_1(g)$.

Without making any assumptions on the choice of $f_1(g)$, we can compute the moments of $f(g, \lambda)$ in terms of those of $f_1(g)$. First, the mean value of G satisfies

$$\begin{aligned} \langle G \rangle &= \int g f(g, \lambda) dg = \sum_{k=0}^{\infty} P_{\lambda}(k) \int g f_k(g) dg = \\ &= \sum_{k=0}^{\infty} P_{\lambda}(k) \cdot k \langle G_1 \rangle = \lambda \langle G_1 \rangle. \end{aligned}$$

In fact, to allow for easy comparison with the data, we consider the total conductance per unit area σ . By making the substitution $\sigma = G/A$. It follows directly that the average value of σ satisfies

$$\langle \sigma \rangle = t N_d \langle G_1 \rangle. \tag{4.3}$$

This is a very intuitive result, since $\langle\sigma\rangle$ equals the average number of dopants in the barrier per unit area multiplied by the average conductance per channel.

To obtain the standard deviation we first observe that

$$\begin{aligned}\langle G_k^2 \rangle &= \langle (G_1^{(1)} + \dots + G_1^{(k)})^2 \rangle = \\ &= k\langle G_1^2 \rangle + k(k-1)\langle G_1 \rangle^2,\end{aligned}$$

when the $G_1^{(i)}$ are independently identically distributed. Using this fact, we find that

$$\begin{aligned}\langle G^2 \rangle &= \int g^2 f(g, \lambda) dg = \sum_{k=0}^{\infty} P_{\lambda}(k) \int g^2 f_k(g) dg = \\ &= \sum_{k=0}^{\infty} P_{\lambda}(k) \cdot (k\langle G_1^2 \rangle + k(k-1)\langle G_1 \rangle^2) = \\ &= \lambda\langle G_1^2 \rangle + \lambda^2\langle G_1 \rangle^2.\end{aligned}$$

Finally, this yields

$$\text{sd}(G) = \sqrt{\langle G^2 \rangle - \langle G \rangle^2} = \sqrt{\lambda\langle G_1^2 \rangle}.$$

By making the substitution $\sigma = G/A$ once more, we find that the standard deviation $\text{sd}(\sigma)$ (which can be interpreted as the spread in σ) is given by

$$\text{sd}(\sigma) = \sqrt{\frac{tN_d}{A}\langle G_1^2 \rangle}. \quad (4.4)$$

The most important observation from this equation is that $\text{sd}(\sigma)$ is proportional to $1/\sqrt{A}$, showing that the area-dependence of $\text{sd}(N)/A$ leads to a similar behavior of spread in σ . This also justifies the choice of the fit-function in Fig. 4.2.

4.4 Application to the data

Our simple model captures the general features of the data and yields reasonable values for the parameters. To demonstrate this, a least square fit of the function C/\sqrt{A} (cf. Eq. (4.4); C is a fit-parameter) to the standard deviations has been performed. The result is the dashed line in Fig. 4.2. The fit gives a good description of the data, showing that the spread in the data is consistent with the prediction of the model.

From the fit, we make some estimates for the physical quantities in the model. The value of the fit-parameter $C = 1.8 \text{ nA V}^{-1} \text{ nm}^{-1}$ should be equal to $\sqrt{tN_d\langle G_1^2 \rangle}$ (according to Eq. (4.4)). By looking at the large area values in Fig. 4.1, we find that $tN_d\langle G_1 \rangle \approx 0.04 \text{ nA V}^{-1} \text{ nm}^{-2}$ (Eq. (4.3)). Combining these numbers and assuming that $\langle G_1 \rangle^2 \approx \langle G_1^2 \rangle$ we find values for parameters in the model. First, $1/tN_d \approx 1/(2500 \text{ nm}^2)$, which corresponds to an average of one dopant per 2500 nm^2 device area (indicated in Fig. 4.2).

This number is consistent with e.g. an average doping concentration at the interface* around $N_d = 10^{17} \text{ cm}^{-3}$ and an effective barrier thickness $t = 2.5 \text{ nm}$. Note that because t is the thickness of the barrier region where dopants influence the barrier height, it is thinner than the total Schottky barrier thickness (a few tens of nanometers in this case). Second, we find $\langle G_1 \rangle \approx 100 \text{ nA/V}$ for the average conductance per channel. In order to achieve this value, it is necessary to have e.g. a small patch with a local barrier height of approximately 0.15 eV and an area† of approximately 10 nm^2 . These numbers are consistent with the actual sample parameters.

On average, the conductance per unit area increases for decreasing island area, as can be seen from Fig. 4.1. This can be explained by the scaling mechanism described in Ref. 15, which predicts that the barrier thickness decreases with device size for devices that are smaller than a few times the Debye length. We note that the increasing value of $\langle \sigma \rangle$ is not the cause of the increment of $\text{sd}(\sigma)$, since similar measurements on low-doped samples do not exhibit an increased scatter (see Fig. 2.10).

As demonstrated by our measurements, the discreteness of doping is easily observed in highly doped samples. In lower doped samples, where the barrier is thicker, the effect is expected to be much weaker. The local distortion of the potential landscape due to the presence of a dopant is roughly as large as its effective Bohr-radius, which equals about 3 nm in silicon. When the barrier thickness is much larger than the dopant's potential well, the effective barrier lowering will be negligible. Hence the induced local barrier lowering is the most pronounced in thin barriers.

4.5 Conclusions

In conclusion, we have shown that individual dopant atoms dominate the transport characteristics of epitaxial nanometer sized metal semiconductor diodes. Room temperature data show increasingly large device-to-device conductance fluctuations towards smaller device sizes. Measurements at 4.5 K reveal pronounced structure in the IV -curves. A statistical analysis based on the assumption of randomly positioned individual dopant atoms leads to a good description of the experimental data.

- [1] T. Tanaka, T. Usuki, T. Futatsugi, Y. Momiyama, and T. Sugii, IEDM Tech. Dig. pp. 271–274 (2000).
- [2] J. D. Meindl, Q. Chen, and J. A. Davis, *Science* **293**, 2044 (2001).
- [3] B. Hoeneisen and C. A. Mead, *Solid-State Electron.* **15**, 819 (1972).
- [4] P. M. Voyles, D. A. Muller, J. L. Grazul, P. H. Citrin, and H.-J. L. Grossmann, *Nature* **416**, 826 (2002).

*The doping concentration close to the silicon surface can be much lower than in the bulk due to out-diffusion during the sample preparation, as confirmed by simulations and SIMS-measurements. We want to thank M. J. P. Hopstaken and G. C. J. Maas at Philips CFT - Materials Analysis for performing the SIMS-measurements.

†This estimate was made using the thermionic emission model [S. M. Sze, *Physics of Semiconductor Devices* (Wiley, New York, 1981), 2nd ed.].

- [5] S. Modesti, D. Furlanetto, M. Piccin, S. Rubini, and A. Franciosi, *Appl. Phys. Lett.* **82**, 1932 (2003).
- [6] W. D. Rau, P. Schwander, F. H. Baumann, W. Höppner, and A. Ourmazd, *Phys. Rev. Lett.* **82**, 2614 (1999).
- [7] N. Sano and M. Tomizawa, *Appl. Phys. Lett.* **79**, 2267 (2001).
- [8] R. T. Tung, *Phys. Rev. B* **45**, 13509 (1992).
- [9] A. A. Talin, R. S. Williams, B. A. Morgan, K. M. Ring, and K. L. Kavanagh, *Phys. Rev. B* **49**, 16474 (1994).
- [10] T. Meyer and H. von Känel, *Phys. Rev. Lett.* **78**, 3133 (1997).
- [11] N. D. Jäger, K. Urban, E. R. Weber, and P. Ebert, *Appl. Phys. Lett.* **82**, 2700 (2003).
- [12] P. A. Bennett, D. J. Smith, and I. K. Robinson, *Appl. Surf. Sci.* **180**, 65 (2001).
- [13] J. A. Stroschio, R. M. Feenstra, and A. P. Fein, *Phys. Rev. Lett.* **57**, 2579 (1986).
- [14] G. R. Grimmett and D. R. Stirzaker, *Probability and random processes* (Clarendon, Oxford, 1992), 2nd ed.
- [15] G. D. J. Smit, S. Rogge, and T. M. Klapwijk, *Appl. Phys. Lett.* **81**, 3852 (2002).



Spectroscopy of individual dopant atoms

Abstract — To provide the context for the subsequent chapters, we present first experiments done in our group, which eventually should lead to resonant tunneling spectroscopy of single dopant atoms. Measuring large silicon tunneling devices containing a δ -doped barrier, we observe a resonance in the differential conductance. It is identified as arising from tunneling through the B^+ state of boron atoms in the δ -layer. Furthermore, we show a fabrication method for nano-devices approaching the size regime necessary for the observation of single dopant atoms. The feasibility of an STM-based measurement method is demonstrated.*

5.1 Introduction

In the subsequent chapters of this thesis, we will present calculations of the behavior of individual dopant atoms in electric and magnetic fields, which were performed in conjunction with the experimental work that is carried out in our group. The purpose of this chapter is to provide some context and background for those calculations, by presenting our recent experimental progress.

In Chapter 4, we have shown experimental results demonstrating the occurrence of resonant tunneling through individual dopant atoms. However, the usage of resonant tunneling spectroscopy (RTS) as a tool to study dopant atoms requires a more controlled experimental system, such as the silicon tunnel barriers that will be presented here.

*The measurement and fabrication of the large devices was carried out by I.D. Vink and J. Caro [see J. Caro, I.D. Vink, G.D.J. Smit, S. Rogge, T.M. Klapwijk, R. Loo, and M. Caymax, *cond-mat/0309139* (2003), submitted to *Phys. Rev. B*]. Measurements of the nano-devices were done together with H. Sellier, who also did the fabrication.

Resonant tunneling spectroscopy (RTS) is a generally applicable and efficient tool to investigate the energy levels of confined systems (see Chapter 1). Modern lithographic techniques enable the preparation of structures in a semiconductor which are sufficiently small to allow for singling out one dopant atom. This gives the opportunity to use RTS as an instrument to study the energy levels of individual dopant atoms. In fact, energy levels of dopant atoms have been observed before in a GaAs barrier containing many dopants [1], single impurities inside a GaAs quantum well [2, 3] and single impurities inside a Si Schottky barrier (see Chapter 4 and Ref. 4).

In the past, large ensembles of dopants have been successfully studied using optical methods (photo-excitation) [5]. Using such methods to address or detect the response of a *single* dopant atom is, however, not as straightforward as with RTS. Another advantage of RTS over optical methods is that all levels are accessible, because there are no restrictions due to optical selection rules. Furthermore, the ground state energy and its behavior in a field can be measured independently. A point of concern is the large electric field that is inherent to this method. Its influence on the energy level positions and width will be discussed in detail in Chapter 7.

In this chapter, we report on the first experiments, which are a part of our effort to study individual dopant atoms using RTS and which eventually should lead to the observation of and control over the energy levels of a single dopant atom. In our initial experiments, we observe a resonance in transport experiments of a silicon tunnel barrier containing a δ -doping layer. Based on its energy position and magnetic field behavior, it is ascribed to resonant tunneling through boron centers in the δ -layer, which are binding two holes. Furthermore, we demonstrate the implementation of a fabrication scheme and an STM-based measurement method that should make the observation of resonant tunneling through a *single* impurity possible. Finally, we discuss potential problems and limitations of our approach.

5.2 Experiments in large devices

At low temperatures, silicon can be an insulator or a conductor, depending on the doping level. This allows for the fabrication of tunneling devices in which both the barrier (in which the single impurity is located) and the emitter/collector are made from silicon, such that the complete device is mono-crystalline. In this way, undesired electrically active defects at the interfaces are avoided.

We fabricated all-silicon δ -doped tunneling devices from a layered structure consisting of 40 nm lowly doped Si (p^- , acting as a barrier) sandwiched between two 500 nm thick degenerately doped p^+ Si layers (acting as metallic contacts). Boron is the dopant in all layers. A δ -spike of boron atoms with areal density $1.7 \times 10^{11} \text{ cm}^{-2}$ is centered in the lowly doped tunnel barrier. The structure is deposited by chemical vapor deposition (CVD) on a Si(001) substrate with low doping. The doping profile in the structure was measured with secondary ion mass spectroscopy (SIMS). The growth and doping profile measurements were performed at IMEC (Leuven, Belgium)*.

*The layer package was grown by R. Loo and M. Caymax (IMEC, Leuven, Belgium)

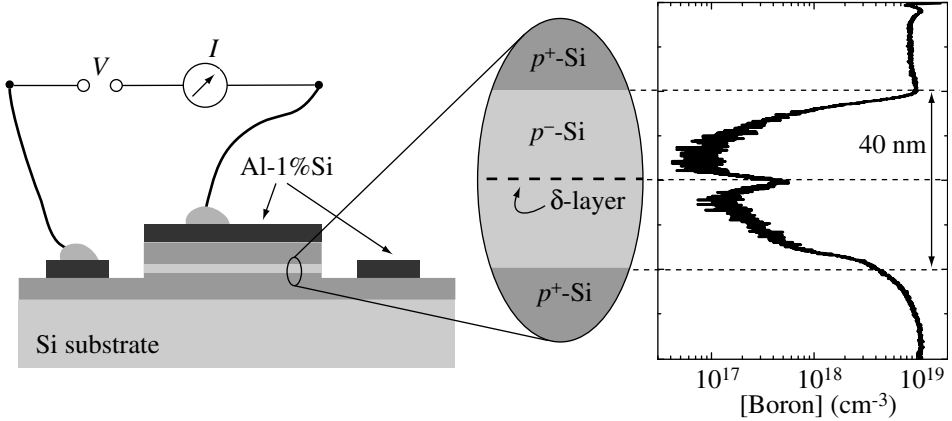


Figure 5.1 Schematic overview of the layered structure after fabrication and bonding. The right graph shows measured SIMS data of the structure.

The right part of Fig. 5.1 shows the result of the SIMS measurements, in which the δ -layer, the barrier and the contact layers can be clearly distinguished. The p^+ layers are degenerately doped, with boron concentration $N_B = 10^{19} \text{ cm}^{-3}$. The δ -layer is about 3 nm wide (full width at half maximum) and has a peak concentration of $N_B = 5 \times 10^{17} \text{ cm}^{-3}$. The contrast of the δ -layer and the unintentionally high background doping ($N_B \approx 10^{17} \text{ cm}^{-3}$) in the barrier is somewhat weak. This is due to boron diffusion out of the bottom contact layer and the δ -layer, occurring during the Si-growth.

In order to characterize the material, we first fabricate square mesas, 100, 200, 300 and 400 μm at a side. The δ -layer in each of these devices contains millions of dopants. The mesas are fabricated by sputter-depositing squares of Al-1%Si through a micro-fabricated shadow mask. These squares serve both as a top contact and as an etching mask for the reactive ion etch in an SF_6 plasma that is used to create the mesas. The SF_6 etch is stopped just after the bottom p^+ layer has been reached. A second shadow mask, aligned with respect to the mesas, is used for sputter deposition of Al-1%Si contacts to the bottom layer. The final step is a 400 $^\circ\text{C}$ anneal in N_2/H_2 -atmosphere, using rapid thermal processing, to improve the contact of the Al to the p^+ Si. The total structure is schematically depicted in Fig. 5.1. At low temperature, the device resistance is dominated by the barrier in the mesa.

Electrical measurements were performed in a ^4He flow cryostat equipped with a 14 T superconducting magnet and in a ^3He cryostat. Standard lock-in techniques were used to measure the differential conductance G versus bias voltage V . At 4.2 K and below a single peak is present in these GV -curves around 10 mV, superimposed on a dominant background (see Fig. 5.2). This peak becomes higher and narrower for decreasing temperatures and is not yet saturated at 0.5 K, where the FWHM of the peak is about 1.5 mV. The peak is absent for devices that have no δ -layer but are otherwise identical. This indicates that the peak originates from the boron atoms of the δ -layer.

Figure 5.3 shows a schematic overview of the valence band profile across the device.

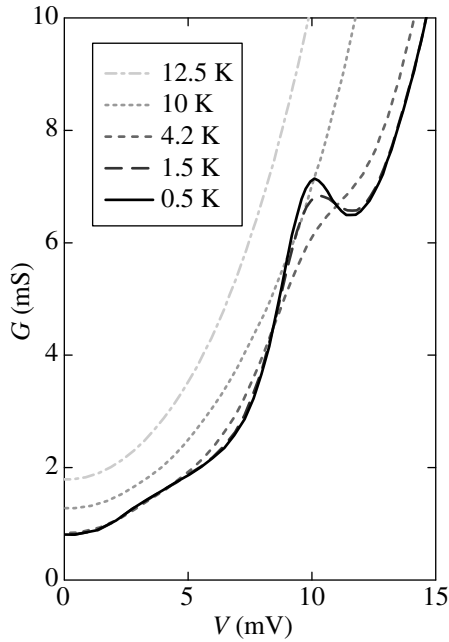


Figure 5.2 *GV*-curve at positive bias voltage for various temperatures (the full curve is symmetric around zero bias). The peak can clearly be seen to develop for decreasing temperature. (Data courtesy of I.D. Vink)

The barrier is formed due to bandgap narrowing in the degenerately doped contacts. Band bending in the barrier can be neglected as it occurs on much longer length scales than the width of the barrier. In the highly doped contacts, an impurity band is formed and the Fermi level position within the band is determined by the doping concentration. The barrier height is determined experimentally to be 11.7 meV, by measuring the temperature dependence of the zero-bias conductivity, which shows activated behavior.

When the structure of Fig. 5.3 is biased, a current starts flowing due to direct tunneling through the barrier. An ionized dopant located inside the barrier introduces a potential well, effectively creating a double barrier system. When the Fermi-level at one side of the barrier aligns with an energy level of the potential well, a resonant channel is opened, resulting in a feature in the *IV*-characteristic. In our device, the boron ground state is located far below the Fermi-level and is therefore occupied by a hole. The resulting neutral boron impurity is able to weakly bind a second hole, resulting in the charged B^+ -state.

We attribute the observed peak in Fig. 5.2 to resonant tunneling through B^+ -states in the δ -layer. The resonance is observed at a bias voltage of just below 10 meV. Using the barrier height obtained before, the binding energy of the B^+ state is found to be slightly more than 6.7 meV. In literature, the B^+ binding energy is found to increase with the

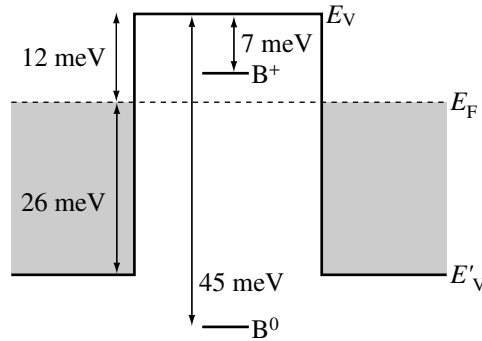


Figure 5.3 Schematic drawing of the valence band edge profile at zero bias. The hole energy increases towards the top of the image. Due to the low temperature and the narrow barrier (~ 40 nm) band bending in the central region can be neglected. E'_V is the new valence band edge that is formed in the highly doped contacts. The Fermi-level position in the contacts is determined by the doping concentration. The ground state of the dopant atoms in the barrier is far below E_F , so at low temperature they are always occupied. Therefore, only the B^+ -state is available for tunneling.

doping concentration. The value we observe is in agreement with extrapolated data from literature (for details, see Ref 6).

Measurements of the resonance in a magnetic field reveal a shift of the resonance position towards higher bias (weaker binding) as well as a broadening of the peak (Fig. 5.4). A rough estimate shows that the size of the shift is consistent with the expected shift from diamagnetism of the B^+ -state [6]. We will analyze these results in more detail in Chapter 6.

5.3 Experiments in nano-devices

The areal density of the δ -layer ($1.7 \times 10^{11} \text{ cm}^{-2}$) gives rise to an average inter-dopant distance of about 25 nm. In order to enter the regime where only a small number of dopant atoms (down to one) is present in the δ -layer of a device, device diameters of 100 nm and below are required. An alternative approach—decreasing the areal density of the layer—would allow for larger devices, but then the number of dopants due to background doping and the background conduction would be relatively too high. Indeed, a reduction of the areal density of the δ -doping layer by a factor 5-10 would make the peak in Fig. 5.1 disappear into the background.

For the fabrication of the sub-100 nm devices, we start from a similar layer package as in the previous section, the only difference being that the thickness of the upper p^+ layer is reduced to 20 nm. The thin top layer prevents the occurrence of an unnecessary high aspect ratio of the mesas. Spots on a double layer resist (PMMA) of down to 50 nm in diameter are exposed by an electron beam. After development and an HF-dip to remove the native oxide of the exposed silicon, a 20 nm thick platinum layer is evaporated onto

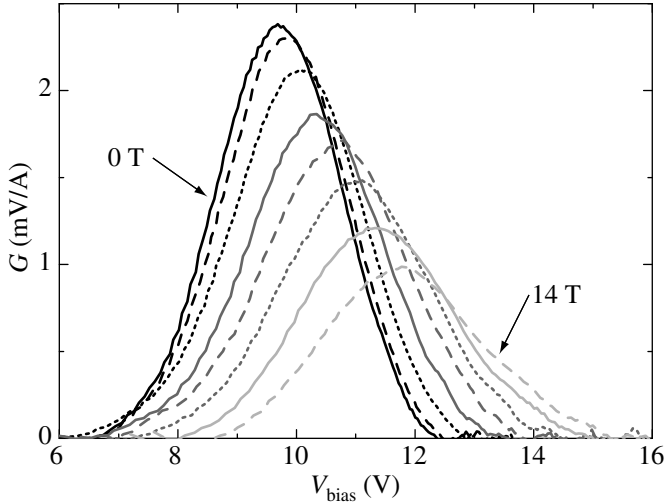


Figure 5.4 The resonance peak in the GI -curves after subtraction of a local linear background for various magnetic fields (from 0 to 14 T in steps of 2 T). The peak obviously shifts, broadens and decreases in height. (Data courtesy of I.D. Vink)

the surface. Lift-off yields arrays of small circular platinum patches. The platinum serves both as a noble-metal contact and as an etching mask for the subsequent anisotropic reactive ion etch, which is carried out in a $\text{BCl}_3/\text{Cl}_2/\text{N}_2$ -plasma. Again, this etch is stopped just after the bottom p^+ -layer has been reached, yielding ~ 80 nm high silicon mesas [see Fig. 5.5(a)]. These mesas are still covered by ~ 10 nm platinum that remains after the etch.

For first experiments on these devices, it is advantageous to avoid the complicated fabrication steps that are required to connect the top layer of the nanometer-sized mesas to bonding pads. Therefore, we fabricate a large and dense array of the mesas described above (typically ~ 10 mesas per μm^2), so that we can use the tip of a scanning tunneling microscope (STM) to locate and contact individual mesas.

An STM-image of a typical mesa is shown in Fig. 5.5(b). Note that imaging these structures with an STM is not straightforward due to the large height differences and steep walls. Measurements were carried out by locating a mesa with the STM, contacting the platinum patches on top of the mesa with the STM-tip (see Fig. 5.6), and acquiring an IV -curve, similar to the technique used in Chapter 2 and 4. Because of the required energy resolution, the electrical measurements were carried out in a commercial STM operating at 4.5 K. The drift of the STM-tip with respect to the sample was so small at low temperatures that maintaining a stable electrical contact for several tens of minutes was possible. This enables accurate measurements, including the use of lock-in techniques.

Although we successfully acquired IV -curves on individual mesas, we have not been able yet to produce measurements that are worth comparing to the results in the previous section. The reason for this is that the experiments were hampered by a high contact

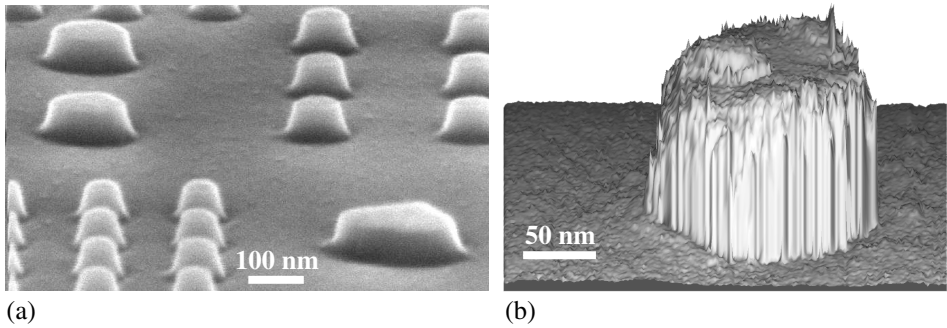


Figure 5.5 (a) Scanning electron micrograph showing micro-fabricated mesas of various diameters. (b) Scanning tunneling micrograph (in 3-dimensional representation) of a mesa. The height of this mesa is about 80 nm. (Images courtesy of H. Sellier)

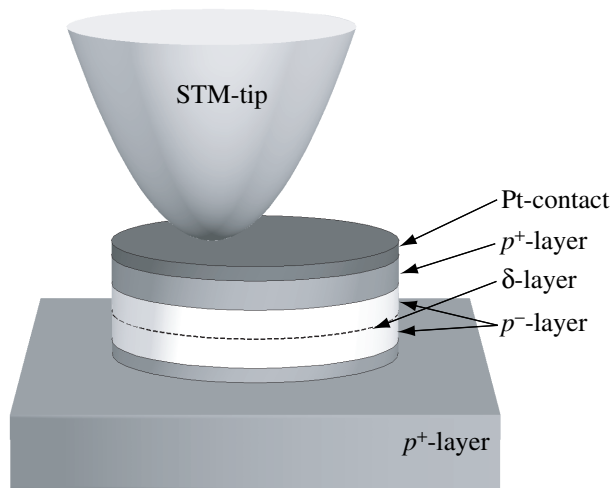


Figure 5.6 Schematic of the device layout during measurement. The top contact Pt-layer is contacted by an STM tip. By applying a bias voltage to the tip, IV -measurements are carried out.

resistance between the platinum and the upper silicon layer. Work on a solution to this problem is currently in progress.

5.4 Discussion

A limitation of the current layer package is the high background concentration in the Si barrier. Ideally, this layer would be undoped, but the high processing temperatures during CVD growth (600-700 °C) give rise to substantial diffusion of boron from the contact layers and δ -layer into the barrier. This effect is clearly visible in Fig. 5.1. There are several possible solutions to this problem. First, one could switch to another combination of host material and impurities, where the diffusion constant of the dopant atoms is smaller. Second, one could use molecular beam epitaxy instead of CVD. Because of the lower growth temperature, a much sharper doping profile can be achieved [7].

The STM-based measurement technique (combined with lithographically fabricated devices) presented in this chapter has several advantages over the traditional approach. First, the fabrication is relatively simple, because the top of the mesas are not connected to bonding pads. Second, a much larger number of devices can be prepared on a single chip, making it possible to gather statistical information from measurements of many identically prepared devices.

On the other hand, our measurements of large devices show that experiments at temperatures below 4.2 K and in a magnetic field are inevitable in order to have sufficient energy resolution and for identification of the observed peaks. However, operating an STM at temperatures below 4.2 K and in a large magnetic field is highly non-trivial and at the edge of current technological possibilities. Carrying out the desired measurements is more straightforward for traditionally fabricated devices. Moreover, once a complete device has been successfully fabricated, it is much more stable than an STM-contacted device and integration of e.g. a gate is more difficult in the STM-approach. Note that the fabrication of a low-resistance metal-semiconductor contact on the nanometer scale is generally a challenging task, which is required for both approaches. We conclude that the STM-approach is especially suited for initial experiments, while the fully lithographically contacted devices are preferred in a later stage, when more accurate and sensitive experiments are required.

Obviously, the wall of a mesa plays a much more important role in the nano-devices than in the large devices. This wall is bound to incorporate electrically active defects due to contamination, etch damage and oxidation in ambient. A large amount of surface defects at the walls could give rise to Fermi level pinning, leading to a lateral confinement potential and limiting electrical transport to the center region of the mesa. Such a (partial) pinch-off effect would substantially relax the size requirements for the observation of a single dopant atom.

5.5 Conclusion

Successful measurements of large devices, containing many resonant channels via a dopant atom in parallel, demonstrate the feasibility of our approach to use resonant tunneling as a probe for the energy levels of (individual) dopants. We implemented an STM-based measurement method, which enables a simplified fabrication scheme of structures containing ~ 1 dopant atom. Therefore, once the contact problems between the mesa and platinum patch are solved, it will prove to be very useful for quick evaluation of the material and physical principles.

- [1] I. P. Roche, G. P. Whittington, P. C. Main, L. Eaves, F. W. Sheard, G. Wunner, and K. E. Singer, *J. Phys.: Condens. Matter* **2**, 4439 (1990).
- [2] M. W. Dellow, P. H. Beton, C. J. G. M. Langerak, T. J. Foster, P. C. Main, L. Eaves, M. Henini, S. P. Beaumont, and C. D. W. Wilkinson, *Phys. Rev. Lett.* **68**, 1754 (1992).
- [3] M. R. Desphande, J. W. Sleight, M. A. Reed, R. G. Wheeler, and R. J. Matyi, *Phys. Rev. Lett.* **76**, 1328 (1996).
- [4] L. E. Calvet, R. G. Wheeler, and M. A. Reed, *Appl. Phys. Lett.* **80**, 1761 (2002).
- [5] A. Ramdas and S. Rodriguez, *Rep. Prog. Phys.* **44**, 1297 (1981).
- [6] J. Caro, I. D. Vink, G. D. J. Smit, S. Rogge, T. M. Klapwijk, R. Loo, and M. Caymax (2003), cond-mat/0309139.
- [7] B. E. Weir, R. L. Haedrick, Q. Shen, L. C. Feldman, M. S. Hybertsen, M. Needels, M. Schlüter, and T. R. Hart, *Phys. Rev. B* **46**, 12861 (1992).



Group theoretical analysis of double acceptors in a magnetic field: identification of the Si:B^+ ground state

Abstract — A boron impurity in silicon binding an extra hole is known to have only one bound state at an energy of just below 2 meV. The nature of the Si:B^+ ground state is however not well established. We qualitatively analyze the behavior in a magnetic field of isolated acceptors in a tetrahedral lattice binding two holes using group theory. Applying these results, we analyze measurements presented in Chapter 5 and conclude that the ground state of B^+ is most compatible with a non-degenerate Γ_1 state.*

6.1 Introduction

A neutral boron acceptor in silicon is able to weakly bind an extra hole, resulting in a positively charged ion (B^+). This entity is an example of a positively charged acceptor, commonly denoted by A^+ , which is the counter part of the better known negatively charged donor D^- . Both are related to their atomic-physics analogue, the negative hydrogen ion H^- . The energy states associated with these ions are very shallow and spatially

*This chapter is based on the following paper: G. D. J. Smit, S. Rogge, J. Caro, and T. M. Klapwijk, cond-mat/0309136 (2003), to be published in Phys. Rev. B.

large. When their concentration is sufficiently high, their overlapping wave functions can form an upper Hubbard band [1] and they play an important role in electronic transport in semiconductors at low temperatures. Since a few years, electronic states of individual dopant atoms gained renewed interest due to their prospective application in Si-based solid state quantum computing [2].

Neither theoretically nor experimentally much work has been done on the B^+ -state. Optical spectroscopy is difficult due to the small ionization energy (less than 2 meV [3]). In particular, the nature of its ground state is not well-established and to our knowledge no results have been published on the magnetic field dependence of the energy levels.

The purpose of this chapter is twofold. First, we present a general group-theoretical study of the magnetic field dependence of two-hole states in tetrahedral semiconductors. To our knowledge, such an analysis has not been published before. Second, because our analysis includes all possibilities for the B^+ ground state, it enables us to compare our results with our measurements of B^+ in a magnetic field (Chapter 5; Ref. 4) and to draw conclusions about the nature of the B^+ ground state.

6.2 Background

The nature of the energy levels of a *neutral* boron acceptor (B^0) in silicon is well-known [5] and the Zeeman effect in B^0 has been studied in detail, both theoretically [6] and experimentally [7]. The B-impurity is located at substitutional sites of the tetrahedral silicon lattice. The (one-hole) ground-state is a $1s$ -like fourfold degenerate state that belongs to the Γ_8 representation of the tetrahedral double group \bar{T}_d (for the nomenclature of representations used, see Table A.1 in Appendix A). The bound hole has total angular momentum $j = \frac{3}{2}$. The single-hole wave function is the product of a $1s$ hydrogen-like envelope function and a band-like function. Due to spin-orbit interaction in silicon, the $j = \frac{1}{2}$ valence band is split off by ~ 43 meV [5] and does not need to be considered in first order. A magnetic field completely lifts the fourfold degeneracy and the lowest order Zeeman effect of the Γ_8 state is linear.

As far as symmetry is concerned, the B^+ -state is similar to neutral group-II acceptors in a tetrahedral lattice, which are well-studied (e.g. Ref. 8 and references therein). Coupling two $j = \frac{3}{2}$ (Γ_8) holes bound to a single nucleus gives rise to a six-fold degenerate state, because due to the Pauli-principle only the *anti*-symmetric part of $\Gamma_8 \times \Gamma_8$ must be taken into account. This can be reduced to its components as $\{\Gamma_8 \times \Gamma_8\} = \Gamma_1 + \Gamma_3 + \Gamma_5$. Interaction between the two holes can split the state into a non-degenerate Γ_1 state with total angular momentum $J = 0$ and a fivefold $\Gamma_3 + \Gamma_5$ state carrying $J = 2$.

Detailed quantitative calculations, which are necessary to establish the ordering and splitting of these levels, are very difficult to carry out, because of the many complicated physical effects that must be taken into account (valence band structure, crystal field, Jahn-Teller-effect, etc.). Hund's rule, well-known from atomic physics, predicts that the more symmetric Γ_1 state has a higher energy than the $\Gamma_3 + \Gamma_5$ state, such that the latter is the ground state. The same conclusion was drawn from numerical calculations based on effective mass theory [9]. However, it has been shown that a dynamic Jahn-Teller effect

Table 6.1 Overview of possible two-hole states arising from products of two single hole states and their reduction to irreducible representations of \tilde{T}_d . For states originating from two *equivalent* single hole states (first two lines in the table), the Pauli principle allows only the antisymmetric part to be considered.

Combination	Two-hole states
$\{\Gamma_8 \times \Gamma_8\}$	$\Gamma_1 + \Gamma_3 + \Gamma_5$
$\{\Gamma_6 \times \Gamma_6\} = \{\Gamma_7 \times \Gamma_7\}$	Γ_1
$\Gamma_8 \times \Gamma'_8$	$\Gamma_1 + \Gamma_2 + \Gamma_3 + 2\Gamma_4 + 2\Gamma_5$
$\Gamma_6 \times \Gamma'_6 = \Gamma_7 \times \Gamma'_7$	$\Gamma_1 + \Gamma_4$
$\Gamma_8 \times \Gamma_7 = \Gamma_8 \times \Gamma_6$	$\Gamma_3 + \Gamma_4 + \Gamma_5$
$\Gamma_7 \times \Gamma_6$	$\Gamma_2 + \Gamma_5$

can provide a mechanism to reverse the ordering of the levels [10, 11], leading to a Γ_1 ground state. This has in fact been observed in several neutral double acceptors.

Very little experimental work on B^+ has been done. The binding energy of the second hole in an isolated B^+ -state has been measured in phonon-induced conductivity (PIC) measurements [3] and photoconductivity experiments [12]. It is slightly below 2 meV. Stress-dependence has been investigated with the same techniques [12, 13] and in one case the results were explained as evidence for a stress-induced ground state splitting [13]. However, interpretation of the conductivity data is non-trivial, because only levels which are very close to either the ground state of B^+ or the valence band edge can be observed with these techniques. Similar experiments in a magnetic field [14] showed a linear increase of the binding energy, which was ascribed to Landau level formation in the valence band. In these experiments, no additional shift or splitting was resolved.

Recent transport experiments in Si resonant tunneling devices provide a way to directly observe the magnetic field dependence of the B^+ state [4]. These experiments showed a super linear shift of the ground state towards the valence band (Fig. 6.2). Neither a ground state level-splitting nor bound excited states were observed.

6.3 Double acceptors in a magnetic field

Here, we present a group theoretical study to qualitatively analyze the magnetic field behavior of isolated acceptors binding two holes in a tetrahedral semiconductor for various possible states. This analysis is not only applicable to neutral group-II acceptors (e.g. Zn in Ge), but also to group-III acceptors binding an extra hole and singly ionized group-I acceptors (e.g. Cu^- in Ge). After this general part, we return to the specific situation of B^+ .

We subsequently consider various possible two-hole levels and analyze their behavior in a magnetic field using perturbation theory. All such levels transform according to single-valued representations of T_d , as shown in the overview in Table 6.1. We assume that the Coulomb force and spin-orbit interaction between the holes is sufficiently strong to split the levels into their irreducible components. Because of its possible importance

Table 6.2 Reduction of the representations of T_d when a magnetic field is applied along a $\langle 100 \rangle$, $\langle 111 \rangle$, or $\langle 110 \rangle$ direction of the tetrahedral lattice. From this table it can be deduced how the double acceptor levels split in a magnetic field.

Direction	$\langle 100 \rangle$	$\langle 111 \rangle$	$\langle 110 \rangle$
Group	S_4	C_3	C_{1h}
$\Gamma_1 (T_d)$	Γ_1	Γ_1	Γ_1
$\Gamma_2 (T_d)$	Γ_2	Γ_1	Γ_2
$\Gamma_3 (T_d)$	$\Gamma_1 + \Gamma_2$	$\Gamma_2 + \Gamma_3$	$\Gamma_1 + \Gamma_2$
$\Gamma_4 (T_d)$	$\Gamma_1 + \Gamma_3 + \Gamma_4$	$\Gamma_1 + \Gamma_2 + \Gamma_3$	$\Gamma_1 + 2\Gamma_2$
$\Gamma_5 (T_d)$	$\Gamma_2 + \Gamma_3 + \Gamma_4$	$\Gamma_1 + \Gamma_2 + \Gamma_3$	$2\Gamma_1 + \Gamma_2$

for B^+ , we also consider the $\Gamma_3 + \Gamma_5$ level. In all cases it is assumed that the level under consideration is well separated from neighboring levels.

Furthermore, we briefly address the analogue of the central field approximation in atomic physics, where it is assumed that each of the two holes moves in the field of the negative ionized acceptor core and the averaged effective potential due to the other hole. In this approximation, the symmetry of the field in which each hole moves is unaffected by the presence of the second hole. This method is known to give a good description for some group-II acceptors in Si and Ge [8].

When a magnetic field \mathcal{B} is applied, new terms are introduced in the Hamiltonian of the holes, as given by the Zeeman-Hamiltonian

$$\mathcal{H}_Z = -\mu_B(\mathbf{L} + 2\mathbf{S}) \cdot \mathcal{B} - \frac{1}{2}m^* \mu_B^2 \left\{ (r_1^2 + r_2^2)\mathcal{B}^2 - [(\mathbf{r}_1 + \mathbf{r}_2) \cdot \mathcal{B}]^2 \right\},$$

where m^* is the hole effective mass and \mathbf{L} and \mathbf{S} are the total orbital and spin angular momenta in units of \hbar . The quantity $\mathbf{L} + 2\mathbf{S}$ is the total static magnetic moment of the system. Moreover, μ_B is the Bohr magneton and \mathbf{r}_i is the position vector of the i -th hole.

The symmetry group of the Zeeman Hamiltonian \mathcal{H}_Z is $\bar{C}_{\infty h}$. Unless \mathcal{B} is directed along one of the main crystallographic axes, the symmetry group of the total Hamiltonian $\mathcal{H} = \mathcal{H}_0 + \mathcal{H}_Z$ reduces to the trivial group. When \mathcal{B} is parallel to a $\langle 100 \rangle$, $\langle 111 \rangle$ or $\langle 110 \rangle$ direction in the crystal, the symmetry group of the total Hamiltonian reduces from \bar{T}_d to \bar{S}_4 , \bar{C}_3 or \bar{C}_{1h} , respectively. The relevant character tables are given in Table A.2 and A.3 in Appendix A. Because all resulting groups are Abelian (commutative), it follows that the application of a magnetic field completely removes the degeneracy of all levels*. The way in which the Γ_i levels exactly split in a magnetic field is presented in Table 6.2.

To deduce the magnetic field induced splitting of the levels, we employ first order degenerate perturbation theory. As mentioned before, it is assumed that the separation of the levels is large compared to the splitting caused by the field, so only the subspace of Hilbert space connected to the level under consideration needs to be taken into account. Given a set of basis functions $|i\rangle$ for a particular level, we find the corresponding submatrix $\langle i | \mathcal{H}_Z | j \rangle$ of \mathcal{H}_Z and diagonalize it to obtain the splitting as a function of \mathcal{B} .

*But not necessarily in a first order approach.

Instead of trying to calculate matrix elements from \mathcal{H}_Z (after choosing a suitable set basis functions) it is much more convenient to use the well-established approach of constructing an *effective Zeeman Hamiltonian* [15]. This comprises the construction of a matrix of the required size, exploiting required symmetries to find vanishing elements and relations between elements. The result is a matrix that usually depends on a small number of unknown phenomenological parameters, in terms of which the level splitting can be expressed. The value of these parameters cannot be determined from symmetry arguments, but their value reflects the quantitative influence of, e.g., the band structure, the Jahn-Teller effect, and the crystal field. The effective Hamiltonian approach is especially advantageous in the present situation, where both the values of the parameters occurring in \mathcal{H}_Z and the unperturbed wave functions are not (exactly) known.

6.4 Linear Zeeman effect

In this section, we will investigate the first order Zeeman effect of all the double acceptor levels mentioned before.

6.4.1 The Γ_i -levels

Because Γ_4 occurs in neither of the anti-symmetric direct products $\{\Gamma_i \times \Gamma_i\}$ ($i = 1 \dots 3$), the effective Hamiltonian matrix $\mathcal{H}_{\text{eff,lin}}$ vanishes identically for the three levels Γ_i . Hence, none of these levels experiences a linear Zeeman effect.

The linear part of the effective Zeeman Hamiltonian for a Γ_4 or Γ_5 level is given by [6, 16]

$$\mathcal{H}_{\text{eff,lin}} = \mu_B g (\mathcal{B}_x J_x + \mathcal{B}_y J_y + \mathcal{B}_z J_z). \quad (6.1)$$

Here, g the gyromagnetic factor and J_x , J_y and J_z are 3×3 -matrix representations of the components of the angular momentum operator with respect to some convenient basis. The components J_α ($\alpha = x, y, z$) transform according to the Γ_4 representation of \bar{T}_d . Because $\{\Gamma_4 \times \Gamma_4\} = \{\Gamma_5 \times \Gamma_5\} = \Gamma_4$, the Γ_4 and Γ_5 level do have a linear Zeeman effect. Calculating the eigenvalues of the matrix $[\mathcal{H}_{\text{eff,lin}}]_i$ ($i = 4, 5$) yields

$$\Delta E = \begin{cases} +\mu_B g \mathcal{B} \\ 0 \\ -\mu_B g \mathcal{B} \end{cases}$$

The eigenvalues are independent of the direction of the magnetic field and hence give rise to an isotropic splitting.

6.4.2 The $\Gamma_3 + \Gamma_5$ level

The situation where the zero-field splitting of the $\Gamma_3 + \Gamma_5$ level is small compared to the Zeeman energy must be dealt with separately. Because $\Gamma_3 \times \Gamma_5 = \Gamma_4 + \Gamma_5$ contains Γ_4 , there are non vanishing cross-terms in the linear effective Zeeman Hamiltonian for a $\Gamma_3 \Gamma_5$ -level. Therefore, such a level will have a linear Zeeman shift different from that of

the individual Γ_3 and Γ_5 levels. The Hamiltonian sub-matrix for the $\Gamma_3 + \Gamma_5$ level is given by

$$\begin{pmatrix} 0 & -\frac{\sqrt{3}}{2}a_{35}\mathcal{B}_x & \frac{\sqrt{3}}{2}a_{35}\mathcal{B}_y & 0 & \\ -\frac{\sqrt{3}}{2}\bar{a}_{35}\mathcal{B}_x & -\frac{1}{2}\bar{a}_{35}\mathcal{B}_x & -\frac{1}{2}a_{35}\mathcal{B}_x & -\frac{1}{2}a_{35}\mathcal{B}_y & a_{35}\mathcal{B}_z \\ \frac{\sqrt{3}}{2}\bar{a}_{35}\mathcal{B}_y & -\frac{1}{2}\bar{a}_{35}\mathcal{B}_y & & & \\ 0 & \bar{a}_{35}\mathcal{B}_z & & & \end{pmatrix} [\mathcal{H}_{\text{eff,lin}}]_5.$$

This 5×5 -matrix is given with respect to a basis consisting of two Γ_3 wave functions and three Γ_5 -wave functions. Only the matrix-elements connecting Γ_3 functions to Γ_5 functions are shown explicitly. This part of the matrix was derived by expressing all six possible products of Γ_3 and Γ_5 wave functions as a linear combination of Γ_4 and Γ_5 wave functions, which is possible because $\Gamma_3 \times \Gamma_5 = \Gamma_4 + \Gamma_5$. This procedure is simplified by using, e.g., the coupling coefficients for $\Gamma_3 \times \Gamma_5$ as given in Ref. 17. Application of the Wigner-Eckart orthogonality theorem (see Appendix A) and the fact that all operators occurring in the linear Zeeman Hamiltonian [Eq. (6.1)] transform according to the rows of Γ_4 complete the derivation of these matrix elements. All information about the strength of the coupling is contained in the (unknown) parameter a_{35} . The upper left and bottom right parts are the same matrices as for the individual Γ_3 and Γ_5 level, respectively, as given in the previous subsection.

From this matrix, we determine the eigenvalues for \mathcal{B} parallel to the main crystallographic directions. For $\mathcal{B} \parallel \langle 100 \rangle$, so $\mathcal{B}_x = \mathcal{B}$, $\mathcal{B}_y = \mathcal{B}_z = 0$, we find

$$\Delta E = \begin{cases} 0 \\ \pm \mu_B g \mathcal{B} \\ \pm |a_{35}| \mathcal{B}. \end{cases}$$

For $\mathcal{B} \parallel \langle 111 \rangle$, so $\mathcal{B}_x = \mathcal{B}_y = \mathcal{B}_z = \mathcal{B}/\sqrt{3}$, we have

$$\Delta E = \begin{cases} 0 \\ \pm \frac{1}{2} \mu_B g \mathcal{B} \pm \frac{1}{2} \mathcal{B} \sqrt{\mu_B^2 g^2 + 2|a_{35}|^2}. \end{cases}$$

Finally for $\mathcal{B} \parallel \langle 110 \rangle$, so $\mathcal{B}_x = \mathcal{B}_y = \mathcal{B}/\sqrt{2}$ and $\mathcal{B}_z = 0$, it is found that

$$\Delta E = \begin{cases} 0 \\ \pm \frac{1}{2} |a_{35}| \mathcal{B} \\ \pm \frac{1}{2} \mathcal{B} \sqrt{2\mu_B^2 g^2 + 3|a_{35}|^2}. \end{cases}$$

We conclude that there is indeed a linear Zeeman effect in the $\Gamma_3 + \Gamma_5$ level and the size of the effect is dependent of the direction of the field with respect to the crystal.

6.5 Quadratic Zeeman effect

For some of the levels we will also give a second order approach, using the quadratic part of the effective Hamiltonian $\mathcal{H}_{\text{eff,quad}}$. Note that $\mathcal{H}_{\text{eff,quad}}$ contains both a second order

approach to the linear part of the original \mathcal{H}_Z and a first order approach to the quadratic part of the original \mathcal{H}_Z .

6.5.1 The Γ_1 and Γ_2 levels

For the Γ_1 level, the effective quadratic Zeeman Hamiltonian contains only one term and is straightforwardly given by

$$\mathcal{H}_{\text{eff,quad}} = a_1 \mathcal{B}^2,$$

where a_1 is a phenomenological parameter. The simple conclusion is that a Γ_1 level will experience a quadratic shift, independent of the direction of the magnetic field: $\Delta E = a_1 \mathcal{B}^2$. From this purely symmetry-based analysis, conclusions can be drawn neither about the magnitude of a_1 nor about its sign (that is, whether the state is diamagnetic or paramagnetic). Because $\Gamma_2 \times \Gamma_2 = \Gamma_1$, a similar expression holds for a Γ_2 level.

6.5.2 The Γ_3 level

For a Γ_3 level, the effective Hamiltonian contains two unknown parameters and is given by [8, 18]

$$\mathcal{H}_{\text{eff,quad}} = a_3 \mathcal{B}^2 + b_3 [-(2\mathcal{B}_z^2 - \mathcal{B}_x^2 - \mathcal{B}_y^2)\sigma_x + \sqrt{3}(\mathcal{B}_x^2 - \mathcal{B}_y^2)\sigma_y],$$

where σ_x and σ_y are Pauli spin matrices and a_3 and b_3 are phenomenological parameters. When $\mathcal{B} \parallel \langle 100 \rangle$ the eigenvalues are given by

$$\Delta E = (a_3 \pm 2b_3)\mathcal{B}^2.$$

This is a symmetric quadratic splitting superimposed on a quadratic shift. When $\mathcal{B} \parallel \langle 111 \rangle$, there is only one eigenvalue

$$\Delta E = a_3 \mathcal{B}^2,$$

meaning that there is no splitting in second order and the quadratic shift is the same as for $\mathcal{B} \parallel \langle 100 \rangle$. Finally, for $\mathcal{B} \parallel \langle 110 \rangle$, we find the eigenvalues

$$\Delta E = (a_3 \pm b_3)\mathcal{B}^2.$$

The Zeeman effect for this field direction is similar to $\mathcal{B} \parallel \langle 100 \rangle$, but the splitting is twice as small.

6.5.3 The Γ_4 and Γ_5 levels

Because the symmetrized squares of Γ_4 and Γ_5 satisfy $[\Gamma_4 \times \Gamma_4] = [\Gamma_5 \times \Gamma_5]$, the results for the Γ_4 and Γ_5 levels are similar. For these two levels, the quadratic part of the effective

Zeeman Hamiltonian has three unknown parameters a_i , b_i and c_i ($i = 4, 5$) and is given by [6]

$$\begin{aligned} \mathcal{H}_{\text{eff,quad}} = & a_i \mathcal{B}^2 + b_i \left[3(\mathcal{B}_x^2 J_x^2 + \mathcal{B}_y^2 J_y^2 - \mathcal{B}_z^2 J_z^2) - 2\mathcal{B}^2 \right] \\ & + c_i \left[\mathcal{B}_y \mathcal{B}_z \{J_y, J_z\} + \mathcal{B}_x \mathcal{B}_z \{J_x, J_z\} + \mathcal{B}_x \mathcal{B}_y \{J_x, J_y\} \right], \end{aligned}$$

where $\{A, B\} = \frac{1}{2}(AB + BA)$ denotes the anti-commutator of A and B . We calculate the eigenvalues of the full quadratic Hamiltonian matrix $[\mathcal{H}_{\text{eff,lin}}]_i + [\mathcal{H}_{\text{eff,quad}}]_i$ for the three main crystallographic directions. For $\mathcal{B} \parallel \langle 100 \rangle$ we have

$$\Delta E = \begin{cases} \mu_B g \mathcal{B} + (a_i + b_i) \mathcal{B}^2 \\ (a_i - 2b_i) \mathcal{B}^2 \\ -\mu_B g \mathcal{B} + (a_i + b_i) \mathcal{B}^2 \end{cases}$$

For $\mathcal{B} \parallel \langle 111 \rangle$ we have

$$\Delta E = \begin{cases} \mu_B g \mathcal{B} + (a_i + \frac{1}{6}c_i) \mathcal{B}^2 \\ (a_i - \frac{1}{3}c_i) \mathcal{B}^2 \\ -\mu_B g \mathcal{B} + (a_i + \frac{1}{6}c_i) \mathcal{B}^2. \end{cases}$$

And for $\mathcal{B} \parallel \langle 110 \rangle$ we find (up to second order in \mathcal{B})

$$\Delta E = \begin{cases} \mu_B g \mathcal{B} + (a_i + \frac{1}{4}b_i + \frac{1}{8}c_i) \mathcal{B}^2 \\ (a_i - \frac{1}{2}b_i - \frac{1}{4}c_i) \mathcal{B}^2 \\ -\mu_B g \mathcal{B} + (a_i + \frac{1}{4}b_i + \frac{1}{8}c_i) \mathcal{B}^2 \end{cases}$$

It follows that in second order the splitting is no longer symmetric and isotropic for these levels.

The Zeeman effect of the levels treated so far is schematically illustrated in Fig. 6.1.

6.6 Central field approximation

Finally we discuss the Zeeman effect for two-hole states in the central field approximation. In this approximation, we must start from the one-hole levels and their behavior in a magnetic field. The two-hole wave functions are anti-symmetrized products of one-hole wave functions and the energy levels are obtained by examining the various ways to put the two holes in the one-hole levels.

We will present results for the case where both holes are put in a Γ_8 level and $\mathcal{B} \parallel \langle 100 \rangle$ only. Similar results for the other types of levels and other directions of the field are easily obtained in an analogous way.

For a magnetic field $\mathcal{B} \parallel \langle 100 \rangle$, the single hole Γ_8 ground state is split into Γ_5 , Γ_6 , Γ_7 and Γ_8 -levels of \bar{S}_4 [6]. Because holes are fermions, each of these non-degenerate levels can be occupied by at most one hole. By putting each of the two holes in a different level, this gives rise to six two-hole levels $\Gamma_5 \times \Gamma_6 = \Gamma_1$, $\Gamma_5 \times \Gamma_7 = \Gamma_3$, $\Gamma_5 \times \Gamma_8 = \Gamma_2$, $\Gamma_6 \times \Gamma_7 = \Gamma_2$, $\Gamma_6 \times \Gamma_8 = \Gamma_4$, and $\Gamma_7 \times \Gamma_8 = \Gamma_1$, where all representations are of \bar{S}_4 .

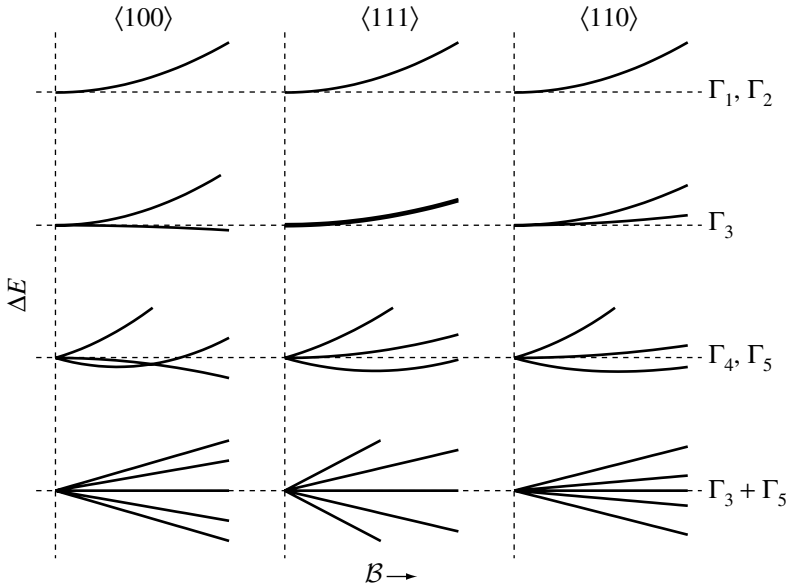


Figure 6.1 Schematic overview of level splitting in a magnetic field along the main crystallographic axes in several kinds of two-hole acceptor levels. The figure illustrates the qualitative aspects of the splitting. The values of the parameter have been chosen to emphasize these features.

The energy shifts of the single-hole levels have been determined experimentally [6]. The shifts of the two-hole levels can be calculated as the sum of the shifts of the individual single hole levels from which they are composed. This results in a linear shift for each two-hole level, given by $\mu_B g \mathcal{B}$, with $g = \frac{3}{2}g_{3/2} + \frac{1}{2}g_{1/2}$ for Γ_2 , $g = \frac{3}{2}g_{3/2} - \frac{1}{2}g_{1/2}$ for Γ_4 , $g = 0$ for $2\Gamma_1$, $g = -\frac{3}{2}g_{3/2} + \frac{1}{2}g_{1/2}$ for Γ_3 and $g = -\frac{3}{2}g_{3/2} - \frac{1}{2}g_{1/2}$ for Γ_2 . The parameters $g_{3/2}$ and $g_{1/2}$ are the g -factors for the single hole $j = \frac{3}{2}$ and $j = \frac{1}{2}$ -levels respectively. Experimental values for B^0 in Si are $g_{3/2} = 1.12$ and $g_{1/2} = 1.04$ [7]. In the above, a small overall shift is neglected.

6.7 Application to B^+

Only states arising from $\{\Gamma_8 \times \Gamma_8\}$ (see Table 6.1) are candidates for the B^+ ground state. These are $\Gamma_1, \Gamma_3, \Gamma_5, \Gamma_3 + \Gamma_5$ and the unsplit (central field) $\{\Gamma_8 \times \Gamma_8\}$. Each of these five possibilities for the B^+ ground state will be compared to existing experimental data. From the previous section, we conclude that all possible ground state levels behave qualitatively differently in a magnetic field. Therefore, it is in principle possible to determine the nature of the actual ground state of B^+ from the analysis of a sufficiently detailed experiment. Though this approach is hampered by the fact that the values of the parameters are not

known, it is possible to draw conclusions based on the qualitative characteristics, such as linear or quadratic splitting/shift and the asymmetry of the splitting.

We refer to our recent experiments reported in Ref. 4 and summarize the main observations. The ground state energy shifts upwards (that is, in the direction of the valence band) and is therefore diamagnetic. The shift has both a linear and a quadratic component. The total shift amounts to 1 meV at a magnetic field of 14 T and was equal for the $\langle 100 \rangle$ and $\langle 110 \rangle$ directions (see Fig. 6.2). The width of the observed peak (full width at half maximum) increased from 1.2 meV to 1.5 meV in the same magnetic field range. Within the experimental error (~ 0.2 meV), no splitting of the peak was detected*.

The experimentally observed super linear overall shift, independent from the direction of \mathcal{B} , best matches the behavior of a Γ_1 state, although this leaves the strong linear component in the measured magnetic field dependence unexplained. Therefore, we believe that the ground state of B^+ is indeed a Γ_1 state. This hypothesis does imply that the observed linear component in the peak shift and the peak broadening are due to other processes (e.g. the Stark effect) as already suggested in Ref. 4.

The broadening in the observed peak is linear in the magnetic field and independent of its direction. Therefore, it cannot be explained as unresolved splitting of a Γ_3 level. A Γ_5 or $\Gamma_3 + \Gamma_5$ ground state would give rise to linear splitting (broadening), but no overall shift would be expected in first order. Moreover, the magnitude of the splitting in a $\Gamma_3 + \Gamma_5$ level would depend on the magnetic field direction. Therefore, these possibilities are not consistent with the experimental observations. Only when the parameter a_3 (a_5) would much larger than all other relevant parameters (that is $a_3 \ll b_3$ or $a_5 \ll b_5, c_5, \mu_b g/\mathcal{B}$), the magnetic field dependence of the Γ_3 (Γ_5) state would be similar to that of the Γ_1 state. In that case, Γ_3 , Γ_5 and $\Gamma_3 + \Gamma_5$ states cannot be rejected as potential ground state symmetries for B^+ .

The central field approach is unlikely to yield good results for B^+ , for which the wave functions of the two holes are expected to overlap considerably (due to the small nuclear charge). The peak splitting (or broadening, due to unresolved splitting) expected in this approach between the two Γ_2 levels would be given by $2\mu_B(\frac{3}{2}g_{3/2} + \frac{1}{2}g_{1/2})B$. Assuming the B^0 -values of the g -factors are valid here, this would amount to 3.6 meV for $B = 14$ T. This is much larger than the observed 0.3 meV increase of the FWHM of the measured resonance peak. Moreover, the 1 meV shift observed in the experiment is much larger than the expected overall peak shift in this approach. Therefore, the description of the B^+ ground state in the central field approximation is not consistent with the experimental observations.

In summary, magnetic field dependent measurements indicate that the B^+ ground state is a non-degenerate Γ_1 state. It would be interesting to have higher resolution spectroscopy data available, in order to exclude that the observed peak broadening is due to unresolved splitting. It is worth emphasizing that in our analysis, we only made use of the fact that B^+ is a double acceptor and the symmetry properties which follow from that. Knowledge of the B^+ ground state *wave function* would allow for obtaining quantitative information

*In these experiments the concentration of B-impurities in the silicon was so high that they cannot be considered as fully isolated as proven by the increased binding energy of the second hole in the B^+ -state. The interaction of a B^+ state with neighboring B^0 states is however not expected to change the nature of its ground state.

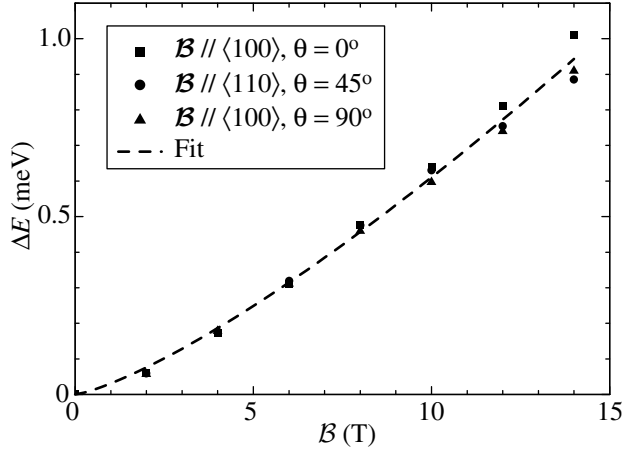


Figure 6.2 Magnetic field induced shift of the B^+ ground state deduced from electrical transport measurements [4]. The angle between the magnetic field and the current is denoted by θ . The expression $\Delta E \propto B(1 + \alpha B)$ was fit to the data, yielding $\alpha = 0.046 \text{ T}^{-1}$.

about the phenomenological parameters, which would be advantageous in the interpretation of experimental data.

6.8 Conclusions

In conclusion, we have presented a general group theoretical study of the magnetic field dependence of two-hole states of acceptors in tetrahedral semiconductors. We have used our results to analyze our experimental observations from Chapter 5. This analysis indicates that the B^+ ground state is most compatible with a Γ_1 state.

- [1] P. Norton, Phys. Rev. Lett. **37**, 164 (1976).
- [2] B. E. Kane, Nature **393**, 133 (1998).
- [3] W. Burger and K. Lassmann, Phys. Rev. Lett. **53**, 2035 (1984).
- [4] J. Caro, I. D. Vink, G. D. J. Smit, S. Rogge, T. M. Klapwijk, R. Loo, and M. Caymax (2003), cond-mat/0309139.
- [5] A. Ramdas and S. Rodriguez, Rep. Prog. Phys. **44**, 1297 (1981).
- [6] A. K. Bhattacharjee and S. Rodriguez, Phys. Rev. B **6**, 3836 (1972).
- [7] F. Merlet, B. Pajot, P. Arcas, and A. M. Jean-Louis, Phys. Rev. B **12**, 3297 (1975).
- [8] E. Kartheuser and S. Rodriguez, Phys. Rev. B **8**, 1556 (1973).
- [9] A. V. Rodina, Solid-State Comm. **85**, 23 (1993).
- [10] F. S. Ham and C.-H. Leung, Phys. Rev. Lett. **71**, 3186 (1993).
- [11] F. S. Ham and C.-H. Leung, Solid-State Comm. **93**, 375 (1995).

- [12] N. Sugimoto, S. Narita, M. Taniguchi, and M. Kobayashi, *Solid-State Comm.* **30**, 395 (1979).
- [13] P. Gross and K. Lassmann, *Ann. Phys.* **4**, 503 (1995).
- [14] S. Roshko and W. Dietsche, *Solid-State Comm.* **98**, 453 (1996).
- [15] B. S. Tsukerblat, *Group theory in chemistry and spectroscopy*, Theoretical chemistry (Academic press Ltd., London, 1994).
- [16] J. M. Luttinger, *Phys. Rev.* **102**, 1030 (1956).
- [17] G. F. Koster, J. O. Dimmock, R. G. Wheeler, and H. Satz, *Properties of the thirty-two point groups* (M.I.T. Press, Cambridge, 1963).
- [18] S. Washimiya, K. Shinagawa, and S. Sugano, *Phys. Rev. B* **1**, 2976 (1970).



Stark effect of shallow impurities in Si

Abstract — We have theoretically studied the effect of an electric field on the energy levels of shallow donors and acceptors in silicon. An analysis of the electric field dependence of the lowest energy states in donors and acceptors is presented, taking the bandstructure into account. A description as hydrogen-like impurities was used for accurate computation of energy levels and lifetimes up to large (several MV/m) electric fields. All results are discussed in connection with atomic scale electronics and solid state quantum computation.*

7.1 Introduction

Manipulation of a single particle's wave functions can be realized by using a local magnetic or electric field. Such a field can be used either to perform the desired manipulation itself, or to provide a local perturbation allowing for addressing a single impurity by a global radiation field. A local electric field could be realized by putting a small gate close to a dopant atom, which is in principle accomplishable with current technology. An ultimate application of gate-manipulation is found in the solid state quantum computer as proposed by Kane [1, 2].

To get more insight in the physics of atomic scale electronic devices, it is essential to try to predict their potential behavior. A first step is the description of isolated dopant atoms in a (homogeneous) electric field. Much more difficult is accurate modelling of a the time evolution of a dopant atom wave function in an inhomogeneous field and the description of the interaction of two or more dopants in a field.

*This chapter is based on the following manuscript: G. D. J. Smit, S. Rogge, J. Caro, and T. M. Klapwijk, cond-mat/0310492 (2003), submitted to Phys. Rev. B.

Dopant atoms binding one electron or hole can be described as a hydrogen atom, where the vacuum values of the dielectric constant and the electron mass are replaced by the appropriate values for the semiconductor. This ‘scaled hydrogen model’ (SHM) provides a reasonable description of the dopant atom’s energy levels. Therefore, it is useful to look at existing studies of the Stark effect in the hydrogen atom. Calculation of the shift and splitting of the hydrogen energy levels up to very large electric field have been carried out by several different methods [3, 4, 5]. Within the SHM, these results can be directly translated to dopant atoms in a uniform electric field. However, we found that almost no actual results of such calculations in the (field)range of interest for ASE have been published.

The SHM also offers a manageable way to describe a dopant atom in an inhomogeneous electric field. Recently, several calculations using this framework have been published [6, 7, 8] in the context of quantum computing. However, the SHM fails in the explanation of effects where it is essential that the bandstructure of the semiconductor is taken into account (as an example, see Ref. 9).

Many measurements of the energy levels of dopant atoms in semiconductors (large ensembles) are known, but only a few concerning the effect of a uniform electric field have been reported, presumably because such measurements are much more difficult than e.g. measurements in a magnetic field or under stress. Among them are spectroscopic measurements of the boron energy levels in silicon subject to electric fields up to 0.15 MV/m [10]. Electron-spin-resonance experiments [11] demonstrated that the electric field couples linearly to the acceptor ground state. The magnitude of the effective electric dipole moment for linear Stark coupling has been estimated as 0.26 D for boron acceptors in silicon (1 D = 3.3×10^{-30} Cm). Photo-ionization measurements have shown a very large electric field effect on the phosphorus ground state in Si [12], but this was measured in highly doped samples where the interaction between dopants dominates the Stark effect of individual energy levels. Finally, quadratic level shifts have been observed in deep selenium double donors in Si, located in the space charge region of a diode [13].

In this paper, we will theoretically investigate the effect of a uniform electric field on isolated shallow impurities in silicon. Primary interest for ASE will be in the ground state and possibly the first few excited states. These states are the only ones that are well separated from neighboring levels and at low temperatures only the ground state is occupied. Therefore, we focus on the lowest energy states of impurities in silicon. First, we derive the shift, splitting and wave functions of the lowest donor levels in silicon in a small uniform electric field, taking full account of the multiple valley conduction band structure (Sec. 7.2). We briefly outline a similar calculation for acceptors in silicon (Sec. 7.3). The results are useful for applications where a local gate is used to bring a single dopant atom into resonance with a global radiation field (nuclear magnetic resonance, electron spin resonance). Moreover, they can be used to outline the limitations of the SHM. Second, in Sec. 7.4 we present accurate numerical calculation of the Stark effect in silicon within SHM, from zero field up to fields that are relevant for atomic scale electronics and quantum computing (several MV/m; see for instance Ref. 2). Finally, we conclude by discussing possible extensions and alternatives of our methods which are useful to address issues in ASE (Sec. 7.5).

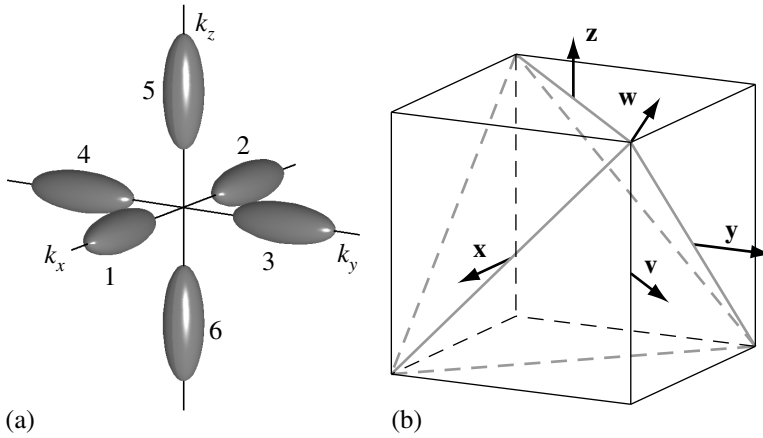


Figure 7.1 (a) Schematic representation of the conduction band valleys of silicon as constant energy surfaces in k -space. The six valleys are labelled by numbers, e.g. 4 represents the $[0\bar{1}0]$ valley. (b) Definition of the coordinate system with respect to the Si-crystal unit cell. We have $x \parallel [100]$, $y \parallel [010]$, $z \parallel [001]$, $v \parallel [110]$, and $w \parallel [111]$. The orientation of the figure in part (a) and (b) is the same.

7.2 Donors

7.2.1 The donor ground state

Group theory is a powerful tool to derive various properties of dopant wave functions in a semiconductor. In order to provide the necessary background and to fix the notation, we will briefly review some relevant properties of donor levels in silicon (see e.g. Ref. 14). Degeneracy due to spin is not lifted by an electric field in donors. For simplicity, we will therefore not count those degeneracies in this section.

The conduction band of silicon has six equivalent minima located on the $[100]$ and equivalent axes. These minima are commonly called ‘valleys’ and we label them by the numbers 1 to 6 as shown in Fig. 7.1(a). The band structure in the vicinity of valley 1, located in k -space at $\mathbf{k}_1 = (k_0, 0, 0)$, can be approximated as

$$E = E_0 + \frac{\hbar^2}{2m_{\parallel}}(k_x - k_0)^2 + \frac{\hbar^2}{2m_{\perp}}(k_y^2 + k_z^2),$$

where $m_{\parallel} = 0.98m$ and $m_{\perp} = 0.19m$ are the electron effective masses and m is the free electron mass. Furthermore, $k_0 = 0.85\frac{2\pi}{a}$ [15], where a is the size of the silicon unit cell. Similar expressions hold for the remaining five valleys.

From effective mass theory (EMT) it follows that the ground state wave function of the Hamiltonian of an electron bound to a donor can be written as [16]

$$\Psi(\mathbf{r}) = \sum_{\mu=1}^6 \alpha_{\mu} F_{\mu}(\mathbf{r}) \varphi_{\mu}(\mathbf{r}), \quad (7.1)$$

where the α_μ are numerical coefficients and the $F_\mu(\mathbf{r})$ are envelope wave functions, which are slowly varying on the length scale of a . $F_1(\mathbf{r}) = F_2(\mathbf{r})$ satisfy the hydrogen-like Schrödinger equation

$$-\left[\frac{\hbar^2}{2m_{\parallel}} \frac{\partial^2}{\partial x^2} + \frac{\hbar^2}{2m_{\perp}} \left(\frac{\partial^2}{\partial y^2} + \frac{\partial^2}{\partial z^2} \right) + \frac{e^2}{4\pi\epsilon r} \right] F(\mathbf{r}) = E F(\mathbf{r}) \quad (7.2)$$

and similar equations hold for the remaining F_μ . The $\varphi_\mu(\mathbf{r})$ are Bloch-wave functions at the minimum of valley μ and can be written as $e^{i\mathbf{k}_\mu \cdot \mathbf{r}} u_\mu(\mathbf{r})$, where $u_\mu(\mathbf{r})$ has the periodicity of the silicon crystal lattice. Because for all μ the eigenvalues resulting from Eq. (7.2) are the same, Eq. (7.1) shows that the degeneracy of each of these eigenvalues is multiplied by six for the total wave functions $\Psi(\mathbf{r})$. In particular, the ground state solution of Eq. (7.2) gives rise to a six-fold degenerate donor ground state.

The symmetry group of the conduction band minima (and thus of the Bloch functions $\varphi(\mathbf{r})$) is $C_{\infty v}$ in EMT, which reduces to C_{2v} in the silicon crystal*. The envelope wave functions $F(\mathbf{r})$ belong to $D_{\infty h}$. Their products belong to the cross-section of both groups, which is C_{2v} . For the $1s$ -like ($m = 0$) ground state function of Eq. 7.2 $F_\mu(\mathbf{r})$, such a product transforms according to the Γ_1 representation of the valley symmetry group C_{2v} . Because the donor is located at a substitutional site of the tetrahedral silicon lattice, the total wave function has T_d -symmetry. Using Frobenius' theorem [17], it can be shown that the Γ_1 representation of C_{2v} induces the $\Gamma_1 + \Gamma_3 + \Gamma_5$ representation[†] of T_d . This means that linear combinations of the $F_\mu(\mathbf{r})$ can be found that have the correct transformation properties under T_d . Using the notation $\alpha = (\alpha_1, \dots, \alpha_6)$ (as in Eq. 7.1) the reduction to the T_d representations is carried out by

$$\begin{aligned} \alpha_g &= \frac{1}{\sqrt{6}}(1, 1, 1, 1, 1, 1) && \Gamma_1 \\ \alpha_r &= \frac{1}{\sqrt{12}}(-1, -1, -1, -1, 2, 2) && \left. \vphantom{\alpha_r} \right\} \Gamma_3 \\ \alpha_s &= \frac{1}{2}(1, 1, -1, -1, 0, 0) && \\ \alpha_x &= \frac{1}{\sqrt{2}}(1, -1, 0, 0, 0, 0) && \left. \vphantom{\alpha_x} \right\} \Gamma_5 \\ \alpha_y &= \frac{1}{\sqrt{2}}(0, 0, 1, -1, 0, 0) && \\ \alpha_z &= \frac{1}{\sqrt{2}}(0, 0, 0, 0, 1, -1) && \end{aligned} \quad (7.3)$$

Each of the vectors α defines a wave function Ψ through Eq. 7.1. Here, the basis functions of the two- and three dimensional representations have been chosen such that Ψ_r and Ψ_s transform under T_d as $3z^2 - r^2$ and $\sqrt{3}(x^2 - y^2)$, respectively. Similarly, Ψ_x , Ψ_y and Ψ_z have been chosen such that they transform under T_d as x , y and z , respectively.

The potential term in the EMT-Schrödinger equation (7.2) is a good approximation only for $r \gtrsim a$, where a is the lattice constant of silicon. For small r , the charge of the nucleus is not screened by other electrons and it will attract electrons much stronger than described by the potential in Eq. (7.2). Because the symmetry of the potential is not

*All relevant character tables can be found in Appendix A.

[†]In literature discussing donors in silicon, it is more common to denote the single valued representations of T_d by A_1, A_2, E, T_1 and T_2 , while for acceptors usually Γ_i ($i = 1 \dots 5$) are used.

Table 7.1 Reduction of the site symmetry of an impurity in a uniform electric field in various directions and the resulting reduction of the irreducible representations [20].

Direction Group	$\langle 100 \rangle$ \bar{C}_{2v}	$\langle 111 \rangle$ \bar{C}_{3v}	$\langle 110 \rangle$ \bar{C}_s
$\Gamma_1 (T_d)$	Γ_1	Γ_1	Γ_1
$\Gamma_2 (T_d)$	Γ_3	Γ_2	Γ_2
$\Gamma_3 (T_d)$	$\Gamma_1 + \Gamma_3$	Γ_3	$\Gamma_1 + \Gamma_2$
$\Gamma_4 (T_d)$	$\Gamma_2 + \Gamma_3 + \Gamma_4$	$\Gamma_2 + \Gamma_3$	$\Gamma_1 + 2\Gamma_2$
$\Gamma_5 (T_d)$	$\Gamma_1 + \Gamma_2 + \Gamma_4$	$\Gamma_1 + \Gamma_3$	$2\Gamma_1 + \Gamma_2$
$\Gamma_6 (\bar{T}_d)$	Γ_5	Γ_4	Γ_{3+4}
$\Gamma_7 (\bar{T}_d)$	Γ_5	Γ_4	Γ_{3+4}
$\Gamma_8 (\bar{T}_d)$	$2\Gamma_5$	$\Gamma_4 + \Gamma_{5+6}$	$2\Gamma_{3+4}$

affected, the states are still described by the representations of T_d , but they are no longer degenerate. The Γ_1 state Ψ_g is the only one of the six ground state wave functions that has non-zero electron density at the nucleus ($\mathbf{r} = 0$). Therefore, it has a larger binding energy than predicted by EMT and for most donors in silicon the $1s(\Gamma_1)$ state is the true ground state. This effect is generally called ‘chemical splitting’ (because the size of the effect depends on the donor in question) or ‘valley-orbit splitting’. The remaining states (especially the non- s states) are quite well described by EMT, because the electron density at the nucleus is negligible. As an example, in case of phosphorus in silicon, the $1s(\Gamma_1)$ state (the ground state) has been measured to be located 45.29 meV below the conduction band minimum [18], while the EMT-prediction is 31.27 meV [19].

7.2.2 Symmetry of the donor ground state in an electric field

After this brief review of established knowledge of silicon donors, we return to the main subject of this paper. From purely symmetry based considerations, we can find how the Hilbert subspace spanned by the original six valley wave functions is decomposed by the application of an electric field in a certain direction. The impurities considered in this paper occupy substitutional sites in the silicon lattice and their wave functions transform according to representations of site symmetry group \bar{T}_d . The symmetry group of a uniform electric field \mathcal{E} is $C_{\infty v}$. When \mathcal{E} is applied in an arbitrary direction in the silicon crystal, the symmetry group \bar{T}_d of the Hamiltonian reduces to the trivial group C_1 . Only when the direction of the field is along one of the main crystallographic directions of the crystal, the result is C_{2v} for $\mathcal{E} \parallel \langle 100 \rangle$, C_{3v} for $\mathcal{E} \parallel \langle 111 \rangle$, and C_s for $\mathcal{E} \parallel \langle 110 \rangle$. The reduction of symmetry can induce a splitting in the original energy levels as shown in Table 7.1. As expected, the electric field does not remove degeneracy due to time reversal symmetry and therefore all resulting levels are at least two-fold degenerate.

To make the connection to the valley wave functions $F_\mu(\mathbf{r})\phi_\mu(\mathbf{r})$, we will now discuss the symmetry of the $1s$ levels in an electric field from another point of view. We start by looking at the individual valley wave functions and subsequently derive which linear com-

binations form appropriate donor wave functions (using the method of Ref. 21). When a donor impurity in silicon is situated in an electric field along the positive z -direction, the valleys 5 and 6 keep their C_{2v} symmetry, while the field reduces the symmetry group of the other four valleys to C_1 . These four valleys are mixed by the elements of the site symmetry group C_{2v} and are therefore grouped together in the third column of Table 7.2.

In case of a $1s$ state, the valley wave functions belong to the Γ_1 representation of C_{2v} (for valley 5 and 6) or C_1 (for 1, 2, 3 and 4). This is found by reducing the even $m = 0$ representation of $D_{\infty h}$ to C_{2v} and C_1 , respectively. By using Frobenius' theorem, it can be deduced that these generate for the impurity wave function the representations Γ_1 and $\Gamma_1 + \Gamma_2 + \Gamma_3 + \Gamma_4$ of C_{2v} , respectively. This is also shown in Table 7.2, together with the (set of) induced wave function(s) spanning the subspace of that representation. In a similar way, we obtained results for the electric field in the other main crystallographic directions. They are also shown in the table.

Due to the valley-orbit splitting (which has been ignored so far) the three irreducible components of the donor ground state are already energetically separated at zero field. Therefore, the basis vectors have to be chosen in such a way that they agree with the zero-field energy splitting of the Γ_1 , Γ_3 and Γ_5 levels of T_d .^{*} The result for various directions of the electric field is shown in Table 7.3.

7.2.3 Shift and splitting in an electric field

Now, we will derive the shift and splitting of the lowest donor levels in an electric field from a perturbation calculation. Results for other levels can be derived using the same method, although (because the level spacing is smaller for higher levels) the range of fields where the perturbation calculation is valid is much smaller.

Although the six-fold degeneracy of the $1s$ -levels is lifted by the valley orbit interaction, the complete manifold is relatively well-separated from the higher levels (the separation of the highest $1s(\Gamma_3)$ level to closest excited level ($2p_0$) is roughly twice as large as the separation between the $1s(\Gamma_1)$ and $1s(\Gamma_3)$ levels). Therefore, we consider the $1s$ -manifold as a whole in a single perturbation calculation, taking only the coupling among the $1s$ levels themselves into account.

The electric field couples to the (induced) dipole moment $\mathbf{D} = e\mathbf{r}$ of the impurity state and gives rise to an additional term in its Hamiltonian $-\mathcal{E} \cdot \mathbf{D}$, reflecting the energy associated with the dipole in the field. By making use of the Wigner-Eckart orthogonality theorem from group theory [22], it is possible to find the vanishing matrix elements as well as the dependencies between the non-vanishing matrix elements, as they follow from the symmetry of the system. The $1s$ sub-matrix $[\mathcal{H}]$ of the total Stark Hamiltonian

^{*}It is known from group theory that the reduction of a representation containing more than one instance of the same irreducible representation is not uniquely determined.

Table 7.2 Considering the symmetry of the valley wave functions in an electric field, the symmetry of the total wave function they induce can be obtained. The results for the $1s$ level, without considering valley-orbit splitting, are shown in this table. The direction of \mathcal{E} in the first column is denoted by the vectors defined in Fig. 7.1(a). The fifth column lists the representations of the appropriate site symmetry group, given in the second column. The basis vectors are given in the notation of Eq. (7.3).

Dir. \mathcal{E}	Site sym.	Valley	Valley sym.	Γ (site)	Basis	
\mathbf{z}	C_{2v}	1, 2, 3, 4	C_1	Γ_1	(1, 1, 1, 1, 0, 0)	
				Γ_2	(1, -1, 1, -1, 0, 0)	
				Γ_3	(1, 1, -1, -1, 0, 0)	
				Γ_4	(1, -1, -1, 1, 0, 0)	
		5	C_{2v}	Γ_1	(0, 0, 0, 0, 1, 0)	
		6	C_{2v}	Γ_1	(0, 0, 0, 0, 0, 1)	
\mathbf{w}	C_{3v}	1, 3, 5	C_s	Γ_1	(1, 0, 1, 0, 1, 0)	
				Γ_3	($\omega^2, 0, \omega, 0, 1, 0$) ($\omega, 0, \omega^2, 0, 1, 0$)	
		2, 3, 6	C_s	Γ_1	(0, 1, 0, 1, 0, 1)	
				Γ_3	(0, $\omega^2, 0, \omega, 0, 1$) (0, $\omega, 0, \omega^2, 0, 1$)	
\mathbf{v}	C_s	1, 3	C_1	Γ_1	(1, 0, 1, 0, 0, 0)	
				Γ_2	(1, 0, -1, 0, 0, 0)	
			2, 4	C_1	Γ_1	(0, 1, 0, 1, 0, 0)
					Γ_2	(0, 1, 0, -1, 0, 0)
		5	C_s	Γ_1	(0, 0, 0, 0, 1, 0)	
		6	C_s	Γ_1	(0, 0, 0, 0, 0, 1)	

$\mathcal{H} = \mathcal{H}_0 + \mathcal{E} \cdot \mathbf{D}$ is given by

$$\begin{pmatrix} E_1 & 0 & 0 & p_{15}\mathcal{E}_x & p_{15}\mathcal{E}_y & p_{15}\mathcal{E}_z \\ 0 & E_3 & 0 & -p_{35}\mathcal{E}_x & -p_{35}\mathcal{E}_y & 2p_{35}\mathcal{E}_z \\ 0 & 0 & E_3 & p_{35}\sqrt{3}\mathcal{E}_x & -p_{35}\sqrt{3}\mathcal{E}_y & 0 \\ \bar{p}_{15}\mathcal{E}_x & -\bar{p}_{35}\mathcal{E}_x & \bar{p}_{35}\sqrt{3}\mathcal{E}_x & E_5 & p_5\mathcal{E}_z & p_5\mathcal{E}_y \\ \bar{p}_{15}\mathcal{E}_y & -\bar{p}_{35}\mathcal{E}_y & \bar{p}_{35}\sqrt{3}\mathcal{E}_y & \bar{p}_5\mathcal{E}_z & E_5 & p_5\mathcal{E}_x \\ \bar{p}_{15}\mathcal{E}_z & 2\bar{p}_{35}\mathcal{E}_z & 0 & \bar{p}_5\mathcal{E}_y & \bar{p}_5\mathcal{E}_x & E_5 \end{pmatrix}.$$

The elements of this matrix are given by $[\mathcal{H}]_{ij} = \langle \varphi_i | \mathcal{H} | \varphi_j \rangle$, where the wave functions φ_i are taken from the basis $(\Psi_g, \Psi_r, \Psi_s, \Psi_x, \Psi_y, \Psi_z)$ as defined before. The energies E_1 , E_3 and E_5 are the eigenvalues of the unperturbed Hamiltonian \mathcal{H}_0 , that is the zero-field

Table 7.3 Reduction of the $1s$ donor energy levels in an electric field. The basis vectors belonging to these states are given (in the notation of Eq. (7.3)) in the limit $\mathcal{E} \rightarrow 0$ ($\omega = e^{2\pi i/3}$). The eigenvalues (up to second order in \mathcal{E}) are the result of the perturbation calculation described in the text.

$\mathcal{E} \parallel \dots$	$\mathcal{E} = 0$	$\mathcal{E} \neq 0$	Basis vector(s)	Eigenvalue
z	$\Gamma_1(T_d)$	$\Gamma_1(C_{2v})$	$(1, 1, 1, 1, 1, 1)/\sqrt{6}$	$E_1 - \frac{ p_{15} ^2}{E_5 - E_1} \mathcal{E}^2$
	$\Gamma_3(T_d)$	$\Gamma_1(C_{2v})$	$(1, 1, 1, 1, -2, -2)/\sqrt{12}$	$E_3 + \frac{ 2p_{35} ^2}{E_3 - E_1} \mathcal{E}^2$
		$\Gamma_3(C_{2v})$	$(1, 1, -1, 1, 0, 0)/2$	E_3
	$\Gamma_5(T_d)$	$\Gamma_1(C_{2v})$	$(0, 0, 0, 0, 1, -1)/\sqrt{2}$	$E_5 + \left(\frac{ p_{15} ^2}{E_5 - E_1} + \frac{ 2p_{35} ^2}{E_3 - E_1}\right) \mathcal{E}^2$
		$\Gamma_2(C_{2v})$	$(1, -1, 1, -1, 0, 0)/\sqrt{2}$	$E_5 + p_5 \mathcal{E}$
$\Gamma_4(C_{2v})$		$(1, -1, -1, 1, 0, 0)/\sqrt{2}$	$E_5 - p_5 \mathcal{E}$	
w	$\Gamma_1(T_d)$	$\Gamma_1(C_{3v})$	$(1, 1, 1, 1, 1, 1)/\sqrt{6}$	$E_1 - \frac{ p_{15} ^2}{E_5 - E_1} \mathcal{E}^2$
	$\Gamma_3(T_d)$	$\Gamma_3(C_{3v})$	$(\omega^2, \omega^2, \omega, \omega, 1, 1)/\sqrt{6}$	$E_3 + \frac{2 p_{35} ^2}{E_3 - E_5} \mathcal{E}^2$
			$(\omega, \omega, \omega^2, \omega^2, 1, 1)/\sqrt{6}$	
	$\Gamma_5(T_d)$	$\Gamma_1(C_{3v})$	$(1, -1, 1, -1, 1, -1)/\sqrt{6}$	$E_5 \pm \frac{2}{3} \sqrt{3} p_5 \mathcal{E}$ $+ \left(\frac{ p_{15} ^2}{E_5 - E_1} - \frac{4 p_{35} ^2}{E_3 - E_5}\right) \mathcal{E}^2$
		$\Gamma_3(C_{3v})$	$(\omega^2, -\omega^2, \omega, -\omega, 1, -1)/\sqrt{6}$ $(\omega, -\omega, \omega^2, -\omega^2, 1, -1)/\sqrt{6}$	$E_5 \mp \frac{1}{3} \sqrt{3} p_5 \mathcal{E}$
v	$\Gamma_1(T_d)$	$\Gamma_1(C_s)$	$(1, 1, 1, 1, 1, 1)/\sqrt{6}$	$E_1 - \frac{ p_{15} ^2}{E_5 - E_1} \mathcal{E}^2$
	$\Gamma_3(T_d)$	$\Gamma_1(C_s)$	$(1, 1, 1, 1, -2, -2)/\sqrt{12}$	$E_3 + \frac{ p_{35} ^2}{E_3 - E_1} \mathcal{E}^2$
		$\Gamma_2(C_s)$	$(1, 1, -1, 1, 0, 0)/2$	$E_3 + \frac{3 p_{35} ^2}{E_3 - E_1} \mathcal{E}^2$
	$\Gamma_5(T_d)$	$\Gamma_1(C_s)$	$(0, 0, 0, 0, 1, -1)/\sqrt{2}$	$E_5 + p_5 \mathcal{E}$ $-\frac{1}{2} \left(\frac{ p_{35} ^2}{E_3 - E_1} - \frac{ p_{15} ^2}{E_5 - E_1}\right) \mathcal{E}^2$
		$\Gamma_1(C_s)$	$(1, -1, 1, -1, 0, 0)/\sqrt{2}$	$E_5 - p_5 \mathcal{E}$ $-\frac{1}{2} \left(\frac{ p_{35} ^2}{E_3 - E_1} - \frac{ p_{15} ^2}{E_5 - E_1}\right) \mathcal{E}^2$
	$\Gamma_2(C_s)$	$(1, -1, -1, 1, 0, 0)/\sqrt{2}$	$E_5 - \frac{3 p_{35} ^2}{E_3 - E_1} \mathcal{E}^2$	

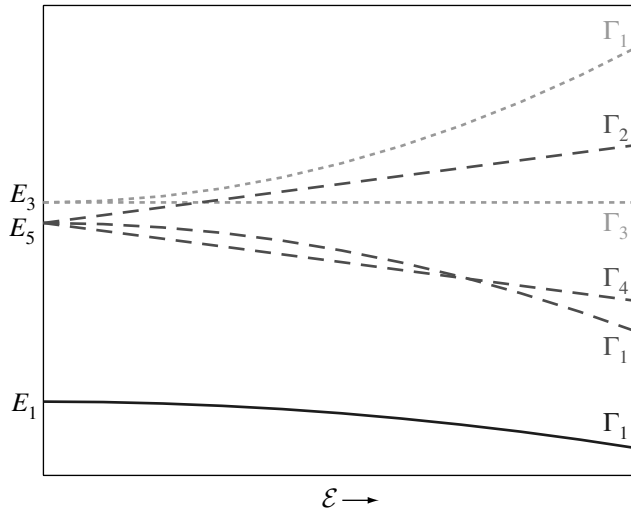


Figure 7.2 Schematic plot of the $1s$ energy levels as a function of the electric field \mathcal{E} . The values of the parameters p_5 , p_{15} , and p_{35} have been chosen such that the plot clearly illustrates the qualitative features of the Stark effect in the energy levels.

energies of the $1s(\Gamma_1)$, $1s(\Gamma_3)$ and $1s(\Gamma_5)$ level, respectively. For phosphorous in silicon, the values are $E_1 = -45.59$ meV, $E_3 = -32.58$ meV, and $E_5 = -33.89$ meV with respect to the conduction band edge [18]. The parameters p_{15} , p_{35} and p_5 describe the coupling between the $1s$ -levels. As can be seen, these are the only three independent parameters describing the coupling between the levels. They can be expressed in terms of integrals over products of wave functions, e.g. $p_{15} = e\langle\Psi_g|x|\Psi_x\rangle$ and $p_5 = e\langle\Psi_y|x|\Psi_z\rangle$.

Perturbation theory is invoked by calculating the eigenvalues and eigenvectors of this 6×6 matrix up to second order in \mathcal{E} . This yields the $1s$ energy levels and wave functions as a function of electric field for \mathcal{E} along the three main crystallographic directions. The energy levels are presented in the last column of Table 7.3. From Table 7.3 it can be seen that the $1s(\Gamma_1)$ ground state experiences an isotropic quadratic shift downwards*, while for the other levels the behavior depends on the direction of the electric field. In Figure 7.2 the results for $\mathcal{E} \parallel \langle 100 \rangle$ are plotted schematically.

The corresponding eigenvectors were also obtained from this calculation. In the limit $\mathcal{E} \rightarrow 0$ they coincide with the vectors given in Table 7.3, allowing to label each eigenvalue with the correct representation. These results are directly applicable in the prediction of allowed optical transitions between the various levels.

We discuss the behavior of the three $1s$ states in in some more detail. The normalized eigenfunctions in an electric field parallel to \mathbf{z} (again up to second order in \mathcal{E}) correspond-

*In general, the shift of a Γ_1 level cannot have any dependence on the direction of the field.

ing to the eigenvalues already given in Table 7.3 are

$$\begin{aligned}
 \Phi_g &= (1 - \frac{1}{2}|\beta|^2\mathcal{E}^2)\Psi_g + \beta''\mathcal{E}^2 \cdot \Psi_r - \bar{\beta}\mathcal{E} \cdot \Psi_z \\
 \Phi_r &= -\bar{\beta}''\mathcal{E}^2 \cdot \Psi_g + (1 - \frac{1}{2}|\beta'|^2\mathcal{E}^2)\Psi_r + \bar{\beta}'\mathcal{E} \cdot \Psi_z \\
 \Phi_s &= \Psi_s \\
 \Phi_x &= \frac{1}{2}\sqrt{2}(\Psi_x + \Psi_y) \\
 \Phi_y &= \frac{1}{2}\sqrt{2}(\Psi_x - \Psi_y) \\
 \Phi_z &= \beta\mathcal{E} \cdot \Psi_g - \beta'\mathcal{E} \cdot \Psi_r + (1 - \frac{1}{2}(|\beta|^2 + |\beta'|^2)\mathcal{E}^2)\Psi_z
 \end{aligned} \tag{7.4}$$

where

$$\beta = \frac{p_{15}}{E_5 - E_1}, \quad \beta' = \frac{2p_{35}}{E_3 - E_5}, \quad \beta'' = \bar{\beta} \frac{2p_{35}}{E_3 - E_1}.$$

The initial zero field wave function Ψ_g has the highest spacial symmetry possible in a tetrahedral lattice. To get more insight in the contribution of the six valleys as a function of the applied field, we can write the perturbed ground state wave function Φ_g in the notation of Eq. (7.3) as

$$(1, 1, 1, 1, 1, 1) + (0, 0, 0, 0, -\gamma'', \gamma'')\mathcal{E} - (\gamma, \gamma, \gamma, \gamma, \gamma', \gamma')\mathcal{E}^2,$$

where

$$\gamma = \frac{1}{2}(|\beta|^2 + \beta''\sqrt{2}), \quad \gamma' = \frac{1}{2}(|\beta|^2 - 2\beta''\sqrt{2}), \quad \gamma'' = \bar{\beta}\sqrt{3}$$

and an overall factor $1/\sqrt{6}$ was omitted. From these expressions, we see that the contribution of the valley in the $-\mathbf{z}$ direction increases linearly with the field, while contribution of the opposite valley decreases linearly with the field. This reflects the field-induced dipole moment of the ground state.

The results of this calculation could be made quantitative if the values of the parameters p_5 , p_{15} , and p_{35} were known. This can be done by evaluating the integrals defining these parameters and using e.g. the EMT wave functions from Eq. (7.1). However, due to the strongly oscillating integrands, this is numerically a non-trivial task. Furthermore, the EMT wave functions have a higher symmetry than the lattice, and the value for p_5 obtained in this way is always zero. An estimate for p_5 can only be obtained using more sophisticated approximations for the wave functions. More importantly, the applicability of such results is limited, especially for the $1s$ state, as the effects of valley-orbit interaction are not included in the EMT wave functions.

It is important to note that the energies in Table 7.3 and the eigenstates in Eq. (7.4) are based on symmetry properties only and not on the explicit form of the EMT wave functions. Therefore, these results remain valid, even if valley-orbit interaction and central cell corrections are fully included. Such modifications would only influence the values of the parameters p_5 , p_{15} , and p_{35} .

7.3 Acceptors

Acceptor wave functions can be equally well used for ASE as donors. Recent experiments showing that the coherence time of spins of bound holes is more than 1 ms [23],

even justify the prospective use of acceptor wave functions as qubits. We therefore also briefly outline the properties of silicon acceptors in an electric field, taking the silicon valence band structure into account. The initially threefold degenerate valence band maximum is split by spin orbit interaction, which causes one of the bands to shift downwards by ~ 43 meV [18]. Due to the spin-orbit interaction, spin is not a good quantum number anymore and the bands must be characterized by the total angular momentum, which is $\frac{3}{2}$ for the upper two bands. Due to the half-valued angular momentum, the Bloch wave function at the valence band maximum transforms according to one of the double valued representations of \bar{T}_d , namely Γ_8 . As a result, the total impurity wave functions transform according to representations of the same group. The ground state wave function, as well as the first few excited levels belong to the Γ_8 representation and they are all four-fold degenerate (including spin).

7.3.1 Linear Stark effect

To derive the small-field splitting of acceptors in silicon in an electric field, we use degenerate perturbation theory for each level individually. To that end, the Hamiltonian sub-matrix $\langle \varphi_i | \mathcal{H} | \varphi_j \rangle$ of the level under consideration must be calculated and diagonalized, where the φ_i form a suitable basis for the subspace of that particular level.

As mentioned before, the components of the electric dipole operator $e\mathbf{r}$ transform according to the rows of the Γ_5 representation of \bar{T}_d . Because the anti-symmetrized direct products $\{\Gamma_6 \times \Gamma_6\} = \{\Gamma_7 \times \Gamma_7\} = \Gamma_1$ do not contain Γ_5 , the first order Stark matrix vanishes for levels with Γ_6 or Γ_7 symmetry. Hence, such levels do not experience a linear Stark effect. On the other hand, $\{\Gamma_8 \times \Gamma_8\} = \Gamma_1 + \Gamma_3 + \Gamma_5$ does contain Γ_5 , so that a linear Stark effect is possible for a Γ_8 level*.

The effective linear Stark Hamiltonian[†] for a Γ_8 level is given by [24]

$$[\mathcal{H}]_8^{\text{lin}} = \frac{2}{\sqrt{3}} p_8 (\mathcal{E}_x \{J_y, J_z\} + \mathcal{E}_y \{J_z, J_x\} + \mathcal{E}_z \{J_x, J_y\}),$$

where the parameter p_8 is related to the effective dipole moment of such a state. The J_i ($i = x, y, z$) are matrices of the components of the angular momentum operator with respect to some convenient basis and $\{A, B\} = \frac{1}{2}(AB + BA)$ is the anti-commutator. The eigenvalues of this matrix are given by

$$E_8 \pm |p_8| \mathcal{E},$$

where both eigenvalues occur twice. This is a symmetric splitting of the level, which is independent of the direction of \mathcal{E} . Note that p_8 vanishes within EMT, similar to p_5 before. Estimates of p_8 obtained in literature range from 10^{-2} D [24] to 0.26 D [11].

*Note that a substitutional site in silicon has no inversion symmetry and therefore no definite parity. This is essential for the occurrence of a linear Stark effect in an isolated level.

[†]In contrast to our treatment of donors, we will use the technique of effective Hamiltonians to derive the matrices for acceptor levels.

7.3.2 Quadratic Stark effect

Because $\{\Gamma_6 \times \Gamma_6\} = \{\Gamma_7 \times \Gamma_7\} = \Gamma_1$, the quadratic effective Stark-Hamiltonian for a Γ_6 and Γ_7 level is simply given by

$$\mathcal{H}_{\text{eff,quad}} = a_i \mathcal{E}^2 \hat{I},$$

where \hat{I} is the identity matrix and the a_i ($i = 6, 7$) are phenomenological parameters, that can be expressed in terms of integrals over wave functions. It follows that the Γ_6 and Γ_7 levels experience an isotropic quadratic shift

$$E_i + a_i \mathcal{E}^2,$$

where E_i is the unperturbed energy of a Γ_i level. The two-fold degeneracy due to time reversal symmetry is obviously not removed by the electric field.

The quadratic part of the effective Hamiltonian for a Γ_8 level, such as the ground state, is given by [24]

$$\begin{aligned} [\mathcal{H}]_8^{\text{quad}} &= a_8 \mathcal{E}^2 \hat{I} + b_8 [J_x^2 \mathcal{E}_x^2 + J_y^2 \mathcal{E}_y^2 + J_z^2 \mathcal{E}_z^2 - \frac{1}{3} \mathbf{J}^2] \\ &+ \frac{2}{\sqrt{3}} c_8 [\{J_x, J_y\} \mathcal{E}_x \mathcal{E}_y + \{J_y, J_z\} \mathcal{E}_y \mathcal{E}_z + \{J_z, J_x\} \mathcal{E}_z \mathcal{E}_x], \end{aligned}$$

where a_8 , b_8 and c_8 are again phenomenological parameters. The total Hamiltonian has two distinct eigenvalues

$$a_8 \mathcal{E}^2 \pm [p_8^2 \mathcal{E}^2 + b_8^2 \mathcal{E}^4 + (c_8^2 - 3b_8^2)(\mathcal{E}_y^2 \mathcal{E}_z^2 + \mathcal{E}_x^2 \mathcal{E}_z^2 + \mathcal{E}_x^2 \mathcal{E}_y^2) + 6p_8 c_8 \mathcal{E}_x \mathcal{E}_y \mathcal{E}_z]^{1/2},$$

each of which is still doubly degenerate (due to time reversal symmetry)*. For $\mathcal{E} \parallel \langle 100 \rangle$ this expression reduces to (up to second order in \mathcal{E})

$$E_8 \pm |p_8| \mathcal{E} + a_8 \mathcal{E}^2.$$

For $\mathcal{E} \parallel \langle 111 \rangle$ we find

$$E_8 \pm |p_8| \mathcal{E} + (a_8 \pm \frac{1}{3} \sqrt{3} c_8) \mathcal{E}^2$$

and for $\mathcal{E} \parallel \langle 110 \rangle$ we have

$$E_8 \pm |p_8| \mathcal{E} + a_8 \mathcal{E}^2.$$

The results for $\mathcal{E} \parallel \langle 100 \rangle$ and for $\mathcal{E} \parallel \langle 110 \rangle$ are the same in this approximation, but different in third order.

Obviously, the wave functions of donors and acceptors are very different and this is reflected in their respective electric field behavior. The donor ground state undergoes an isotropic quadratic shift. The acceptor ground state has an isotropic linear splitting, superposed on an anisotropic quadratic shift.

In the spectroscopic measurements of boron acceptors in silicon [10] (mentioned in the introduction), the observed Γ_8 -levels indeed show a quadratic shift. However, the expected level-splitting was not observed, most likely due to limited resolution.

*Note that there is a mistake in the corresponding expression in Ref. 24, where the last term between the square brackets is missing.

Table 7.4 Atomic units for some relevant physical quantities in vacuum and silicon. For silicon the values $\epsilon_s = 11.4$ and $m^* = 0.26$ (appropriate for electrons) were taken. As an example, for lengths in Si we have 1 a.u. \approx 2.3 nm

Quantity	Unit	Value in vacuum	Value in Si
Energy	2Ry	27.2 eV	54 meV
Length	a_0	0.053 nm	2.3 nm
Electric field	2Ry/ ea_0	510 GV/m	24 MV/m
Time	$\hbar/2\text{Ry}$	$2.4 \cdot 10^{-17}$ s	$1.2 \cdot 10^{-14}$ s

7.4 Large electric fields in the SHM

In this section, we will calculate energy levels of an impurity in a semiconductor as a function of electric field in the range from zero to ~ 5 MV/m. This is done within the scaled hydrogen model, where the band structure of the semiconductor is accounted for by a single effective mass and the dielectric constant only.

For this calculation it is convenient to express all quantities in so-called effective atomic units. For instance, energies are expressed in units of twice the effective ionization energy and length in units of the effective Bohr-radius. Conversion of units of relevant quantities for both vacuum and silicon are given in Table 7.4.

In the past, several algorithms have been described in literature to calculate electric field dependence of the energy levels of the hydrogen atom. However, very little results in the range of interest for ASE (fields up to ~ 0.1 a.u. [2]) have been published. Therefore, we found it important to fill this gap by fully presenting the results of our calculation. For this purpose, we used the slightly adapted version of a variational algorithm that not only yields the energy levels, but also their lifetimes [3].

For completeness, we will very briefly outline the main features of this method. The hydrogen Schrödinger equation (including the electric field) in parabolic coordinates can be separated, which allows for high numerical accuracy without too much computational effort. In order to be able to find the energy positions of the resonances as well as their lifetimes, the complex scaling method was applied [25]. Then, for each coordinate the Hamiltonian (including electric field) is expanded with respect to a truncated basis of unperturbed wave functions. This can be done analytically. Finally, the energy levels and lifetimes are obtained by tracking (separately for each level) the eigenvalues of this matrix from zero field in small steps to larger fields.

By using the method described above, we calculated the energies of all states with $n = 1, 2, 3$ for $0 \leq \mathcal{E} \leq 0.2$ a.u. The results for the energy levels are depicted in Fig. 7.3. The levels are labelled by parabolic quantum numbers [26] (n_1, n_2, m) , which are more suitable for hydrogen in an electric field than the more common spherical quantum numbers (n, l, m) . The magnetic quantum number m has the same meaning in both representations. The main quantum number n is related to the parabolic quantum numbers by $n = n_1 + n_2 + |m| + 1$. The electric field lifts all degeneracies except for spin and

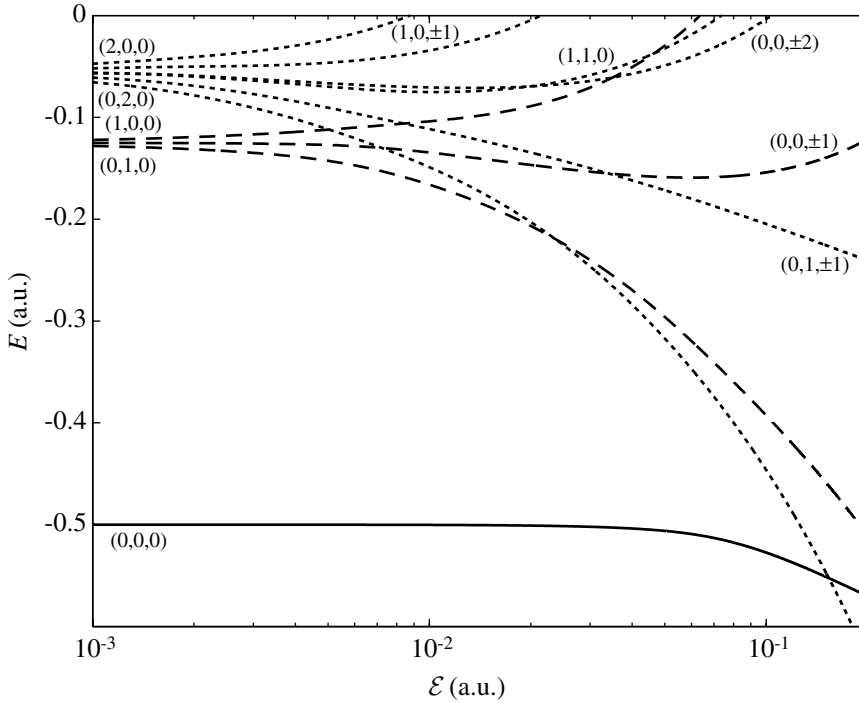


Figure 7.3 Evolution of the lowest lying energy levels ($n = 1, 2, 3$) of a hydrogen-like system versus electric field \mathcal{E} . The levels are labeled with their parabolic quantum numbers (n_1, n_2, m) . For conversion of a.u. to conventional units, see Table 7.4.

$(n_1, n_2, \pm m)$. So (including spin) there are both two-fold degenerate levels ($m = 0$) and fourfold degenerate levels ($m \neq 0$).

Figure 7.3 shows that the ground state ($n = 1$) exhibits a small second order shift downwards. The $n = 2$ -level splits into three levels. Two of them are (for small \mathcal{E}) linearly shifting upwards and downwards. The middle one has no first order shift, consistent with the well known results from perturbation theory [26]. Finally, the ninefold degenerate $n = 3$ -level can be seen to split into six levels. As expected, the effect of the electric field on higher levels is larger, due to their larger spatial extent. At large values of the field, several levels cross each other* and some of them show non-monotonous behavior.

The few results of calculations that can be found in literature (obtained by different methods) and overlap with our results are in very good agreement, both for the ground state [5] and for the first excited state ($m = 1$) [4].

The method we used for our calculations can not only be extended to very large fields, but it also has the advantage of yielding the width of the energy levels. The increasing

*Levels belonging to the same representation of the spatial symmetry group $C_{\infty v}$ can be seen to cross each other in Fig. 7.3. This is however no violation of the non-crossing rule, since for this specific problem there exists an additional constant of motion that is associated with the separability of the Hamiltonian [27].

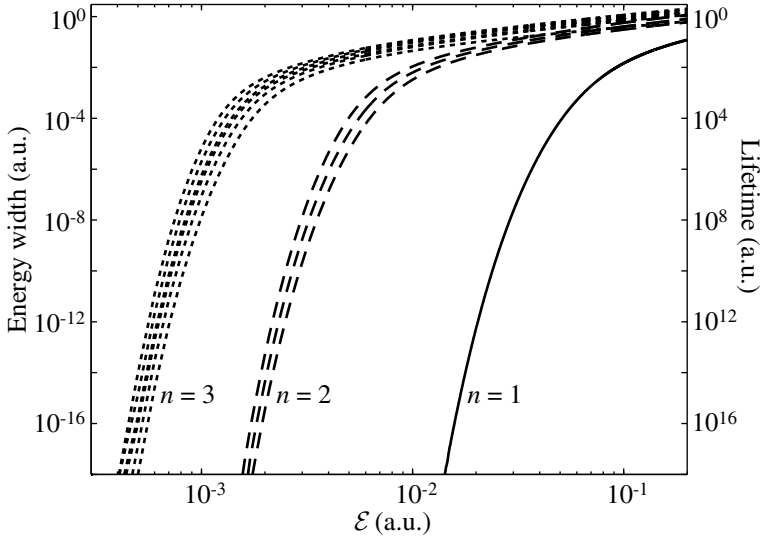


Figure 7.4 Energy width and lifetime of the lowest lying energy levels of hydrogen-like systems ($n = 1, 2, 3$) versus electric field \mathcal{E} . For conversion of a.u. to conventional units, see Table 7.4.

energy width of the hydrogen-like levels in an electric field is the results of the ability of the field to ionize the atom. The finite probability for the carrier to tunnel out of the nucleus' potential well leads to a finite lifetime* of the level. In Fig. 7.4, the evolution of the width of several hydrogen energy levels is depicted. Obviously, the width of all levels is zero at zero field, which is equivalent to an infinitely long lifetime. For any nonzero \mathcal{E} , the lifetimes have a finite value, that decreases monotonously with the field. The stronger the binding energy of a level at zero field, the faster the lifetime decreases when the field increases.

In Figure 7.5, the results of Figure 7.3 and 7.4 are combined into one 'intensity map', where the levels are displayed as normalized Lorentzian line shapes, the width of which is taken from Fig. 7.4. The figure shows clearly that for the realistic electric field $\mathcal{E} = 0.04$ a.u. (about 1 MV/m; see Table 7.4) the energy width of all levels except the ground state is already larger than or comparable to their binding energy. The ground state lifetime is only 10 ns at that field. We also note that for our purpose it is not very useful to extend the calculation to higher fields, as already at $\mathcal{E} = 0.2$ a.u. all levels are very much broadened and strongly overlapping. Although in case of hydrogen atoms in vacuum such large field (0.2 a.u. \approx 100 GV/m) are only realized in astronomy, in semiconductors they can be easily achieved under laboratory conditions (0.2 a.u. \approx 5 MV/m).

Though the SHM oversimplifies the bandstructure, it is in our opinion particularly useful to estimate lifetimes. Fig. 7.4 shows that the lifetimes are primarily a function of

*This lifetime is solely due to the possibility of ionization and is unrelated to (radiative or non-radiative) transitions from an excited level to a lower state.

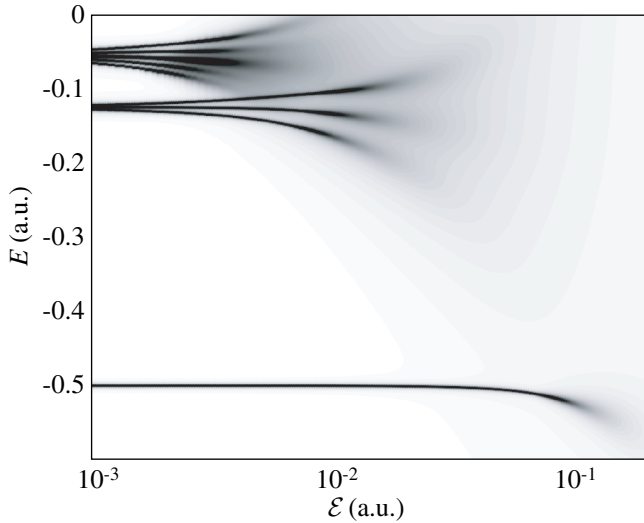


Figure 7.5 Map of the energy levels from Figure 7.3, converted to Lorentzians using the data of Figure 7.4. For conversion of a.u. to conventional units, see Table 7.4.

the zero-field binding energies. Assuming this is still true when the silicon bandstructure is included, interpolation of the results can be expected to provide a good first order approximation of the level's true lifetime. For example, the $n = 1$ value in Fig. 7.4 underestimates the phosphorous donor ground state lifetime, because it is stronger bound than assumed in EMT.

When the electric field is generated by a small local gate, this gate is usually separated from the semiconductor by a potential barrier that is sufficiently high to prevent tunneling. If the distance of the dopant atom to the barrier is not too small, ionization of the dopant atom can still occur in large fields (and the lifetimes discussed before still apply). However, the charge carrier will not be 'lost', but transferred to the potential well created by the biased gate [7].

7.5 Discussion and conclusion

In the preceding sections, we have used two distinct approaches to study the behavior of impurity wave functions in an electric field. The first includes details of the bandstructure, but is only valid for small fields and is somewhat qualitative. From this symmetry-based analysis, we derived the energy level shift and splitting for donors and acceptors in small electric fields, as well as the modification of the donor wave function. Furthermore, the symmetry classification of the resulting levels provides for straightforward prediction of allowed optical transitions.

The second approach, the scaled hydrogen model, is fully quantitative and applicable

up to large fields, but neglects most features of the silicon bandstructure. Still, the SHM offers a manageable and valuable way to describe important phenomena in atomic scale electronics. We presented the energy width and lifetime of the impurity levels in large electric fields, calculated within this framework.

It is possible to combine the two approaches and treat Eq. (7.2) in a way similar to that presented in Section 7.4. Though this is in principle straightforward, the reduced symmetry and lack of separability will make this approach numerically very involved. Furthermore, it is important to note that the direction of the electric field with respect to the valley axis is not the same for all valleys. As an example, for $\mathcal{E} \parallel \mathbf{z}$ the energy levels of F_5 and F_6 are affected in a different way than those of the other four F_μ . If the solutions for the various valley wave functions are known, they can be combined into impurity wave functions using the data in Table 7.2.

Though potentially interesting, such an effort is not likely to yield a good description of the dopant's wave function at high electric fields, despite the tremendous increase of necessary computational power. The reason is the omission of valley orbit interaction, which not only affects the ground state, but also the coupling to excited states. Especially for large fields, the coupling influences the properties *all* energy levels. It has been shown that inter-valley coupling accounts for the splitting of the $1s$ state for P in Si [28]. Inclusion of this effect appears to be a minimum requirement for obtaining accurate quantitative results valid at large fields.

Recently, calculations of a silicon donor in an electric field in the tight binding approach have been presented [29]. This approach seems to be a useful alternative to calculations based on effective mass theory. Given the fact that this method inherently includes the band structure of the semiconductor host, it is striking how similar the results are to calculations based on the SHM [7]. This underlines the power of the SHM in this type of calculations.

In summary, we have calculated the Stark effect of impurities in silicon in two different approaches. Moreover, we discussed the results and the computation methods used in the context of atomic scale electronics and quantum computation.

- [1] B. E. Kane, *Nature* **393**, 133 (1998).
- [2] B. E. Kane, *Fortschr. Phys.* **48**, 1023 (2000).
- [3] G. Alvarez, R. J. Damburg, and H. J. Silverstone, *Phys. Rev. A* **44**, 3060 (1991).
- [4] F. M. Fernández, *Phys. Rev. A* **54**, 1206 (1996).
- [5] I. A. Ivanov, *Phys. Rev. A* **56**, 202 (1997).
- [6] L. M. Kettle, H.-S. Goan, S. C. Smith, C. J. Wellard, L. C. L. Hollenberg, and C. I. Pakes, *Phys. Rev. B* **68**, 075317 (2003).
- [7] G. D. J. Smit, S. Rogge, J. Caro, and T. M. Klapwijk, *Phys. Rev. B* **68**, 193302 (2003).
- [8] A. Fang, Y. C. Chang, and J. R. Tucker, *Phys. Rev. B* **66**, 155331 (2002).
- [9] B. Koiller, X. Hu, and S. D. Sarma, *Phys. Rev. Lett.* **88**, 027903 (2002).
- [10] J. J. White, *Can. J. Phys.* **45**, 2695 (1967).
- [11] A. Köpf and K. Lassmann, *Phys. Rev. Lett.* **69**, 1580 (1992).

- [12] G. M. Guichar, C. Sebenne, F. Proix, and M. Balkanski, Phys. Rev. B **5**, 422 (1972).
- [13] K. Larsson and H. G. Grimmeiss, J. Appl. Phys. **63**, 4524 (1988).
- [14] W. Kohn and J. M. Luttinger, Phys. Rev. **98**, 915 (1955).
- [15] G. Feher, Phys. Rev. **114**, 1219 (1959).
- [16] J. M. Luttinger and W. Kohn, Phys. Rev. **97**, 869 (1955).
- [17] M. Hamermesh, *Group theory and its application to physical problems* (Addison-Wesley, Massachusetts, 1962).
- [18] A. Ramdas and S. Rodriguez, Rep. Prog. Phys. **44**, 1297 (1981).
- [19] R. A. Faulkner, Phys. Rev. **184**, 713 (1969).
- [20] G. F. Koster, J. O. Dimmock, R. G. Wheeler, and H. Satz, *Properties of the thirty-two point groups* (M.I.T. Press, Cambridge, 1963).
- [21] A. K. Ramdas, P. M. Lee, and P. Fisher, Phys. Lett. **7**, 99 (1963).
- [22] B. S. Tsukerblat, *Group theory in chemistry and spectroscopy*, Theoretical chemistry (Academic press Ltd., London, 1994).
- [23] B. Golding and M. I. Dykman (2003), cond-mat/0309147.
- [24] G. L. Bir, E. I. Butikov, and G. E. Pikus, J. Phys. Chem. Solids **24**, 1475 (1963).
- [25] N. Moiseyev, Phys. Rep. **302**, 211 (1998).
- [26] H. A. Bethe and E. E. Salpeter, *Quantum mechanics of one- and two-electron atoms* (Springer-verlag, Berlin, 1957).
- [27] K. Helfrich, Theoret. chim. Acta (Berl.) **24**, 271 (1972).
- [28] A. Balderischi, Phys. Rev. B **1**, 4673 (1970).
- [29] A. S. Martins, R. B. Capaz, and B. Koiller (2003), cond-mat/0308575.



Gate-induced ionization of single dopant atoms

Abstract — Gate-induced wave function manipulation of a single dopant atom is a possible basis of atomic scale electronics. From this perspective, we analyzed the effect of a small nearby gate on a single dopant atom in a semiconductor up to field ionization. The dopant is modeled as a hydrogen-like impurity and the Schrödinger equation is solved by a variational method. We find that—depending on the separation of the dopant and the gate—the electron transfer is either gradual or abrupt, defining two distinctive regimes for the gate-induced ionization process.*

8.1 Introduction

Putting a small gate close to a single impurity is perhaps the most straightforward way to allow for the manipulation of *individual* hydrogen-like wave functions. Apart from the fundamental importance, an ultimate application of single wave function manipulation is found in a Si-based solid state quantum computer [1, 2], in which the nuclear spins of single ^{31}P -dopants are envisioned as qubits. In this proposal, addressing a single qubit by NMR is achieved via the hyperfine interaction of the nuclear spin and its valence electron, which can be tuned by modifying the electron wave function with a nearby gate. In a recent variation of this design [3], the ionization of single dopants by this gate is an essential ingredient.

In this chapter, our aim is to quantitatively investigate the effect of the electric field generated by a local gate on a single neutral dopant atom in a semiconductor, ultimately

*This chapter is based on the following paper: G. D. J. Smit, S. Rogge, J. Caro, and T. M. Klapwijk, Phys. Rev. B **68**, 193302 (2003).

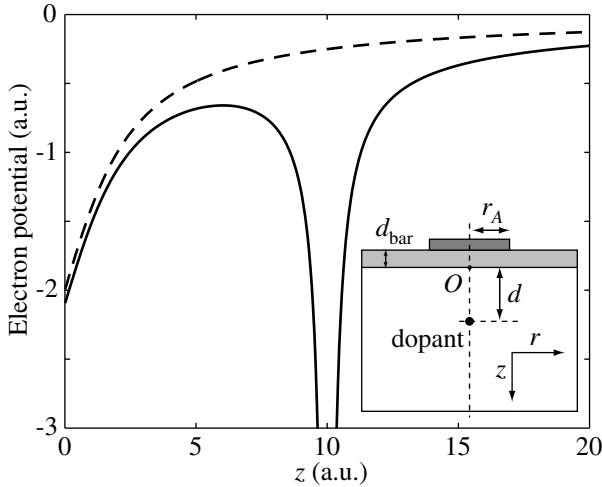


Figure 8.1 The dashed line represents the calculated potential due to the gate at the symmetry axis of the device for $r_A = 2$ a.u. and a gate voltage of 2 a.u. The solid line includes the dopant potential for $d = 10$ a.u. (Note that, e.g., in silicon 1 a.u. ≈ 3 nm for lengths and 1 a.u. ≈ 90 mV for voltages.) The inset shows a schematic of the device layout, indicating the important parameters.

leading to ionization. The response to small fields has been addressed before in the context of quantum computing [4, 5]. In this chapter, the complete ionization process is discussed. Our approach incorporates the computation of time independent ground state wave functions of the system and, subsequently, the estimation of transition probabilities. We conclude that the separation of the dopant and the gate determines the nature of the ionization process. When the dopant resides close to the gate, the electron is gradually pulled away from the dopant when the gate voltage is increased, while for a larger separation the dopant ionizes abruptly at a well-defined gate voltage.

8.2 Model system

Addressing a single dopant requires a small local gate. When a dopant would be ionized by a large gate (e.g., an infinite strip [5]), the electron would be delocalized along the gate. This would be undesirable in applications where (spin-)phase coherence must be kept under control, such as a quantum computer. Therefore, we chose to model the gate as a circular disc, having the additional advantage that the complete system (dopant plus gate) is radially symmetric. The layout of our model system is schematically depicted in the inset of Fig. 8.1. The disc-shaped metallic gate with radius r_A is separated from the semiconductor bulk (relative dielectric constant ϵ_s) by a barrier (relative dielectric constant ϵ_b) of thickness d_{bar} . A dopant is positioned at distance d from the barrier-semiconductor interface and centered with respect to the gate.

At low temperatures, the semiconductor can be considered as a dielectric, due to the absence of free charges. Charges at the barrier-semiconductor interfaces and in the barrier will be neglected. In our calculations, we assume the barrier to be infinitely high and infinitely thin ($d_{\text{bar}} = 0$), which allows us to take advantage of the fact that the potential due to a charged metallic disc in a uniform dielectric medium can be expressed in closed form [6] (we will demonstrate the applicability of our results to a realistic layout). The total potential was obtained by adding a Coulomb potential well due to a positive unit charge in the semiconductor. A cross section of the total electron potential for some typical parameters is shown in Fig. 8.1. Image charge effects at the semiconductor-barrier and the barrier-gate interfaces were neglected.

In our calculations, the dopant atom is described within an effective mass approach: the contribution of the semiconductor bandstructure is accounted for by considering it as an uniform dielectric medium and using an isotropic effective mass. Such a hydrogen-like model is known to provide a good first order description of a dopant atom (although it fails to accurately describe the energy levels [7] and interactions [8]). It is sufficient for our purpose and allows us to capture crucial phenomena and obtain estimates of important parameters. To keep our results general and transparent, physical quantities will be expressed in (effective) atomic units (a.u.)*. To simplify the conversion to conventional units, some values for silicon are given as an example in the caption of Fig. 8.1.

8.3 Solving the Schrödinger equation

The time-independent Hamiltonian of the problem reads (in atomic units)

$$\mathcal{H} = -\frac{1}{2}\nabla^2 - \frac{1}{\sqrt{r^2 + (z-d)^2}} + V_g(r, z),$$

where $V_g(r, z)$ describes the potential landscape in the semiconductor due to the gate and (r, z) are cylinder coordinates as defined in Fig. 8.1 (inset). Approximate ground state wave functions are found by a variational method. As trial wave function we use a linear combination of functions from a fixed and finite set \mathcal{S} , where the weights are used as variational parameters. To this end, we choose \mathcal{S} to contain functions of the form

$$\varphi(r, z) = \exp(-\alpha r^2) \cdot z \exp(-\beta(z-d)^2) \quad (8.1)$$

and

$$\tilde{\varphi}(r, z) = \exp(-\gamma r^2) \cdot z \exp(-\delta z^2), \quad (8.2)$$

where α, β, γ , and δ are constants that will be chosen later. The functions are cylinder-symmetric, motivated by the radial symmetry of the potential and the fact that the ground state is expected to be s -like. To allow for a full description of the ionization process, it is important that \mathcal{S} includes both wave functions of the form (8.1), having large electron

* (Effective) atomic units comprise setting the reduced Planck's constant \hbar , the electron charge e , and the electron effective mass m^* equal to unity. As a result, length is expressed in units of the effective Bohr radius a_0^* and energy is expressed in units of twice the effective ionization energy of the dopant (i.e., twice the effective Rydberg Ry^*). See also Table 7.4.

density at the dopant site, and of the form (8.2), where the electron resides close to the gate.

The functional form of Eq. (8.1) is motivated by the fact that the (exponential) ground state wave function of hydrogen-like atoms can be quite well approximated as a linear combination of Gaussians [9], which are much easier to work with numerically. To make sure that the wave functions vanish at the interface ($z = 0$), it is multiplied by z . The $\varphi(r, z)$ are allowed to become aspherical due to the gate action by choosing different values for α and β . Concerning the form of Eq. (8.2), we note that the potential well caused by the gate can in the radial direction be approximated by a parabola. Consequently, a ground state wave function similar to that of a linear harmonic oscillator is expected and therefore the r -dependent part of $\tilde{\varphi}(r, z)$ is chosen as a Gaussian. The ground state wave function of the triangular shaped well in the z -direction can be approximated as $z \cdot e^{-\zeta z}$ (Ref. 10). Again, we will approximate the exponential by a linear combination of gaussians.

In order to choose concrete values for the constants α , β , γ , and δ , we note that for each positive integer N it is possible to find a set of N real numbers $\{\lambda_i\}_{i=1}^N$, such that a linear combination of $\exp(-\lambda_i r^2)$ optimally approximates the ground state wave function of hydrogen [9]. We will use the values given in Ref. 9, which are, for example, $\{0.101, 0.321, 1.15, 5.06, 33.6\}$ for $N = 5$. In our calculation, we created functions of type (8.1) by taking values for α and β from such a set in all possible N^2 combinations. Functions of type (8.2) were created by choosing values for γ and δ from the same set, after multiplying all elements by the scaling constant $r_A^{-1/2}$ to account for the size of the gate. Proceeding like this, \mathcal{S} contains a total of $2N^2$ functions. It was found that taking $N > 5$ hardly improved the accuracy. Therefore, $N = 5$ was used in all presented results.

Denoting the elements of \mathcal{S} by ψ_n , the variational procedure is now performed by forming the trial wave function

$$\psi(r, z) = \sum_{\psi_n \in \mathcal{S}} c_n \psi_n(r, z)$$

as a linear combination of the ψ_n and minimizing the functional

$$\frac{\langle \psi | \mathcal{H} | \psi \rangle}{\langle \psi | \psi \rangle}$$

with respect to the variational parameters c_n . This minimum is an upper bound to the ground state energy of \mathcal{H} . This variational problem is equivalent to finding the smallest eigenvalue of the generalized matrix eigenvalue problem

$$(\mathbf{H} - E\mathbf{M}) \cdot \mathbf{c} = 0, \quad (8.3)$$

where \mathbf{H} is the Hamiltonian matrix expanded on the ψ_n with elements $H_{ij} = \langle \psi_i | \mathcal{H} | \psi_j \rangle$ and \mathbf{M} is the overlap matrix of the ψ_n defined as $M_{ij} = \langle \psi_i | \psi_j \rangle$. Furthermore, $\mathbf{c} = (c_1, c_2, \dots, c_m)$ and the inner-product $\langle \cdot | \cdot \rangle$ is (as usual) defined as

$$\langle \psi_i | \psi_j \rangle = \int_0^\infty \int_0^\infty \psi_i^*(r, z) \psi_j(r, z) 2\pi r \, dr \, dz.$$

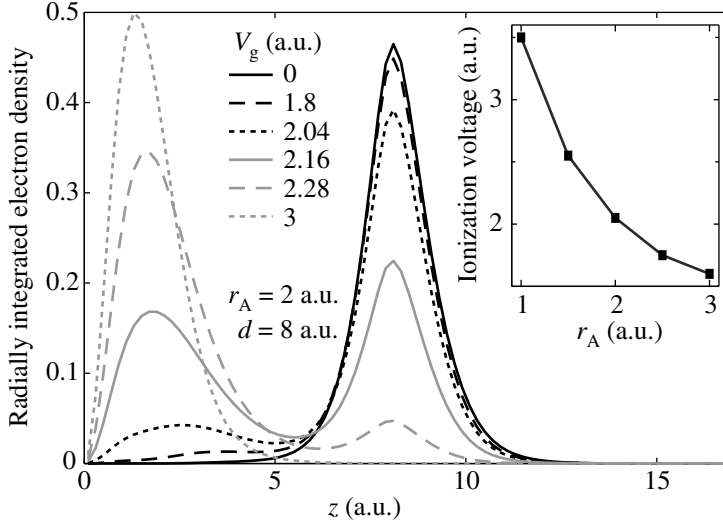


Figure 8.2 The radially integrated probability density of the electron wave function as a function of z for various gate voltages. The inset shows the ionization voltage versus gate radius r_A . (In silicon: 1 a.u. \approx 3 nm and 90 mV, respectively.)

Note that \mathbf{M} would be the unit matrix if \mathcal{S} would be an orthonormal set with respect to $\langle \cdot | \cdot \rangle$. In that case, Eq. (8.3) would reduce to an ordinary eigenvalue problem.

The smallest eigenvalue E_0 of Eq. (8.3) is an upper bound to the ground state energy of the system. When \mathcal{S} is chosen properly, E_0 is a good approximation to the real ground state energy of \mathcal{H} and the corresponding eigenvector \mathbf{c} defines a wave function that is a good approximation of the real ground state wave function.

8.4 Results

Once this wave function is known for several values of the dopant depth d , gate voltage V_g , and gate radius r_A , we will use it to study the ionization process of the dopant. As an example, the radially integrated probability density of the calculated electron wave function (i.e. $\int_0^\infty |\psi(r, z)|^2 2\pi r dr$) is plotted versus z in Fig. 8.2. At zero gate voltage*, the electron occupies the dopant site. For increasing gate voltage, the electron is gradually pulled away from the donor site. Finally, for large enough gate voltage, it resides completely in the newly created potential well at the gate.

An interesting physical quantity is the electron density $|\psi_0(0, d)|^2$ at the dopant site, as derived from the approximated ground state wave function $\psi_0(r, z)$. We will use it as an indication of the position of the electron: when the electron is pulled away from the

*Note that zero gate voltage is defined as the flat-band situation in the semiconductor. Due to interface effects at the gate (that result in band bending), this might correspond to an actual gate voltage that is nonzero.

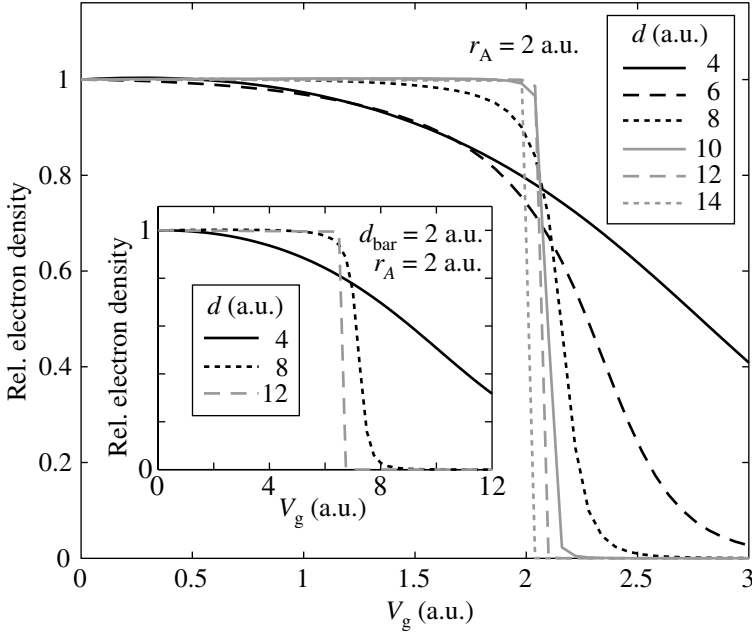


Figure 8.3 The electron density at the dopant site as a function of gate voltage for various dopant depths, showing the process of ionization. All curves are normalized to their value at $V_g = 0$. The transition from a smooth to a step-like behavior is clearly visible at $d \approx 8a_0^*$. The inset shows the corresponding data with a 2 a.u. thick oxide barrier present. The behavior is similar, but occurs at higher gate voltage.

dopant site, this number decreases. Moreover, it is of physical importance because the hyperfine interaction is proportional to this number [11].

The characteristics of the electron transfer from the dopant to the gate with increasing gate voltage depend on the distance d of the dopant under the gate. In Fig. 8.3, the electron density at the dopant site $|\psi_0(0, d)|^2$ (normalized to the value at zero gate voltage) is plotted as a function of gate voltage for several values of d . It can be seen that for small d the electron is transferred gradually from the dopant to the gate, while for larger d an abrupt electron jump occurs, defining an ionization voltage. This can be explained from the fact that for large d , a sufficiently large barrier separates the two potential wells. For small d , the two wells are so strongly coupled that they can be considered as a single well, the position of which is pulled towards the gate with increasing gate voltage.

The calculations were repeated for several gate radii r_A . The inset of Fig. 8.2 shows the ionization voltage for $d = 15$ versus r_A . From the figure it is clear that the voltage gets smaller for larger r_A . The reason for this is that the transfer roughly takes place when the ground state energy of the gate-well drops below that of the dopant-well. When the gate-well is larger, the ground state energy is closer to the bottom of the well and the transfer takes place at lower gate voltage.

8.5 Discussion

In a realistic device, the barrier between the gate and the semiconductor will have a finite thickness (in the most common material systems this will be at least 1 to 2 a.u.). Usually, this barrier does not have the same dielectric constant as the semiconductor and hence it can modify the gate potential considerably. Moreover, the gate must be connected to the outside world by some kind of interconnect. Such an interconnect must be separated from the semiconductor by a much thicker barrier in order to sufficiently screen its potential (see Chapter 3). Therefore, in a realistic device, the gate must be buried in a thick layer of barrier material.

To allow for comparison with the idealized situation in which our calculations were carried out, several calculations were repeated with a realistic barrier present. To that end, we obtained the potential landscape due to the gate by solving the Poisson equation with a finite element method (FEM)*. It was found that for typical realistic parameters (e.g. a SiO₂/Si-system with $\epsilon_s = 12$, $\epsilon_b = 4$, and $d_{\text{bar}} = 2$ a.u.), the potential landscape *in the semiconductor* is qualitatively similar to the situation where the gate is put directly on the semiconductor. As demonstrated in the inset of Fig. 8.3, the same phenomena are observed, but they occur at a higher voltage than in the absence of a barrier. The voltage drop over the barrier can roughly be accounted for by a linear scaling factor that depends on ϵ_b and d_{bar} . Indeed, we find from the FEM-calculations that for the given parameters about 31% of the gate voltage drops in the semiconductor. This number is similar to the observed ratio between the ionization voltages with and without a finite barrier thickness. This justifies the presentation of mainly results obtained with an idealized barrier.

As a final remark in our discussion of the barrier, we note that for any application or measurement of a single dopant device, it is crucial that there are no charge traps present near the dopant. Therefore it is highly desirable to have the barrier epitaxially grown on the semiconductor. A promising candidate is a Si_{1-x}Ge_x-layer as barrier on a Si substrate [2], although the maximum achievable barrier height in this system is only about 100 meV [12].

The presented time-*independent* calculations are not sufficient to predict whether the dopant atom will indeed be ionized when the ground state wave function has a low electron density at the dopant site. In order to complete our analysis, an estimate of the tunnel probability is needed. This is obtained by comparison with the resonance lifetime of a hydrogen atom in an electric field. The typical field strengths considered in the region between the gate and the dopant site are very large (e.g., 0.05–0.5 a.u. for $r_A = 2$, $d = 10$, $V_g = 2$, see Fig. 8.1). Using a calculation of the Stark effect in hydrogen [13] while taking the value of Ry^* for silicon, it is found that the electron lifetime at the dopant site ranges roughly from 0.1 ps to 1 ns. This can be interpreted as the time it takes for the dopant to be ionized when the gate voltage is switched on and justifies our interpretation of Fig. 8.3 as the representation of an ionization process.

*Contrary to the situation without a barrier where the backgate was thought to be at infinity, in the FEM-calculations a backgate had to be put at a finite distance from the barrier, which was chosen as 50 a.u. in the presented calculation. The results depend only weakly on this distance, provided it is much larger than d .

8.6 Application

Our general analysis can be readily applied, as we performed the calculations with parameters that are consistent with the quantum computer design mentioned. First, controlled tuning of the hyperfine interaction by the gate, which is required in Ref. 1, is possible only when d is small enough: from Fig. 8.3 we estimate $d \lesssim 6$ a.u. Switching off the hyperfine interaction, as required in the ‘digital approach’ [3], can only be achieved for large separation between dopant and gate ($d \gtrsim 10$ a.u.). Hence, the dimensions of the device determine in which of both regimes operation takes place. Second, our analysis can be used to estimate the required gate voltage to tune the hyperfine interaction to a certain value (Fig. 8.3). Third, it is found that the required voltage to fully ionize the dopant depends on r_A , but it is nearly independent of d (Fig 8.3).

8.7 Conclusion

In conclusion, we analyzed the wave function manipulation of a semiconductor dopant atom by a small electrostatic gate. We find that two regimes can be distinguished for the ionization process of the dopant. For a dopant-gate separation smaller than $\sim 8a_0^*$ (e.g., ~ 24 nm for P in Si), the electron is gradually pulled out of the Coulomb potential of the dopant. When the dopant resides further away from the gate, the transfer takes place abruptly at a well-defined threshold field. Both regimes are accessible, since, e.g., epitaxial growth techniques allow for sufficiently accurate positioning of the dopant under the gate.

- [1] B. E. Kane, *Nature* **393**, 133 (1998).
- [2] B. E. Kane, *Fortschr. Phys.* **48**, 1023 (2000).
- [3] A. J. Skinner, M. E. Davenport, and B. E. Kane, *Phys. Rev. Lett.* **90**, 087901 (2003).
- [4] A. A. Larionov, L. E. Fedichkin, A. A. Kokin, and K. A. Valiev, *Nanotechnology* **11**, 392 (2000).
- [5] C. I. Pakes, C. J. Wellard, D. N. Jamieson, L. C. L. Hollenberg, S. Praver, A. S. Dzurak, A. R. Hamilton, and R. G. Clark, *Microelectron. J.* **33**, 1053 (2002).
- [6] W. R. Smythe, *Static and Dynamic Electricity* (McGraw-Hill, New York, 1950), 2nd ed.
- [7] A. Ramdas and S. Rodriguez, *Rep. Prog. Phys.* **44**, 1297 (1981).
- [8] B. Koiller, X. Hu, and S. D. Sarma, *Phys. Rev. Lett.* **88**, 027903 (2002).
- [9] S. Huzinaga, *J. Chem. Phys.* **42**, 1293 (1965).
- [10] F. F. Fang and W. E. Howard, *Phys. Rev. Lett.* **16**, 797 (1966).
- [11] H. A. Bethe and E. E. Salpeter, *Quantum mechanics of one- and two-electron atoms* (Springer-verlag, Berlin, 1957).
- [12] C. G. van de Walle, *Properties of silicon germanium and SiGe:Carbon* (IN-SPEC, London, 2000), vol. 24 of *EMIS datareviews series*, pp. 149–157, edited by E. Kasper et al.

[13] I. A. Ivanov, Phys. Rev. A **56**, 202 (1997).



Representations of groups

A.1 Introduction

The Chapters 6 and 7 rely heavily on the theory of group representations. This theory provides a formal way to exploit the spatial symmetry of a system, which is particularly useful when dealing with energy levels of an atom located in a crystal lattice. As a service to the reader, we will present in this appendix a brief review of the most important definitions and theorems that are used in the main text. First, the concepts of groups, representations, and characters of representations are introduced. Then, character tables which are relevant for this thesis are given. Starting from Section A.6, the application to physics is treated.*

A.2 Groups

The notion of an abstract group is given by the following definition.

Definition 1 *A group is a nonempty set G equipped with an operation $*$, having the following properties.*

1. *Closure: If $g_1, g_2 \in G$, then $g_1 * g_2 \in G$.*
2. *Associativity: $g_1 * (g_2 * g_3) = (g_1 * g_2) * g_3$ for any $g_1, g_2, g_3 \in G$.*
3. *Unit element: There is an element $e \in G$ such that $g * e = g = e * g$ for all $g \in G$.*

*An introduction to the theory of groups can be found in many textbooks, for instance Ref. 1. A clean, concise introduction to group representations can be found in Ref. 2. Finally, applications to physics are treated in Ref. 3 and 4.

4. *Inverse:* For each $g \in G$, there is an element of G , commonly denoted by g^{-1} , satisfying $g * g^{-1} = e = g^{-1} * g$.

In practice, when no confusion is possible, $g_1 * g_2$ is often abbreviated as $g_1 g_2$.

To illustrate this definition, we will give some examples of groups.

- The set of only one element e and the group operation defined as $e * e = e$. This is the *trivial group*, the simplest possible group.
- The set of integers \mathbb{Z} with addition as the group operation. The unit element is 0, the inverse of an element $n \in \mathbb{Z}$ is given by $-n$.
- The set of non-zero complex numbers $\mathbb{C} \setminus \{0\}$ with multiplication as the group operation. The unit element is 1, the inverse of an element c is given by $1/c$.
- The set of rotations in the plane around a fixed point O , with composition as the group operation. The unit element is the rotation through 0 rad. The inverse of a rotation over an angle θ is the rotation over an angle $-\theta$.
- The set $GL(V)$ of invertible linear operations on a vector space V (over the field complex numbers) with composition as the group operation. The unit element is the unit operation I , which maps every element of V into itself.

If $g_1, g_2 \in G$ are linked by $g_1 = hg_2h^{-1}$ for some element $h \in G$, then g_1 and g_2 are said to belong to the same *class* of G .

A.2.1 Crystallographic point groups

A group consisting of symmetry operations of a three dimensional body that keep at least one point fixed is called a *point group*. Such groups contain rotation around some axis and, possibly, improper rotations (i.e., proper rotations combined with a mirror reflection in a plane). The point groups associated with crystallographic lattices are called *crystallographic point groups* and there exist exactly 32 of them. They of importance for this thesis, because the symmetry group of an impurity in a crystal lattice is a point group. An important example for this thesis, is the point group T_d (with 24 elements), which is the symmetry group of a substitutional impurity in a tetrahedral lattice, such as the silicon lattice.

A.2.2 Double groups

Half-integer spins have the peculiar property that a rotation through 2π radians does not leave them invariant, though a rotation through 4π does. A point group G expanded with the necessary elements to reflect this special property is called a *double group* and is usually denoted by \bar{G} .

A.3 Representations

Definition 2 A linear representation of a group G in a vector space V is a homomorphism $\Gamma : G \rightarrow \text{GL}(V)$. In other words, with each element $g \in G$ we associate an element $\Gamma(g) \in \text{GL}(V)$ such that

$$\Gamma(g_1 g_2) = \Gamma(g_1) \Gamma(g_2) \text{ for all } g_1, g_2 \in G.$$

As an example, consider the group R_2 of rotations in the plane around O . For each integer m , the mapping $\Gamma_m : R_2 \rightarrow \mathbb{C}$ given by $\Gamma_m(r_\theta) = \exp(im\theta)$ for each $r_\theta \in R_2$ defines a one dimensional representation of R_2 . In particular, for $m = 0$ we get the *trivial representation*, which maps every element of the group into 1.

Two representations Γ and Γ' of the same group G in vector spaces V and V' are said to be *similar* or *isomorphic* if there exists an invertible linear mapping $\tau : V \rightarrow V'$ that converts Γ in Γ' , i.e., that satisfies $\tau \circ \Gamma(g) = \Gamma'(g) \circ \tau$ for all $g \in G$. In particular, each representation of a finite group is isomorphic to a unitary representation.

A.3.1 Reducibility

If $\Gamma : G \rightarrow \text{GL}(V)$ is a representation of G and W is a subspace of V , then W is called *stable* or *invariant* under the action of G if $x \in W$ implies $\Gamma(g)x \in W$ for all $g \in G$. In that case, the restriction Γ^W of Γ to W is also a representation of G and is therefore called a *subrepresentation* of Γ . Furthermore, it can be shown that there exists a complement W' of W in V which is also stable under the action of G , giving rise to a second subrepresentation $\Gamma^{W'}$. Analogous to the notation of the direct sum $V = W \oplus W'$ we write $\Gamma = \Gamma^W + \Gamma^{W'}$. If neither of the two subspaces W and W' has dimension 0, the representation Γ is said to be *reducible*. If such a decomposition is not possible, Γ is said to be *irreducible*. More general, the following theorem holds.

Theorem 3 Every representation can be written as the sum of irreducible representations.

If $\Gamma : G \rightarrow \text{GL}(V)$ is an irreducible representation of G and H is a subgroup of G , then the restriction of Γ to H defines a representation of H . Although the irreducibility of Γ implies that there is no nontrivial subspace of V which is stable under G , there might be one which is stable under H , simply because H contains less elements. Therefore, the restriction of Γ to H can, in general, be reducible.

A.3.2 Product representation

Definition 4 Let $\Gamma_1 : G \rightarrow \text{GL}(V_1)$ and $\Gamma_2 : G \rightarrow \text{GL}(V_2)$ be two linear representations of a group G . Then we define the product representation $\Gamma_p = \Gamma_1 \times \Gamma_2 : G \rightarrow \text{GL}(V_p)$ in the product space $V_p = V_1 \otimes V_2$ by setting for each $g \in G$

$$\Gamma_p(g)(x_1 \otimes x_2) = \Gamma_1(g)x_1 \otimes \Gamma_2(g)x_2$$

for $x_1 \in V_1$ and $x_2 \in V_2$.

Moreover, let τ be the automorphism of $V \otimes V$ defined by $\tau(x_1 \otimes x_2) = x_2 \otimes x_1$. If $\Gamma : G \rightarrow \text{GL}(V)$ is a representation of G , then the subspaces $\text{Sym}^2(V)$ and $\text{Alt}^2(V)$ of $V \otimes V$, consisting of those elements of $V \otimes V$ satisfying $\tau(x) = x$ and $\tau(x) = -x$ respectively, are stable under G . They thus define two representations, which are called the symmetric square $[\Gamma \times \Gamma]$ and the antisymmetric square $\{\Gamma \times \Gamma\}$ of the representation Γ .

A.4 Characters

Definition 5 Let $\Gamma : G \rightarrow \text{GL}(V)$ be a representation of G . The character of Γ is the complex valued function χ_Γ on G defined by

$$\chi_\Gamma(g) = \text{Tr}(\Gamma(g)).$$

The importance of the character lies primarily in the fact that it *characterizes* the representation Γ : two representations are isomorphic if and only if the representations have the same character. The characters of the irreducible representations of a certain group are often collected in a *character table*. Some basic properties of the character are given in the following theorem.

Theorem 6 If χ is the character of a representation Γ of degree n , we have

- $\chi(e) = n$ for the unit element e of G .
- $\chi(g^{-1}) = \chi(g)^*$ for all $g \in G$.
- $\chi(hgh^{-1}) = \chi(g)$ for all $g, h \in G$. This means that χ is a class-function.

Moreover, if χ_1 and χ_2 are the characters of two representations Γ_1 and Γ_2 of G , we also have

- The character of $\Gamma_1 + \Gamma_2$ is $\chi_1 + \chi_2$.
- The character of $\Gamma_1 \times \Gamma_2$ is $\chi_1 \times \chi_2$.
- The character χ_σ of $[\Gamma \times \Gamma]$ is given by $\chi_\sigma(g) = \frac{1}{2}(\chi(g)^2 + \chi(g^2))$.
- The character χ_α of $\{\Gamma \times \Gamma\}$ is given by $\chi_\alpha(g) = \frac{1}{2}(\chi(g)^2 - \chi(g^2))$.

Much can be said about the properties of characters. We restrict ourselves to the most important. To that end, for any two complex valued functions ϕ_1 and ϕ_2 on G put

$$\langle \phi_1 | \phi_2 \rangle = \frac{1}{|G|} \sum_{g \in G} \phi_1(g) \phi_2(g)^*.$$

This defines an inner-product when ϕ_1 and ϕ_2 are characters. Now we can formulate the following very useful orthogonality theorem.

Table A.1 Character table of the double group \bar{T}_d .

Rep.	E	\bar{E}	$8C_3$	$8\bar{C}_3$	$3C_2, 3\bar{C}_2$	$6S_4$	$6\bar{S}_4$	$6\sigma_d, 6\bar{\sigma}_d$
Γ_1	1	1	1	1	1	1	1	1
Γ_2	1	1	1	1	1	-1	-1	-1
Γ_3	2	2	-1	-1	2	0	0	0
Γ_4	3	3	0	0	-1	1	1	-1
Γ_5	3	3	0	0	-1	-1	-1	1
Γ_6	2	-2	1	-1	0	$-\sqrt{2}$	$\sqrt{2}$	0
Γ_7	2	-2	1	-1	0	$\sqrt{2}$	$-\sqrt{2}$	0
Γ_8	4	-4	-1	1	0	0	0	0

Theorem 7 If χ is the character of an irreducible representation, then $\langle \chi | \chi \rangle = 1$, that is, χ is ‘normalized’. Moreover, if χ_1 and χ_2 are the characters of two non-isomorphic irreducible representations, then $\langle \chi_1 | \chi_2 \rangle = 0$, that is, χ_1 and χ_2 are ‘orthogonal’.

The practical importance of this theorem lies in the fact that if the representation Γ with character χ decomposes into irreducible representations as $\Gamma_1 + \dots + \Gamma_k$ with characters χ_1, \dots, χ_k and Γ_0 is an irreducible representation with character χ_0 , then $m = \langle \chi_0 | \chi \rangle$ is the number of representations among the $\Gamma_1, \dots, \Gamma_k$ that is isomorphic to χ_0 . In other words, Γ_0 occurs m times in Γ .

Because the characters of all irreducible representations of the 32 point groups are known [5], this makes it straightforward to decompose any representation of a point group into its irreducible components.

A.5 Relevant character tables

In this section, we give as a service to the reader the character tables of various symmetry groups, relevant for this thesis. Table A.1 refers to the lattice symmetry group \bar{T}_d . Depending on the direction of the magnetic field, it reduces to one of the groups S_4 , C_3 or C_{1h} , the character tables of which are given in Table A.2 and A.3. In an electric field, it reduces to one of the groups C_{2v} , C_{3v} or C_s , the character tables of which are given in Table A.4. Finally, the tables of the continuous groups $D_{\infty h}$ and $C_{\infty v}$ are given in Table A.5.

A.6 Representations and wave functions

To make the connection with physics, let G be a group of operations that act on the spatial coordinate \mathbf{r} , for instance a point group. If ψ is a function, we can associate with each element $g \in G$ a linear operator O_g defined by $O_g \psi(\mathbf{r}) = \psi(g^{-1} \mathbf{r})$. If $O_g \psi$ is identical to ψ , the function ψ is said to be invariant under the transformation g . Similarly, an

Table A.2 Character table for the double group \bar{S}_4 ($\omega = e^{i\pi/4}$), relevant for a dopant atom in a magnetic field along the $\langle 100 \rangle$ direction.

Rep.	E	\bar{E}	C_2	\bar{C}_2	S_4	S_4^{-1}	\bar{S}_4	\bar{S}_4^{-1}
Γ_1	1	1	1	1	1	1	1	1
Γ_2	1	1	1	1	-1	-1	-1	-1
Γ_3	1	1	-1	-1	$-i$	i	$-i$	i
Γ_4	1	1	-1	-1	i	$-i$	i	$-i$
Γ_5	1	-1	$-i$	i	$-\omega$	ω^3	ω	$-\omega^3$
Γ_6	1	-1	i	$-i$	ω^3	$-\omega$	$-\omega^3$	ω
Γ_7	1	-1	$-i$	i	ω	$-\omega^3$	$-\omega$	ω^3
Γ_8	1	-1	i	$-i$	$-\omega^3$	ω	ω^3	$-\omega$

Table A.3 Character table for the double groups \bar{C}_3 (left; $\omega = e^{i\pi/3}$) and \bar{C}_{1h} (right), relevant for a dopant atom in a magnetic field along the $\langle 111 \rangle$ and $\langle 110 \rangle$ direction, respectively.

Rep.	E	\bar{E}	C_3	C_3^{-1}	\bar{C}_3	\bar{C}_3^{-1}
Γ_1	1	1	1	1	1	1
Γ_2	1	1	$-\omega$	ω^2	$-\omega$	ω^2
Γ_3	1	1	ω^2	$-\omega$	ω^2	$-\omega$
Γ_4	1	-1	$-\omega^2$	ω	ω^2	$-\omega$
Γ_5	1	-1	ω	$-\omega^2$	$-\omega$	ω^2
Γ_6	1	-1	-1	-1	1	1

Rep.	E	\bar{E}	σ_h	$\bar{\sigma}_h$
Γ_1	1	1	1	1
Γ_2	1	1	-1	-1
Γ_3	1	-1	$-i$	i
Γ_4	1	-1	i	$-i$

Table A.4 Character tables of the single valued irreducible representations of the point groups C_{2v} , C_{3v} , and C_s , relevant for a dopant atom in an electric field along the $\langle 100 \rangle$, $\langle 111 \rangle$ and $\langle 110 \rangle$ direction, respectively.

C_{2v}	E	C_2	σ_v	σ'_v
Γ_1	1	1	1	1
Γ_2	1	-1	1	-1
Γ_3	1	1	-1	-1
Γ_4	1	-1	-1	1

C_{3v}	E	$2C_3$	$3\sigma_v$
Γ_1	1	1	1
Γ_2	1	1	-1
Γ_3	2	-1	0

C_s	E	σ
Γ_1	1	1
Γ_2	1	-1

Table A.5 Character table of the groups $D_{\infty h}$ and $C_{\infty v}$ (upper left part). These continuous groups have four (two for $C_{\infty v}$) one-dimensional representation and an infinite number of two-dimensional representations. Here m is a positive integer.

	E	$2C_{\infty}^{\varphi}$	$\infty\sigma_v$	i	$2S_{\infty}^{\varphi}$	∞C_2
Γ_g^+	1	1	1	1	1	1
Γ_g^-	1	1	-1	1	1	-1
Γ_g^m	2	$2 \cos m\varphi$	0	2	$2 \cos m\varphi$	0
Γ_u^+	1	1	1	-1	-1	-1
Γ_u^-	1	1	-1	-1	-1	1
Γ_u^m	2	$2 \cos m\varphi$	0	-2	$-2 \cos m\varphi$	0

operator $\mathcal{H}(\mathbf{r})$ acting on the function ψ is said to be invariant under g if $O_g \mathcal{H} O_g^{-1}$ is identical to \mathcal{H} (in other words, \mathcal{H} and O_g commute).

Consider the energy levels and wave functions of an isolated atom perturbed by a crystalline environment. Then, the electrostatic potential felt by an electron bound to this impurity is invariant under operation O_g of the crystal point group G . Because the kinetic energy operator is invariant under any rotation or reflection, the full Hamiltonian \mathcal{H} of this problem is invariant under transformations of G .

If $\{\psi_i\}$ is a set of n linearly independent eigenfunctions of this Hamiltonian \mathcal{H} belonging to the same eigenvalue E , then the $O_g \psi_i$ are also eigenfunctions of \mathcal{H} . Hence, they can be expressed as a linear combination of the original $\{\psi_i\}$, namely

$$O_g \psi_i = \sum_{j=1}^n M_{ij}(g) \psi_j.$$

Moreover, it can be shown that the matrices $M(g)$ thus defined satisfy $M(g_1 g_2) = M(g_1) M(g_2)$. In other words, the $M(g)$ form an n -dimensional linear representation of G .

After reduction of such a representation into its irreducible components, it is useful to classify the corresponding basis functions as $\psi_i^{(\mu)}$, meaning that this is the i th basis function of the μ th irreducible representation of G . This is nothing else then assigning the quantum numbers i and μ to describe the function's behavior under operations of G^* .

Theorem 8 *The eigenfunctions of each degenerate energy level of a Hamiltonian \mathcal{H} provide a basis for a representation of the symmetry group of \mathcal{H} .*

In our situation, G is a crystallographic point group and therefore all the irreducible representations are known. This makes it possible to classify the energy levels of \mathcal{H} by labeling them with the corresponding irreducible representations. If the representation of

*This is completely analogous to the quantum numbers l and m which characterize the behavior of the spherical harmonics $Y_m^l(\theta, \varphi)$ under rotations and inversion by assigning it to the m th row of the l th irreducible representation.

an energy level is irreducible, no perturbation that preserves the symmetry of the Hamiltonian can lift the degeneracy. If, on the other hand, a perturbation is applied that does reduce the symmetry, it is straightforward to derive how the representation is reduced under the new symmetry group of \mathcal{H} . The degrees of the new irreducible representations give the degeneracies of the new levels that emerge from the original level.

A.7 Matrix elements

It is an easily proven fact that the integral of a function of odd parity vanishes. The theory of representations of groups extends this argument and fully exploits the symmetry properties of wave functions and operators in the calculation of matrix elements.

Every group G has at least one irreducible representation, namely the trivial representation, which is commonly denoted by Γ_1 . A function belonging to Γ_1 is invariant under all group transformations. It can be shown that the integral of a function $\psi_i^{(\mu)}$ (belonging to the i th row of representation μ) vanishes, if it does not belong to Γ_1 ($\mu \neq 1$).

If ψ and φ transform according to the representations Γ and Γ' , respectively, their product $\psi\varphi$ transforms according to the product representation $\Gamma \times \Gamma'$. If $\Gamma \times \Gamma'$ can be reduced to $\Gamma_1 + \dots + \Gamma_k$, this means that $\psi\varphi$ can be written as a linear combination of functions ϕ_i , where each ϕ_i belongs to Γ_i .

For the following theorem, we recall that if ψ and φ are functions in a certain Hilbert space, then $\langle \psi | \varphi \rangle = \int \psi(\mathbf{r})\varphi(\mathbf{r})^* d\mathbf{r}$ defines an inner-product on this space.

Theorem 9 1. $\langle \psi_i^{(\mu)} | \varphi_j^{(\nu)} \rangle = 0$ if $\Gamma_\mu \times \Gamma_\nu$ does not contain Γ_1 .

2. $\langle \psi_i^{(\mu)} | \varphi_j^{(\nu)} \rangle = 0$ if $\mu \neq \nu$ or $i \neq j$.

3. Let \mathcal{A} be an operator that transforms according to the representation Γ_ρ . Then $\langle \psi_i^{(\mu)} | \mathcal{A} | \varphi_j^{(\nu)} \rangle = 0$ if $\Gamma_\mu \times \Gamma_\nu$ does not contain Γ_ρ .

The above is very useful when calculating matrix elements of a certain operator, as it allows for easy identification of most vanishing matrix elements, just by using the symmetry properties of the system.

Care must be taken when $\mu = \nu$ and the $\psi_i^{(\mu)}$ and $\varphi_j^{(\mu)}$ are the same set of functions, because then the products $\psi_i^{(\mu)}\varphi_j^{(\mu)}$ are not linearly independent. This occurs when calculating the coupling of states within one level. In this situation, the product $\Gamma_\mu \times \Gamma_\nu$ in Theorem 9 must be replaced by the symmetrized product $[\Gamma_\mu \times \Gamma_\mu]$.

Theorem 10 (Wigner-Eckart) Let μ and ν be fixed and let the operator \mathcal{A} belong to the representation Γ_ρ . Then the matrix A with elements $A_{ij} = \langle \psi_i^{(\mu)} | \mathcal{A} | \varphi_j^{(\nu)} \rangle$ can be written as $A = aB$, where a is a numeric constant and B is a matrix that only depends on the representations Γ_μ , Γ_ν , and Γ_ρ . The elements of B are called Clebsch–Gordon coefficients of G .

This theorem forms the cornerstone of the ‘effective Hamiltonian’ method used in Chapter 6 and 7. It is very powerful, as it states that all matrix elements A_{ij} can be

calculated up to a single constant a , by only knowing the symmetry properties of the system. All other properties of the wave functions and operator are contained in a . The Clebsch–Gordon coefficients B_{ij} can be obtained from, e.g., the coupling constants listed in Ref. 5.

- [1] T. W. Hungerford, *Abstract algebra: An introduction* (Saunders college publishing, 1990), 2nd ed.
- [2] J.-P. Serre, *Linear representations of finite groups*, vol. 42 of *Graduate texts in mathematics* (Springer Verlag, 1993), 4th ed.
- [3] B. S. Tsukerblat, *Group theory in chemistry and spectroscopy*, Theoretical chemistry (Academic press Ltd., London, 1994).
- [4] M. Hamermesh, *Group theory and its application to physical problems* (Addison-Wesley, Massachusetts, 1962).
- [5] G. F. Koster, J. O. Dimmock, R. G. Wheeler, and H. Satz, *Properties of the thirty-two point groups* (M.I.T. Press, Cambridge, 1963).

Summary

.....

Atomic-scale electronics in semiconductors _____

A dopant atom in a semiconductor, which can be considered as the solid state analogue of a hydrogen atom, has a Bohr radius of several nanometers. Because this length scale is close to being accessible by modern nanolithography, detection and control of charge and spin in a semiconductor down to the level of individual dopant atoms is within reach and provides the unique opportunity to study, manipulate, and utilize a single atom's wave function. These issues are studied within the context of *Atomic Scale Electronics* and this thesis contains several experimental and theoretical results which contribute to this emerging field.

In this thesis, focus is put on scaling of metal-semiconductor diodes, effects of the discreteness of doping on the electrical properties of small diodes, resonant tunneling spectroscopy of single dopant atoms, and the effect of magnetic and electric fields on the electronic state of dopant atoms.

The behavior of conventional devices may change drastically when decreasing their size below a certain length scale. From this perspective, we have performed electrical transport measurements across epitaxial defect-free nanometer-sized Schottky diodes. These were formed by self-assembled CoSi_2 -islands on Si(111) and contacted with the tip of a scanning tunneling microscope (STM). An ultra-high vacuum system is required for the preparation and measurements of this delicate experimental system. Greatly enhanced conductance was observed in diodes, the size of which was small compared to the Debye length in the semiconductor. The observed behavior can be understood qualitatively from a model that predicts a decreased barrier width for smaller diodes. This causes enhanced tunneling leading to an increase in conductance (per unit area). From an extension of this model we also find that—next to the actual diode size—the interconnects in micro-fabricated devices play an important role in determining the conductance of a diode.

The discreteness of doping is another important factor which influences the *IV*-characteristics of small devices. In fact, dopant-induced fluctuations in the device characteristics are viewed as one of the fundamental limits in scaling down the size of MOSFETs. We find that on highly doped substrates, individual dopant atoms even dominate the transport characteristics of our nanometer sized devices. In room temperature measurements, the scatter in the device-to-device conductance increases towards smaller device sizes. Moreover, in low-temperature measurements pronounced features are observed, which are attributed to resonant tunneling through electronic states of individual dopant atoms. For a statistical analysis of the room temperature results, the observed scatter in the mea-

surements was interpreted as resulting from fluctuations in the Schottky barrier height due to randomly distributed individual dopant atoms in the space charge region.

The ability to observe the energy levels of single dopant atoms is essential for experimental studies of individual wave functions in a semiconductor. Resonant tunneling spectroscopy (RTS) is a promising method for this purpose. Therefore, as a first step towards RTS of single dopant atoms, RTS-measurements were performed on large silicon tunneling devices containing a δ -doped barrier. The effectiveness of this technique is demonstrated by the observed resonance in the differential conductance, which was identified as arising from tunneling through the B^+ -state of boron atoms in the δ -layer. Furthermore, preliminary results in a fabrication method for nano-devices approaching the size regime necessary for the observation of single dopants demonstrate the feasibility of an STM-based measurement method.

The Si: B^+ -state, a boron impurity in silicon binding an extra hole, has only one bound state, the nature of which was not well-established. Therefore, the magnetic-field behavior of isolated double acceptors in a tetrahedral lattice was analyzed using group theory. This resulted in a prediction of the qualitative features of the magnetic field response for each of the possible symmetries of a double acceptor. Comparison of the outcomes to the RTS-measurements allowed for identification of the symmetry of the B^+ -state.

The most straightforward means to address an individual impurity is manipulation of its wave function with a gate. As a first approach to address this problem theoretically, the effect of a homogeneous electric field on the energy levels of shallow donors and acceptors in silicon was studied, taking the bandstructure into account. Furthermore, a description as hydrogen-like impurities was used for accurate computation of energy levels and lifetimes up to large (several MV/m) electric fields. We find that, despite its simplicity, this ‘scaled hydrogen model’ turns out to be a useful and valuable description of a dopant atom in silicon.

Therefore, the scaled hydrogen model was used in a realistic device geometry, in which a small nearby gate influences a single dopant atom. The effect of this electric field was analyzed up to field ionization. It was found that—depending on the separation of the dopant and the gate—the electron transfer is either gradual or abrupt, defining two distinctive regimes for the gate-induced ionization process. This knowledge is particularly important for the development of a dopant-atom based quantum computer.

In conclusion, this thesis deals with several basic but essential topics in the field of *Atomic Scale Electronics*. Taking our results and the overall progress in this field into account, it is reasonable to expect that within a few years time both the controlled manipulation of a single dopant atom’s wave function and tuning of the strength of the interaction between two dopant atoms will have been realized experimentally.

Gert-Jan Smit

Elektronica op atomaire schaal in halfgeleiders _____

Een doteringsatoom in een halfgeleider—dat kan worden beschouwd als het vastestofanalogon van een waterstofatoom—heeft een Bohr-straal van verscheidene nanome-

ters. Omdat het met moderne nanolithografie vrijwel mogelijk is toegang te krijgen tot deze schaal, komt het detecteren en beïnvloeden van lading en spin in een halfgeleider tot op het niveau van individuele doteringsatomen binnen handbereik. Dit geeft de bijzondere mogelijkheid om de golf functie van een individueel atoom te bestuderen, te manipuleren en er gebruik van te maken. Deze zaken worden bestudeerd binnen de context van *Elektronica op Atomaire Schaal* en dit proefschrift bevat een aantal experimentele en theoretische resultaten die bijdragen aan dit onderzoeksgebied-in- wording.

In dit proefschrift ligt de nadruk op de schalingseigenschappen van metaal-halfgeleider diodes, de effecten van het discrete karakter van dotering op de elektrische eigenschappen van diodes, resonante-tunnelspectroscopie van individuele doteringsatomen en het effect van magnetische en elektrische velden op de elektronische toestand van doteringsatomen.

Het gedrag van conventionele elektronische devices kan drastisch veranderen wanneer hun afmeting kleiner wordt dan een zekere karakteristieke lengte. Om dit te onderzoeken hebben we elektrisch-transportmetingen verricht in epitaxiale, defect-vrije Schottky diodes van nanometer-afmetingen. Deze bestonden uit zelf-gevormde CoSi_2 -eilandjes op Si(111), waarmee de tip van een scanning tunneling microscoop (STM) contact maakte. Voor de preparatie van en metingen aan dit delicate experimentele systeem is een ultrahog vacuüm systeem vereist. In diodes waarvan de afmeting klein was vergeleken met de Debye-lengte in de halfgeleider werd een sterk vergrote geleiding waargenomen. Dit waargenomen gedrag kan kwalitatief worden begrepen vanuit een model dat voorspelt dat de barrière dikte afneemt naarmate de diodes kleiner worden. Dit veroorzaakt een toegenomen tunnelstroom, waardoor door de geleiding (per oppervlakte eenheid) groter wordt. Een uitbreiding van dit model voorspelt ook dat—naast de eigenlijke afmeting van de diode—de interconnects in gemicrofabriceerde devices een belangrijke rol spelen in het bepalen van de geleiding van een diode.

Het discrete karakter van dotering is een andere belangrijke factor die de *IV*-karakteristiek van een klein device beïnvloedt. Fluctuaties in de eigenschappen van devices als gevolg van dotering worden zelfs gezien als één van de fundamentele limieten voor het alsmaar kleiner maken van MOSFETs. Uit metingen op zwaar-gedoteerde substraten blijkt dat individuele doteringsatomen de transport-eigenschappen van onze nanometer-grote diodes zelfs domineren. In metingen bij kamertemperatuur neemt de spreiding (van device tot device) in de geleiding toe naarmate de diodes kleiner worden. Daarnaast zijn in metingen bij lage temperatuur sterke karakteristieken waargenomen die we toeschrijven aan resonante tunneling door de elektronische toestand van individuele doterings atomen. Voor een statistische analyse van de resultaten bij kamertemperatuur interpreteren we de waargenomen spreiding in de metingen als het gevolg van fluctuaties in de hoogte van de Schottky-barrière. Deze fluctuaties worden op hun beurt veroorzaakt door willekeurig verdeelde individuele doteringsatomen in het ruimte-ladingsgebied.

Het vermogen om energie niveaus van individuele doteringsatomen waar te nemen is essentieel voor experimentele studies aan individuele golf functies in een halfgeleider. Resonante-tunneling spectroscopie (RTS) is een veelbelovende methode voor dit doel. Als een eerste stap op weg naar RTS van enkele doteringsatomen zijn daarom RTS-metingen verricht aan grote silicium devices met een tunnel-barrière die een δ -doteringslaag bevat. De effectiviteit van deze techniek wordt aangetoond door de re-

sonantie die we waarnamen in de differentiële geleiding. We hebben vastgesteld dat deze resonantie het gevolg is van tunnels door de B^+ -toestand van boor-atomen in de δ -laag. Verder laten voorlopige resultaten van een fabricage methode voor nano-devices (die de noodzakelijke afmetingen benaderen voor het waarnemen van individuele doterings atomen) zien dat een op STM gebaseerde meetmethode haalbaar is.

De $Si:B^+$ toestand, een boor-verontreiniging in silicium die een extra gat bindt, heeft slechts één gebonden toestand, waarvan de aard (nog) niet vaststaat. Daarom is het magnetisch-veld gedrag van geïsoleerde dubbel-acceptoren in een diamantrooster geanalyseerd met behulp van groepentheorie. Hieruit volgde een voorspelling van de kwalitatieve kenmerken van de respons op een magnetisch veld voor elk van de mogelijke symmetrieën van een dubbel-acceptor. Vergelijking van de uitkomsten met de metingen maakte het mogelijk de aard van de B^+ -toestand vast te stellen.

De meest voor de hand liggende manier om een individueel doteringsatoom aan te spreken is manipulatie van zijn golf functie met een gate. In een eerste, theoretische benadering van dit probleem is het effect van een homogeen elektrisch veld op de energie niveaus van ondiepe donoren en acceptoren in silicium bestudeerd, waarbij de bandenstructuur is meegenomen. Daarnaast is een waterstof-achtige beschrijving van doteringsatomen gebruikt voor een nauwkeurige berekening van de energie niveaus en levensduren tot grote (enkele MV/m) elektrische velden. We vinden dat—ondanks haar eenvoud—dit ‘geschaalde-waterstofmodel’ een nuttige en waardevolle beschrijving van een doteringsatoom in silicium blijkt te zijn.

Om die reden is het geschaalde-waterstofmodel gebruikt in een realistische device-geometrie, waarin een kleine, dichtbij geplaatste gate een enkel doteringsatoom beïnvloedt. Het effect van dit elektrisch veld is geanalyseerd tot aan het optreden van veld-ionisatie. Het bleek dat—afhankelijk van de afstand tussen het doteringsatoom en de gate—de overdracht van het electron geleidelijk of abrupt plaatsvindt, waarmee twee verschillende regimes gedefinieerd worden voor het gate-geïnduceerde ionisatie proces. Deze kennis is vooral belangrijk voor de ontwikkeling van een op doteringsatomen gebaseerde kwantum-computer.

Concluderend: dit proefschrift behandelt verscheidene basale maar essentiële onderwerpen binnen het vakgebied van de *Elektronica op Atomaire Schaal*. Kijkend naar onze resultaten en de algehele vooruitgang in dit vakgebied lijkt het redelijk te verwachten dat binnen enkele jaren zowel de gecontroleerde manipulatie van de golf functie van een individueel doteringsatoom als het instellen van de sterkte van de interactie tussen twee doteringsatomen experimenteel gerealiseerd zullen zijn.

Gert-Jan Smit

List of publications

Publications related to this thesis

- *Stark effect of shallow impurities in Si*
G. D. J. Smit, S. Rogge, J. Caro, T. M. Klapwijk, cond-mat/0310492 (2003), submitted. [Chapter 7]
- *Direct observation by resonant tunneling of the B^+ level in a delta-doped silicon barrier*
J. Caro, I. D. Vink, G. D. J. Smit, S. Rogge, T. M. Klapwijk, R. Loo, and M. Caymax, cond-mat/0309139 (2003), submitted. [Chapter 5]
- *Group-theoretical analysis of double acceptors in a magnetic field: Identification of the $Si:B^+$ ground state*
G. D. J. Smit, S. Rogge, J. Caro, T. M. Klapwijk, condmat/0309136 (2003), to be published in Phys. Rev. B. [Chapter 6]
- *Conductance distribution in nanometer-sized semiconductor devices due to dopant statistics*
G. D. J. Smit, S. Rogge, J. Caro, T. M. Klapwijk, cond-mat/0309137 (2003), to be published in Phys. Rev. B. [Chapter 4]
- *Gate-induced ionization of single dopant atoms*
G. D. J. Smit, S. Rogge, J. Caro, T. M. Klapwijk, *Phys. Rev. B* **68**(19), 193302-1-4 (2003). [Chapter 8]
- *Scaling of nano-Schottky-diodes*
G. D. J. Smit, S. Rogge, T. M. Klapwijk, *Appl. Phys. Lett.* **81**(20), 3852-4 (2002). [Chapter 2]
- *Scaling of micro-fabricated nanometer-sized Schottky diodes*
G. D. J. Smit, M. G. Flokstra, S. Rogge, T. M. Klapwijk, *Microelectron. Eng.* **64**(1-4), 429-33 (2002). [Chapter 3]
- *Enhanced tunneling across nanometer-scale metal-semiconductor interfaces*
G. D. J. Smit, S. Rogge, T. M. Klapwijk, *Appl. Phys. Lett.* **80**(14), 2568-70 (2002). [Chapter 2]

Publications not related to this thesis

- *Phonon generation by carrier recombination in a-Si:H*
M. van der Voort, G. D. J. Smit, A. V. Akimov, J. I. Dijkhuis, *Physica B* **263**, 283-5 (1999).

- *Decay of nonequilibrium phonons in nanocrystalline silicon*
M. van der Voort, G. D. J. Smit, A. V. Akimov, J. I. Dijkhuis, N. A. Feoktistov,
A. A. Kaplyanskii, A. B. Pevtsov, *Physica B* **263**, 473–5 (1999).

Dankwoord

Met het gereedkomen van dit proefschrift is na ruim vier en een half jaar mijn promotietraject vrijwel afgesloten. Het schrijven van dit boekje en vooral het voltooiën van het daaraan ten grondslag liggende onderzoek was echter nooit gelukt zonder de hulp, aanwezigheid en ondersteuning van vele anderen, die ik hier wil bedanken.

Mijn onderzoek vond plaats in de vakgroep Nanofysica onder leiding van mijn promotor Teun Klapwijk. Weliswaar op enige afstand, maar daarom niet minder belangrijk. Zijn vaardigheid om het grote overzicht te bewaren, om een boodschap goed te verpakken en uit te dragen én zijn kennis van de wereld der wetenschap (inclusief geschiedenis en filosofie) en daarbuiten waren voor mij erg belangrijk, nuttig en inspirerend.

Buitengewoon veel dank ben ik verschuldigd aan Sven Rogge. Als mijn directe begeleider was hij mijn primaire vraagbaak op vrijwel alle terreinen. Altijd kon ik bij hem binnenlopen, of het nu om een natuurkundige vraag ging, een computer-probleem of een gezellig praatje. Dankzij zijn grote experimentele kennis en vaardigheid heb ik in vier jaar heel veel kunnen leren. Ook bij het schrijven van artikelen en het bepalen van de richting van mijn onderzoek heeft hij een onmisbare rol gespeeld.

Bart Geerligts wil ik bedanken voor het vertrouwen dat hij in me had door mij als promovendus aan te nemen en voor zijn enthousiaste begeleiding tijdens de start van mijn project.

De laatste twee jaar werkte ik binnen de subgroep ‘Atomic-scale electronics’, waarvan het belang goed tot uitdrukking komt in de titel van dit boekje. In die context wil ik eerst Jaap Caro bedanken voor de vele nuttige discussies die we gehad hebben. Dankzij zijn kritische en minutieuze hulp kwamen verscheidene onvolkomenheden in mijn werk en schrijfsels aan het licht en konden zo verholpen worden. Machiel Flokstra wil ik bedanken voor zijn bijdrage aan het nano-Schottky-diode-project. De EVO-studenten Marc-Jan den Boer (later ook afstudeerder), Jan Manschot en Krijn Wielinga wil ik bedanken voor hun inzet bij verschillende projecten. David Bakker, Michel van Putten en Irene Vink (van de ‘Irene-devices’) legden de experimentele basis voor onze subgroep en daarmee voor veel van de berekeningen in dit proefschrift. Last but certainly not least, I would like to thank Hermann Selier for the brief but fruitful and very enjoyable period we worked together.

Tijdens mijn werk in Delft heb ik mijn kamer mogen delen met verschillende collega’s: Burghard Ilge, Mogens Fyhn, Eric van Zee, Paul Snijders, Rogier Boogaard en Frank Meijer wil ik bedanken voor hun gezelschap en de vele discussies die we gehad hebben, zowel over natuurkundige als over maatschappelijke en religieuze kwesties. In het NEXT-lab (pardon, UHV-SPM-lab) heb ik veel gehad aan Paul Snijders, Monica Craciun, Marc-Jan den Boer, Murat Durkut, Dagmar Wismijer, Eric Svensson, Andrew Dunn, Hon Tin Man, Natalia Cividjian, Christoph Bisch en Thierry Melin, niet alleen als experimenteer-partners, maar ook als discussie-partners. Verder wil ik alle overige

groepsleden (ook al zal ik ze hier niet bij name noemen) hartelijk bedanken voor de gesprekken tijdens koffie en lunch, hun hulp en—vooral—hun bijdrage aan de opbouw van het wetenschappelijk klimaat en de werksfeer in de groep na de reorganisatie van Nanofysica in de beginfase van mijn promotietijd.

Technici zijn onmisbaar voor experimenteel onderzoek. Ik heb vooral veel gebruik mogen maken van de diensten van Ron Hoogerheide, die al mijn vage ideeën wist om te zetten in een uitvoerbaar ontwerp en dat vervolgens ook realiseerde. Ook de overige technici, Jordi Schmitz, Jan Toth, Eelke Algera, Norbert Koster en Ben de Lange, wil ik bedanken voor hun hulp met mijn vele kleine vragen. Liefde voor cleanroom-fabricage heb ik nooit gekregen, maar dat lag niet aan Emile v.d. Drift en de cleanroom-technici. Bij mijn spaarzame werkzaamheden in de DIMES-cleanroom heb ik veel gehad aan hun kennis van en ondersteuning bij het microfabricage-werk. De management-assistenten in de groep nemen de naam van hun functie gelukkig niet al te letterlijk en ondersteunen behalve de ‘groepsmanager’ ook de promovendi. Nejla Özkaya, Margaret van Fessem, Maria Roodenburg en Monique Vernhout wil ik daarom bedanken voor hun praktische en administratieve hulp, alsmede voor hun welkome niet-natuurkundige inbreng in de groep.

Hoewel ik een uitstekende STM tot mijn beschikking had, wilde ik soms meer (i.e. lagere temperaturen). Daarom ben ik zeer dankbaar jegens Serge Lemay, Brian LeRoy, Sander Otte, Abdou Hassani, (MB) Leonid Gurevich (QT), Gert-Jan van Baarle en Jan Aarts (Leiden), die allen hun STM beschikbaar hebben gesteld voor mijn experimenten en tijd voor mij hebben vrijgemaakt om waar nodig te helpen die experimenten uit te voeren. Het ‘NanoComp’-DIOC, waar mijn onderzoek deel van uit maakte, leidde tot verscheidene bijeenkomsten en vergaderingen met promovendi en stafleden van buiten de natuurkunde-faculteit. Deze kennismaking en discussie met mensen uit andere vakgebieden heb ik als erg interessant ervaren. Peter Hadley wil ik bedanken voor zijn bijdrage aan de invulling van mijn onderwijstaak.

Enkele mensen ‘van buiten’ wil ik niet onvermeld laten voor hun hulp. W.J. Eij-senga and W. Crans van de faculteit Elektrotechniek lieten mij gebruik maken van hun device-simulatie software. Marco Hopstaken en Geert Maas van Philips verrichtten SIMS-metingen aan mijn samples. Verder fabriceerden Roger Loo en Matty Caymax van IMEC verschillende belangrijke lagen-pakketten. Stephan Winnerl, Helge Bay en Siegfried Mantl van Forschungszentrum Jülich wil ik bedanken voor het groeien van enkele CoSi_2 lagen. I am grateful to John Tucker from the University of Illinois for several useful discussions.

Gelukkig was er nog voldoende leven naast de promotie, waarin mijn vrienden van het Goudse lyceum en de Utrechtse natuur- en wiskundestudie een belangrijke rol speelden. Hen wil ik hartelijk danken voor hun interesse in mijn onderzoek en de vele leuke feestjes, bezoeken, gesprekken etc. die we samen hadden. Een speciale vermelding is voor Femius Koenderink, dankzij wiens hulp ik verscheidene $\text{L}^{\text{A}}\text{T}_{\text{E}}\text{X}$ -gerelateerde problemen in mijn proefschrift heb kunnen oplossen. Ook mijn (schoon)familie wil ik bedanken voor hun belangstelling en aandacht voor mij en mijn werk. Mies Huizenga wil ik bedanken voor het proeflezen van de samenvatting. In het bijzonder wil ik ook mijn ouders bedanken, die via mijn opvoeding een moeilijk te benoemen, maar belangrijke rol gespeeld hebben in mijn ontwikkeling. Tenslotte Hennie, die er—tussen het vangen van baby’s door—altijd onvoorwaardelijk voor mij was en hopelijk nog heel lang zal zijn.

Curriculum Vitae

Gert-Jan Smit

- 1975 Born on November 17th in Meppel, The Netherlands
- 1988–1994 Gymnasium, Christelijk Lyceum-HAVO, Gouda
- 1994–1998 M.Sc. Experimental Physics, *cum laude*, University of Utrecht
“Dynamics of phonons in amorphous and nanocrystalline silicon”. Research carried out in the Condensed Matter group of Prof. Dr. J.I. Dijkhuis
- 1994–1999 M.Sc. Mathematics, *cum laude*, University of Utrecht
“A dependent bond percolation model”. Research carried out under supervision of Dr. R. Meester in the Probability-theory group
- 1999–2004 Ph.D. Physics, Delft University of Technology
“Atomic scale electronics in semiconductors”. Research carried out in the Nanophysics group of Prof. dr. ir. T.M. Klapwijk

